3D IMAGING AND AUTOMATED POINT CLOUD ANALYSIS FOR IN-FIELD PLANT MAPPING

by

SHANGPENG SUN

(Under the Direction of Changying Li)

ABSTRACT

Agriculture is facing tremendous challenges to meet the needs of a growing world population which is projected to exceed 9 billion by 2050. It is urgent to build a sustainable agriculture system in order to accelerate crop improvement while reducing the environmental footprint. High through phenotyping, which refers to the process of measuring and assessing qualitative and quantitative plant bio-physical traits in an efficient and effective manner, is instrumental both in facilitating new plant breeding technologies and improving crop management practices.

This dissertation mainly focused on the development of field-based 3D imaging systems and methodologies for plant trait mapping from canopy level to organ level. Cotton plants were used as the model plants since cotton is among the most economically important crops providing natural fiber throughout the world. A ground vehicle-based 3D plant canopy surface reconstruction system, mainly consisting of a 2D line scan light detection and ranging (LiDAR) sensor and a real-time kinematic GPS, was developed to scan plants periodically. Algorithms were developed to extract three morphological traits at plot level and monitor their growth rate. In order to reduce the occlusion problem which was a major reason for the underestimation of cotton boll counting from images, a multi-view camera system was developed to scan plants from different perspectives.

Then, dense point clouds were reconstructed from the images using structure from motion algorithm, from which a supervoxel-based segmentation and density-based clustering algorithm was developed to map cotton bolls. In addition to boll number, its size and position were extracted. A data processing pipeline, including skeleton extraction, main stalk and individual branches segmentation, and node localization, was developed to map plant nodes from point clouds obtained using a high-resolution 3D LiDAR. Experimental results showed that the developed systems and methodologies can accurately and efficiently measure these phenotypic traits. Furthermore, in addition to automating the types of the traits measured manually, the developed systems and methodologies can measure new phenotypic traits. Therefore, they can be used as tools both for plant researchers and growers alike, and can be used for other plants such as wheat after minor modifications.

INDEX WORDS: High Throughput Phenotyping, Artificial Intelligence, 3D Imaging System, Point Cloud, Computer Vision, LiDAR, Segmentation, Clustering, Precision Agriculture, Plant Architecture Pattern, Yield Prediction, Crop Growth Monitoring

3D IMAGING AND AUTOMATED POINT CLOUD ANALYSIS FOR IN-FIELD PLANT MAPPING

by

SHANGPENG SUN

B.S., Xi'an University of Science and Technology, China, 2007

M.S., Beijing Jiaotong University, China, 2009

Ph.D., Beijing Jiaotong University, China, 2014

A Dissertation Submitted to the Graduate Faculty of The University of Georgia in Partial Fulfillment of the Requirements for the Degree

DOCTOR OF PHILOSOPHY

ATHENS, GEORGIA

2019

3D IMAGING AND AUTOMATED POINT CLOUD ANALYSIS FOR IN-FIELD PLANT MAPPING

by

SHAGNPENG SUN

Major Professor:	Changying Li
Committee:	Peter Kner
	Ping Ma
	Glen Rains
	Peng Chee

Electronic Version Approved:

Ron Walcott
Interim Dean of the Graduate School
The University of Georgia
December 2019

DEDICATION

To my parents and wife

ACKNOWLEDGEMENTS

I would like to express a special thanks to Dr. Changying Li for providing me the opportunity to work with a great team under his guidance. Thank you for your advice, support, and encouragement whenever needed. Thanks for always showing me the right direction in research and my career. I will always cherish the time when I worked in your group. I look forward to many collaborations with you in the future.

I would also like to thank Dr. Glen Rains, Dr. Peter Kner, Dr. Peng Chee, and Dr. Ping Ma for serving on my committee. I appreciate your gracious support and critique of my research. It has been extremely helpful. I would like to thank Dr. Andrew Paterson for providing research resources and advice on the experiment design.

My thanks also go to other collaborators and my friends, including Dr. Yu Jiang, Mr. Rui Xu, Dr. Mengyun Zhang, Mr. Zikai Wei, Mr. Tsunghan Han, Mr. Jawad Iqbal, Mr. Rikki Brown, Mr. Jesse Kuzy, Dr. Ruoyu Zhang, Mr. Jon Robertson, Mr. Jeevan Adhikari, and Dr. Tariq Shehzad, Mr. Cheng Meng and Miss Jingyi Zhang. I am thankful for the invaluable discussions regarding my research projects, and all the laughs we have had together.

Particularly, I want to thank my father and my mother who have always supported me during my life. Thanks to my wife for love and support.

TABLE OF CONTENTS

Page

CHAPTER

LIST OF TABLES

LIST OF FIGURES

CHAPTER 1

INTRODUCTION

1.1 Background and Significance of This Study

Agriculture provides food, fiber, biofuels, and other products for people living on this planet, and is facing tremendous challenges to meet the needs of the current and future world population. Today, more than 820 million people remain undernourished, and approximately two billion people suffer from food insecurity in the world (Egal, 2019). More food and fiber are required to sustain the growing world population which is projected to exceed 9 billion by 2050 (Gerland et al., 2014), but agricultural production is negatively affected by environmental changes such as climate change, decreasing arable land and freshwater (Cordell et al., 2009). For example, it was reported that environmental changes caused around a 4 ~ 5 % decline for the production of maize and wheat during the past three decades (Lobell et al., 2011). However, agricultural activities can cause great environmental threats (Crist et al., 2017). For example, agricultural activities release greenhouse gases into the atmosphere, contributing to the world temperature change (Ollivier et al., 2019); they are also the major cause of freshwater eutrophication (Ortiz-Reyes and Anex, 2018). Thus, it is urgent to build a sustainable agriculture system in order to accelerate crop improvement while reducing the environmental footprint.

Plant phenotyping is a process of evaluating plant performance by measuring qualitative and quantitative plant bio-physical traits (Pieruschka and Schurr, 2019). High throughput phenotyping provides methods for plant trait mapping which is instrumental both in facilitating new plant breeding technologies and in improving crop management practices (Butler et al., 2017; Granier and Vile, 2014; Ninomiya et al., 2019), and plays a vital role in building the sustainable agriculture system (Zaidi et al., 2019). During the past decade, 2D imaging methods have been widely applied in phenotyping, and have significantly facilitated the efficiency of phenotypic trait measurement and analysis (Li et al., 2014). These methods, however, have significant limitations. For example, it is difficult to address the occlusion problem, which is one of the major challenges for plant phenotyping. Furthermore, it is difficult to determine actual size from 2D images.

3D imaging technologies have a great potential to overcome these limitations because depth information is provided, and therefore are receiving more attention for plant phenotyping (Paulus, 2019; Vazquez-Arellano et al., 2016). Today, new 3D sensing technologies and increased computing power enable obtaining and processing high-resolution 3D data. This dissertation mainly focuses on the development of field-based 3D imaging systems and methodologies to extract plant phenotypic traits from the whole canopy to organ level. Cotton plants were used as model plants in this dissertation, because cotton is one of the most economically important fiber crops, that produces natural fiber throughout the world (Günaydin et al., 2019), and cotton is the most widely grown row crop in Georgia, USA, producing a market value of around $794.9 million in 2018 (USDA, 2018b).

The two most commonly used principles of image-based 3D reconstruction are Time-of-Flight (ToF) and triangulation (Gibbs et al., 2017; Vazquez-Arellano et al., 2016). ToF, which is an active way to determine depth, estimates the true distance from the sensor to the object based on the flight time of an emitted signal which hits the object and returns to the receiver (Figure 1.1a) (eq (1.1)).

$$z = \frac{c\left(t_2 - t_1\right)}{2} \tag{1.1}$$

where z is the depth, c is the speed of the signal, and (t_2 - t_1) is the difference between the time when the signal was emitted and when it was received. A common approach to determine the time difference is to measure the phase shift between the outgoing and returning modulated waves (Yuan et al., 2014). Assume φ is the measured difference of phase angle, ω is the wave frequency, $\omega = 2\pi f$, the time difference can be calculated using eq (1.2).

$$\varphi = \omega\Delta t = 2\pi f\,\Delta t \tag{1.2}$$

Light Detection and Ranging (LiDAR) is one of the most commonly used ToF sensors for field-based plant 3D reconstruction (Lin, 2015). LiDAR data have also been used to derive other phenotypic traits including leaf area index (Richardson et al., 2009), plant counting (Shi et al., 2015), and tree structure analysis (Méndez et al., 2016). The resolution of LiDAR improves with the development of sensing technologies. Recently, several studies have reported the application of a high-resolution 3D LiDAR for infield point cloud acquisition and have developed custom algorithms to extract plant organ level traits such as leaf angle (Jin et al., 2018) and sorghum panicles (Malambo et al., 2019). Microsoft Kinect v2 is another widely used ToF sensor, which provides both 3D and color measurements. Jiang et al. (2017) applied a Kinect V2 sensor to build colored point clouds of cotton plants under field conditions. The sensor was mounted inside an enclosure in order to reduce sunlight influence. Results showed that the resolution of the point clouds was not high enough to distinguish plant organs such as branches and leaves. Therefore, only plant level morphological traits were extracted from the 3D data. In addition, Vázquez-Arellano et al. (2018) applied a Kinect v2 to detect plant positions in a greenhouse. Tao and Zhou (2017) used the sensor for apple recognition under field conditions. Other TOF sensors such as light curtain (Busemeyer et al., 2013a) and Radar (Hosseini et al., 2015) have been explored for plant phenotyping. Overall, TOF sensors can provide accurate point cloud data, and have certain ability to resist varied illumination influence. However, the sensors are usually expensive because special hardware is needed to calculate the flight time which is critical to the accuracy of distance measurements.

Triangulation techniques measure distances based on a triangle consisting of the target and two sensors (Rusu, 2010). Stereo vision is a popular method for obtaining 3D data passively as it does not need to send any light onto the object for distance estimation. Stereo vision extracts 3D information by processing two images captured with slightly different horizontal perspectives. Usually, the two cameras are calibrated with respect to each other to obtain the focal length and baseline (Figure 1.1b). Then, pairs of corresponding points matching the projection of the same 3D point are detected from the two images. This process is called correspondence search, which is one of the most challenging tasks of stereo vision. The 3D reconstruction—referred to as triangulation—is to compute the 3D positions of these matched points (Figure 1.1b). The depth of a pair of matched points is determined as the intersection of the two projected rays.

$$z = \frac{Bf}{x_l - x_r} \tag{1.3}$$

where z is the depth of the 3D point, B is the distance between the two centers of projection, called baseline, f is the focal length of the cameras, x_l (x_r) is the position of the projected point on the horizontal axis in the left (right) image, (x_l-x_r) is called disparity. If the scene is static, the two images can also be taken in sequence by a single camera at two positions. Once such a strategy is considered, more than two images can be taken by moving the camera. Such strategy is referred to as structure-from-motion (SfM). SfM approaches calculate 3D data either sequentially or globally from corresponding points which can be detected using scale invariant feature transform (SIFT) (Snavely et al., 2008). Overall, these methods are less expensive than ToF sensor-based methods for 3D reconstruction, because they only need a standard camera to capture overlapping images of an object. Moreover, having more camera views reduces the possibility of occlusion, thereby resulting in more complete 3D object models. These properties render stereo vision and SfM very attractive 3D acquisition strategies.

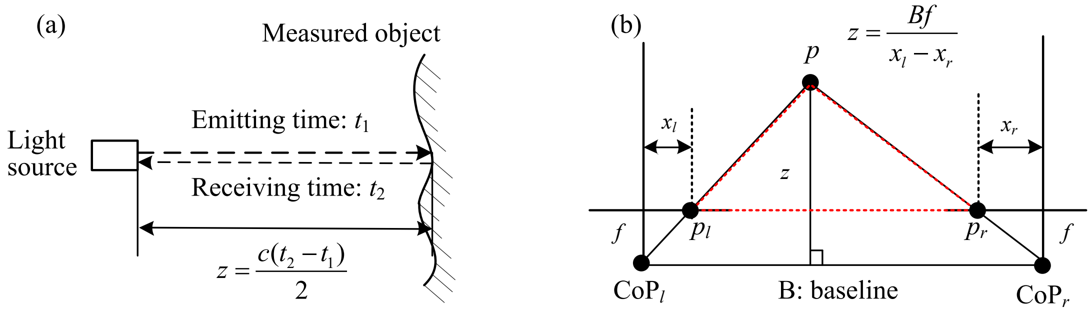

Figure 1.1. Schematic representation of 3D reconstruction methods. (a) Time of flight method. c is light speed. (b) stereo vision triangulation. CoP$_l$ and CoP$_r$ are centers of projection for the left and right sensors, respectively; P, P_l and P_r are the real point in scene, projection point in left image plane and projection point in the right image plane, respectively; f is the focal length of the camera, B is the distance between CoP$_l$ and CoP$_r$; x_l (x_r) is the position on the horizontal axis in the left (right) image. Triangle P-P_l-P_r is similar to Triangle P-CoP$_l$-CoP$_r$.

Underwood et al. (2017) and Fernandez et al. (2017) applied stereo cameras attached to ground vehicle-based platforms to build 3D point clouds for maize and wheat under natural illumination conditions, respectively. Accurate and dense point clouds were obtained, thus making plant organ traits extraction possible. The developed algorithms successfully extracted plant geometric traits such as plant height and stem diameter from the data. Stereo cameras take images simultaneously, therefore, it is easier to find correspondences because illumination conditions can vary slightly, and wind-induced plant movement is small. However, images are taken sequentially for SfM-based methods, which can result in a relatively long time for image collection, particularly for large field applications. In order to shorten the time of data collection, unmanned aerial vehicles

(UAVs) are used as platforms on which cameras are attached for data collection. Chu et al. (2018) reconstructed 3D point clouds of maize from images taken by a camera attached to an UAV, and plant height was extracted from the data with the R^2 between algorithm measurements and ground truth up to 0.89. The limitation was low resolution, which made it difficult to extract organ level traits. Duan et al. (2016) built very dense 3D point clouds of wheat using SfM under controlled environment conditions, and developed algorithms to extract plant organ level traits such as leaf angle and leaf elongation rate. Sunlight is a factor affecting the 3D data quality for infield applications. If sunlight is too bright, the taken images would be in the absence of texture, making finding corresponding points more difficulty. A potential solution is to add an enclosure in order to provide a consistent illumination condition. In addition, the parameters of a camera such as aperture, shutter speed, and ISO need to be adjusted according to specific plants in order to ensure that objects in images contain good texture characteristics. Another way reducing effects of the problem is to replace one of the cameras in a stereo setup by a projection device such as a projector, that is to apply an active way to facilitate the process of finding corresponding points. This technique is called structured light. A calibrated light source emits light, and it is reflected into the camera when hitting a target object. The emitted light is with predesigned pattern such as lines and grids, therefore making it easy to detect in the image. There are other passive approaches to 3D reconstruction using triangulation principle, such as shape from silhouette (Masuda, 2019) and space carving (Kutulakos and Seitz, 1999). However, they are used less frequently for plant 3D reconstruction, because they have a limited capability to handle plants with complex structures.

1.2 Objectives

The overall goal of this dissertation was to develop 3D imaging-based high throughput phenotyping systems for plant mapping from canopy traits to organ traits under field conditions. Specific objectives were to:

1. Develop plant canopy morphological traits extraction and plant growth monitoring algorithms from point clouds reconstructed using a 2D line scan LiDAR and an RTK-GPS sensor.
2. Develop single cotton boll detection algorithms from 2D images and point clouds, respectively. The point clouds were reconstructed from images captured using multi-view RGB cameras.
3. Develop plant node detection algorithms from point clouds using a 3D terrestrial LiDAR.

1.3 Overview of the Dissertation Chapters

This dissertation consists of seven chapters. Chapter 1 introduces background of the study and the current status of field-based plant phenotyping and describes the objectives of this dissertation.

Chapter 2 introduces a 3D sensing system and methodologies used for plant canopy surface model reconstruction and plant height extraction. The sensing system mainly consisted of a 2D line scan LiDAR and an RTK-GPS sensor which were attached on a ground vehicle-based platform. The LiDAR scanned plants from the top view, and each line scan was geotagged GPS data, resulting in 3D point clouds of the scanned plants. Then a point cloud processing pipeline was designed to extract plant canopy height for each plot.

Chapter 3 introduces a point cloud processing pipeline for plant morphological trait extraction and plant growth analysis. The LiDAR and RTK-GPS sensing system was used to scan plants periodically. Algorithms were developed to extract canopy height, projected canopy area and plant volume from the reconstructed point clouds for each plot. A three-parameter logistic model was used to fit the growth curves for the three traits. In addition, the linear correlations between the traits extracted at different growing stages and fiber yield were analyzed.

Chapter 4 introduces image processing algorithms for single cotton boll counting under field conditions. An RGB camera was mounted on a robot platform to take images of cotton plants. A double-thresholding with region growth algorithm was developed for cotton boll segmentation from images, then single cotton boll was identified based on boll shape, size and position features. Correlation analysis between cotton boll number and fiber yield was explored.

Chapter 5 introduces 3D photogrammetric mapping of cotton bolls under field conditions. Cotton boll number was underestimated using the 2D image-based method. A multi-view camera system was designed to scan plants from different perspectives, and an algorithm named structure form motion was used to reconstruct dense point clouds from images. A data processing pipeline including point cloud segmentation and clustering was designed to identify individual bolls. In addition to cotton boll number, two more traits – cotton boll volume and position – were extracted from this method.

Chapter 6 introduces methodologies for plant node detection from point clouds. A high-resolution terrestrial LiDAR was used to obtain point clouds of single plants under field conditions. A Laplacian-based contraction algorithm was used to extract a skeleton of a plant from the point cloud, then a graph-based method was developed to segment the main stalk and individual branches, after that each node was identified by finding the intersection between the main stalk and a branch. The trait height-node-ratio was also calculated.

Chapter 7 provides general conclusions and limitations of this dissertation and proposes research plans in the future.

CHAPTER 2

IN-FIELD HIGH THROUGHPUT PHENOTYPING OF COTTON PLANT HEIGHT USING LIDAR[1]

---

[1] Sun, S.; Li, C.; Paterson, A.H. *Remote Sensing* 2017, 9, 1-21. Reprinted here with permission of publisher.

Abstract

A LiDAR-based high-throughput phenotyping (HTP) system was developed for cotton plant phenotyping in the field. The HTP system consists of a 2D LiDAR and an RTK-GPS mounted on a high clearance tractor. The LiDAR scanned three rows of cotton plots simultaneously from the top and the RTK-GPS was used to provide the spatial coordinates of the point cloud during data collection. Configuration parameters of the system were optimized to ensure the best data quality. A height profile for each plot was extracted from the dense three dimensional point clouds; then the maximum height and height distribution of each plot were derived. In lab tests, single plants were scanned by LiDAR using 0.5° angular resolution and results showed an R^2 value of 1.00 (RMSE = 3.46 mm) in comparison to manual measurements. In field tests using the same angular resolution; the LiDAR-based HTP system achieved average R^2 values of 0.98 (RMSE = 65 mm) for cotton plot height estimation; compared to manual measurements. This HTP system is particularly useful for large field application because it provides highly accurate measurements; and the efficiency is greatly improved compared to similar studies using the side view scan.

2.1 Introduction

Geometric characteristics of crops (height, crown size, and volume) have great scientific value for crop breeders and geneticists (Garrido et al., 2015; Rosell-Polo et al., 2009). These characteristics are useful not only for quantitative analysis of genotype–environment interactions, which is essential for increasing crop performance (Cobb et al., 2013; Goggin et al., 2015; Großkinsky et al., 2015), but also for improving crop management strategies such as fertilization, irrigation, and optimization of harvesting (Lipka et al., 2015; Stamatiadis et al., 2010; White et al., 2012). Several studies have shown interactions between geometric parameters of plants and crop yield as well as biomass (Cobb et al., 2013; Ghanem et al., 2015; Granier and Vile, 2014; Großkinsky et al., 2015; Sharma and Ritchie, 2015). Manual measurements of crop traits, which are still often used in practical phenomic applications, have significant limitations and drawbacks. These methods are time-consuming and labor intensive, which inevitably increases cost (Barker III et al., 2016; Sharma and Ritchie, 2015). Additionally, manually obtained measurements are subject to human error due to fatigue and distractions during data collection.

Several platforms based on remote sensing technologies have been developed for automatic crop phenotyping in greenhouses over the past three decades (Palanichamy and Cobb, 2015; Pratap et al., 2015), but such controlled conditions are significantly different in many important ways from the outdoor agricultural environment in which the vast majority of crops are produced. Admittedly, there are tremendous challenges to developing field-based high-throughput phenotyping (HTP) systems in the highly variable natural environment, including variable natural lighting, high temperature, uncontrolled rainfall, and occlusion of plant features between adjacent plants within a plot or between plots, to name a few. While genomics now empowers detailed and cost effective analysis of plant genetic composition, field-based high-throughput phenotyping capabilities currently remain a major bottleneck limiting plant genome research and crop improvement (Barker III et al., 2016; Cobb et al., 2013).

Crop height is an important parameter among geometric characteristics; it has important implications for plant health, crop yield and quality, and total biomass (Hofle, 2014; Stamatiadis et al., 2010; Zhang and Grift, 2012). Crop height also influences the interactions between plants and solar radiation, water, and nutrients (Sharma and Ritchie, 2015). Crop growth rates—as reflected by changes in height—provide an indicator to assess the efficiency and effectiveness of management strategies related to fertilization, irrigation management, pruning, and harvesting (Sritarapipat et al., 2014; Tilly et al., 2014). Cotton plant height is a function of the extension of main stem internodes, which is strongly influenced by determinacy and growing environment (Baloch et al., 2014; Siebert and Stewart, 2006). Consequently, it is of great value to develop field-based systems to estimate crop height effectively and efficiently.

Several approaches based on remote sensing technologies have been published in the scientific literature for crop height measurement. Ultrasonic sensors are the most commonly used sensor to measure crop height in agriculture applications (Andrade-Sanchez et al., 2013; Barker III et al., 2016; Sharma and Ritchie, 2015). One of the main drawbacks of an ultrasonic sensor is that the field of view becomes larger as the distance between the sensor and the object increases—reducing the accuracy of measurements—due to the sensor's relatively wide angle divergence of ultrasonic waves. Additionally, the ultrasonic sensor is sensitive to temperature variations, which limits its outdoor use (Barker III et al., 2016).

Computer vision based techniques have also been employed for crop height measurement: Carlone et al. (2015) presented a plant height and crown radius measurement system which used an RGB camera with an inertial measurement unit (IMU) and a GPS mounted on a tractor to collect data weekly. A 3D model of the scanned crop was obtained by applying SLAM (simultaneous localization and mapping) techniques (Furukawa and Ponce, 2010) and multi-view stereo algorithms (Kaess et al., 2011) to process the images and sensor data. The system obtained reasonable estimates for crop height and crown radius.

Busemeyer et al. (2013a) used 3D time-of-flight (TOF) cameras for field phenotyping research. A 3D TOF camera was mounted above plant height for vertical top view measurements of the canopy, an enclosure was used to provide a stable environment for the sensor, and the reported mean relative error (MRE) ranged from 4.3% to 6.5%. However, one major limitation of image based methods is that data quality can be significantly affected by the variable environment, since shadows and sunlight can result in under or over exposure and limit automatic data processing.

LiDAR (light detection and ranging) is a remote sensing technology used to measure the distance to an object of interest based on the TOF principle. This technique has gained increasing attention in precision agriculture and forestry applications due to its high accuracy, reading speed rates, and versatility. Furthermore, LiDAR's robust operational capacities in a wide range of light conditions make this technology highly favorable for outdoor use (Lin, 2015). In addition, a 3D structure model of plants can be obtained with a 2D LiDAR when georeferenced sensors are used, from which various structural characteristics have the potential to be derived. A 2D LiDAR collects two dimensional scans in a measured plane, and the third dimension is obtained by moving the sensor along the perpendicular direction to the scanning plane. Usually a LiDAR system is attached to different platforms for various demands. Aerial LiDAR has been successfully used in forest ecosystem applications such as mapping and canopy structural characteristic retrieving. Leeuwen and Nieuwenhuis (2010) presented an overview of how LiDAR remote sensing can be used to derive forest structure attributes such as tree height, leaf area, and branch detection, and addressed approaches for fusing LiDAR data with passive optical techniques. LiDAR remote sensing is expected to play a key role in forest ecosystem, biomass, and biodiversity studies over the coming years. Zhao and Popescu (2009) explored the capability of LiDAR to remotely map leaf area index (LAI) in a temperate forest of the southern USA. The correlation of two LAI maps between the LiDAR and the optical remote sensor (the GLOBCARBON moderate resolution satellite LAI product) was up to 0.85 for pines, which implied that LiDAR offered a viable tool for mapping LAI. However, aerial LiDAR was not as effective in agriculture crops phenotyping activities since it has limited capability to provide high resolution information for crops which are much smaller than trees (Murgoitio et al., 2014).

Terrestrial LiDAR has the potential to provide denser point clouds over a relatively small area, from which high resolution information could be extracted. Therefore, it has been increasingly used in field phenotyping (Lin, 2015). Llorens et al. (2011) compared the use of ultrasonic sensors and LiDAR to capture canopy characterization in vineyards, and they concluded that data obtained with LiDAR is generally more precise than data obtained with ultrasonic sensors. Rosell Polo et al. (2009) designed a tractor-mounted LiDAR to scan several kinds of tree and plantations from the side view. Known objects were placed for reference at known positions during data collection, and an algorithm based on the reference points was used to obtain the 3D structure model. For some selected trees the volume estimation based on the 3D model was accurate—the correlation coefficient was up to 0.976 between LiDAR measurements and manual measurements—but the procedure of 3D model reconstruction was very time-consuming as several steps had to be carried out manually. Auat Cheein et al. (2015) compared four real-time canopy volume estimation approaches based on LiDAR data collected using the methodology (Rosell Polo et al., 2009) and 3D model reconstruction procedure. Results showed that the volume could be estimated using partially scanned canopies on either left or right sides. For the worst case, the volume was about 70% of the value estimated by fully scanned canopies. Other methods for measuring tree canopy structure information using LiDAR were discussed by Pforte et al. (2012) and Sanz-Cortiella et al. (2011). Shi et al. (2015) introduced a corn plant locations and stalk numbers measurement system using a LiDAR with an encoder mounted on a modified golf cart. However, one limitation was that error might be accumulated since plant locations were determined from LiDAR position information recorded with a shaft encoder. Zhang and Grift (2012) proposed a LiDAR-based crop height measurement system for *Miscanthus giganteus*, in which the LiDAR was attached to a tractor and the crop scanned from the side view. In static mode, an average error of 5.08% was achieved; in dynamic mode, an average error of 3.8% was achieved. For dynamic situations, the tractor must be driven at constant velocity since no odometers were used to provide position information of LiDAR scans. However, moving at a constant speed was not easy to implement in the field. 3D LiDAR is being developed and explored for better characterization of plant structures, and some models are gradually becoming commercial available (Kjaer and Ottosen, 2015) but are still challenging to operate in harsh field environments. A detailed review of the potential of LiDAR in present and future applications was presented by Bhardwaj et al. (2016).

In this study, the height measurement of cotton plants was conducted using a LiDAR, but several improvements were made over the previously mentioned studies. Since cotton plants are much smaller than trees and have what some suggest to be the most complex structure of all major field crops (Mauney, 1986), more accuracy is required for a height measurement system for cotton than trees and other crops. In addition to height, other plant structure traits such as crown size and leaf area index can be extracted from a 3D map of cotton plants. The quality of the reconstructed 3D map of cotton plants plays a significant role in trait extraction. An RTK-GPS system which can offer 1 cm accuracy was used to provide the precise spatial coordinates at all times. This was useful for reconstruction of the 3D model because precise GPS data remedied the negative effect of inconsistent tractor speed. In addition, the LiDAR was set to scan plants from the top view so multiple rows could be scanned simultaneously, thereby greatly improving the throughput capability. The LiDAR scanning strategy in this study was similar to the method used by Andújar et al. (2016), where two rows of poplar trees were scanned at a time. Side view scanning is another commonly used strategy because other traits in addition to crop height could be measured, but only one row can be scanned simultaneously. We also proposed a systematic approach to optimize system configurations to ensure that the tallest parts of plants were scanned. The method used in this study is particularly useful for field application. Custom software for data acquisition was developed using LabVIEW 2014 (National Instruments Inc., Austin, TX, USA), which can be easily extended and customized.

The overall goal of this work was to develop a high-throughput phenotyping system using LiDAR for cotton plant height measurement in the field. Specific objectives were to: (1) design and implement a robust LiDAR data acquisition system (hardware, software, and system configuration methods) for data collection under dynamic field conditions; (2) develop a point cloud data processing pipeline for GPS and LiDAR data fusion to reconstruct a 3D model of cotton plants and extract height information; and (3) evaluate the performance of the proposed system with lab and field validation tests.

2.2 Materials and Methods

2.2.1. Data acquisition system

A tractor was used as the data acquisition platform (Figure 2.1a), and the schematic of the system is shown in Figure 2.1b. A LiDAR sensor unit (LMS 511 PRO SR, SICK AG, Waldkrich, Germany) was attached to a sensor bar at the back of the tractor (John Deere 6000 Sprayer, Deere & Company, Moline, IL, USA). The mounting height of the sensor bar could be adjusted by the tractor's hydraulic lift system from 1124 mm to 1824 mm above the ground. An RTK-GPS unit (Cruizer II, Raven Industries Inc., Sioux Falls, SD, USA) was used to provide the spatial coordinates of the LiDAR at all times. The LiDAR and RTK-GPS main characteristics are summarized in Tables 1 and 2. Data collected by LiDAR was recorded by a rugged laptop computer (S400, Getac Technology Corporation, Taipei, Taiwan) through an Ethernet interface. A dense 3D model of cotton plants was obtained when the tractor was driven along rows in the field. In this study, the maximum height (1824 mm) of the LiDAR was configured for field experiments. The LiDAR simultaneously scanned three rows of plants from above (the top view) in the field (Figure 2.1c and d).

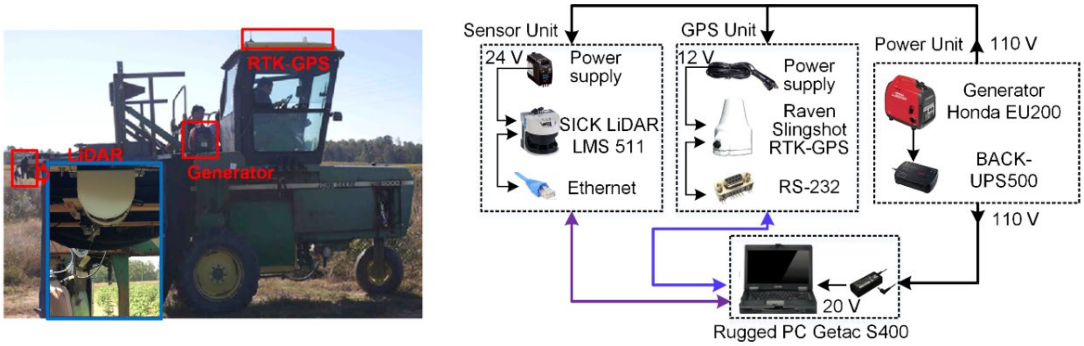

(a) Data acquisition platform during data collection in the field

(b) Device connection diagram

(c) Back view

(d) Top view

Figure 2.1. Diagram of data acquisition platform during data collection in the field.

Table 2.1. LMS 511 technical data.

Features		**Performance**	
Operating range	0~80 m	Systematic error	±25 mm (1 m~10 m) ±35 mm (10 m~20 m) ±50 mm (20 m~30 m)
Aperture angle	190° (−5°~185°)	Statistical error	6 mm (1 m~10 m) 8 mm (10 m~20 m) 14 mm (20 m~30 m)
Scanning frequency	25/35/50/75/100 Hz	Interface	Ethernet, RS-232,RS-422, USB, CAN
Angular resolution	0.167/0.25/0.333/0.5/0.667/1°	Supply voltage	24 V (22 W)
Wave length	Infrared (905 nm)	Temperature range	−30 °C to +50 °C

Table 2.2. Cruizer II RTK GPS technical data.

Features		**Performance**	
Sampling frequency	1, 5 and 10 Hz	Interface	RS-232, USB, CAN
RTK accuracy	1 cm	Supply voltage	9–16V DC (600 mA)
Differential correction	SBAS (RTK)	Temperature range	−30 °C to +70 °C
NEMA output	GGA, GLL, GSA, GSV, RMC, VTG, ZDA	Memory	FLASH, 256 MB

Custom software for data acquisition was developed using LabVIEW 2014 (National Instruments Inc., Austin, TX, USA). The front panel and flowchart of the block diagram are shown in Figure 2.2. A finite-state machine (FSM) was used in the event-driven custom software so the configurations can be changed without stopping the program. The FSM is a mathematical abstraction machine that can store one of a finite number of states at any given time and change from one state to another in response to external inputs. Compared to the commercial software SOPAS (SICK Open Portal for Application and Systems Engineering) which is commercially available software for communication, configuration and data logging, the developed software can be easily extended and customized. For example, it is easy to integrate extra sensors into the system or develop new data processing functions in the software.

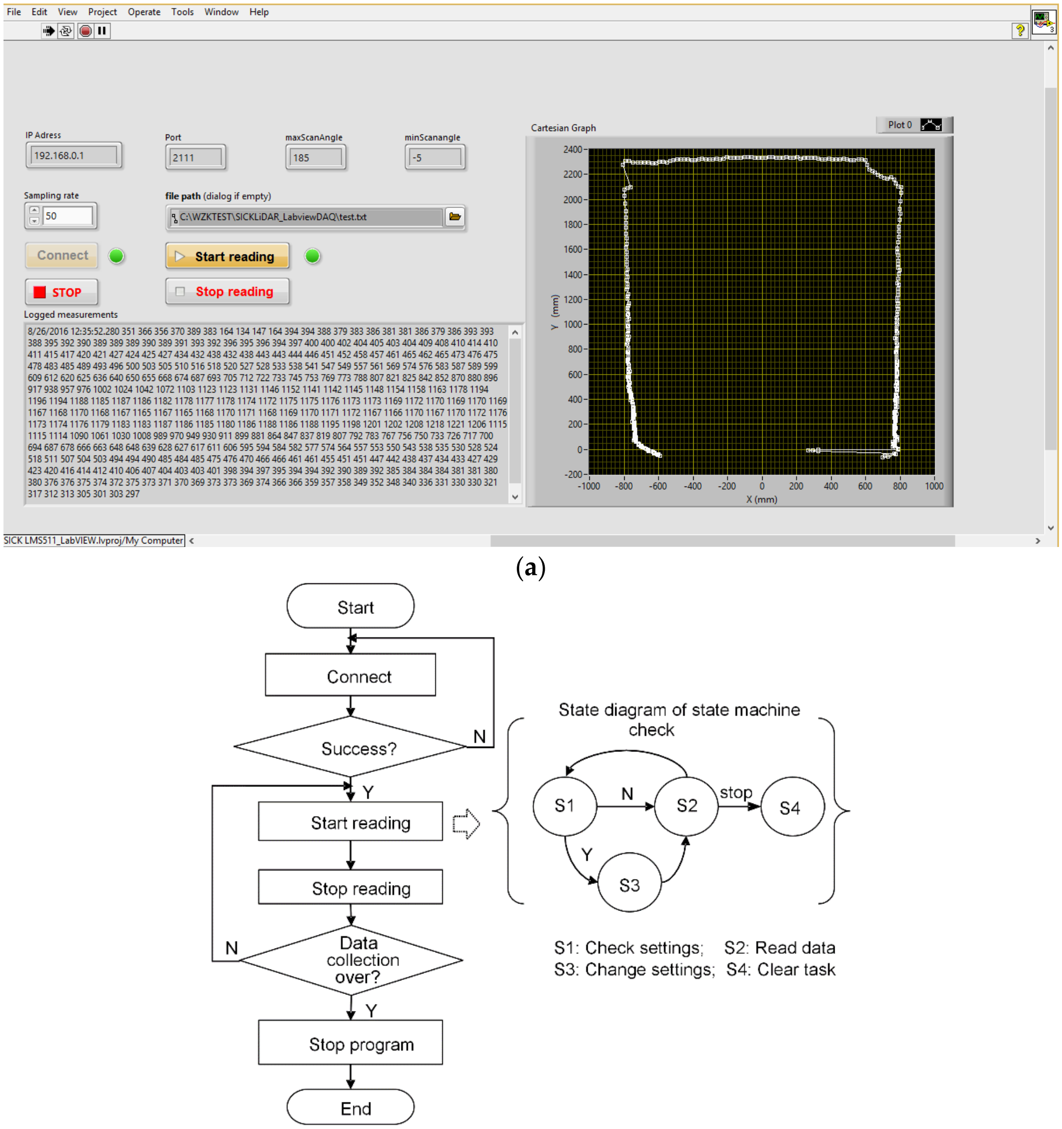

IP Adress: 192.168.0.1
Port: 2111
maxScanAngle: 185
minScanangle: -5
Sampling rate: 50
file path (dialog if empty): C:\WZKTEST\SICKLiDAR_LabviewDAQ\test.txt

Logged measurements

```
8/26/2016 12:35:52.280 351 366 356 370 389 383 164 134 147 164 394 394 388 379 383 386 381 381 386 379 386 393 393
388 395 392 390 389 389 389 390 389 391 393 392 396 395 396 394 397 400 400 402 404 405 403 404 409 408 410 414 410
411 415 417 420 421 427 424 425 427 434 432 438 432 438 443 443 444 446 451 452 458 457 461 465 462 465 473 476 475
478 483 485 489 493 496 500 503 505 510 516 518 520 527 528 533 538 541 547 549 557 561 569 574 576 583 587 589 599
609 612 620 625 636 640 650 655 668 674 687 693 705 712 722 733 745 753 769 773 788 807 821 825 842 852 870 880 896
917 938 957 976 1002 1024 1042 1072 1103 1123 1123 1131 1146 1152 1141 1142 1145 1148 1154 1158 1163 1178 1194
1196 1194 1188 1185 1187 1186 1182 1178 1177 1178 1174 1172 1175 1175 1176 1173 1173 1169 1172 1170 1169 1170 1169
1167 1168 1170 1168 1167 1165 1167 1165 1168 1170 1171 1168 1169 1170 1171 1172 1167 1166 1170 1167 1170 1172 1176
1173 1174 1176 1179 1183 1183 1187 1186 1185 1180 1186 1188 1186 1188 1195 1198 1201 1202 1208 1218 1221 1206 1115
1115 1114 1090 1061 1030 1008 989 970 949 930 911 899 881 864 847 837 819 807 792 783 767 756 750 733 726 717 700
694 687 678 666 663 648 648 639 628 627 617 611 606 595 594 584 582 577 574 564 557 553 550 543 538 535 530 528 524
518 511 507 504 503 494 494 490 485 484 485 475 476 470 466 466 461 461 455 451 451 447 442 438 437 434 433 427 429
423 420 416 414 412 410 406 407 404 403 403 401 398 394 397 395 394 394 392 390 389 392 385 384 384 384 381 381 380
380 376 376 375 374 372 375 373 371 370 369 373 373 369 374 366 366 359 357 358 349 352 348 340 336 331 330 330 321
317 312 313 305 301 303 297
```

(**a**)

(**b**)

Figure 2.2. Custom data acquisition software. (a) Front panel of the custom data acquisition software; (b) Flowchart of block diagram of the custom data acquisition software.

2.2.2 Configuration of system parameters

Cotton plants have perhaps the most complex structure of all major field crops. They do not have a homogenous crop surface like rice and maize. Therefore, a dense 3D point should be obtained to ensure that the highest points of plants are scanned by LiDAR. The interspace between two consecutive measured points within each frame, ΔD, should be less than the diameter of the laser beam, Φ (Figure 2.3, eq (2.1a)). Similarly, the interspace between two consecutive frames, ΔL, should be less than Φ (Figure 2.3, eq (2.1b)).

$$\begin{aligned} \Delta D &\le \Phi \quad (a) \\ \Delta L &\le \Phi \quad (b)' \end{aligned} \tag{2.1}$$

The diameter of the laser beam Φ increases in size as the distance from LiDAR increases, and the diameter can be determined by eq (2.2) (SICK, 2015):

$$\Phi = (0.011 \times dis) + 13 \ [mm], \tag{2.2}$$

where *dis* is the distance in mm between the LiDAR and the object to be measured. ΔD is dependent on the angular resolution selected and the distance *dis*, which is related to the mounting height. ΔL is a function of the moving speed of LiDAR—which is the velocity of the tractor—and the scanning frequency (frames per second) in Hz.

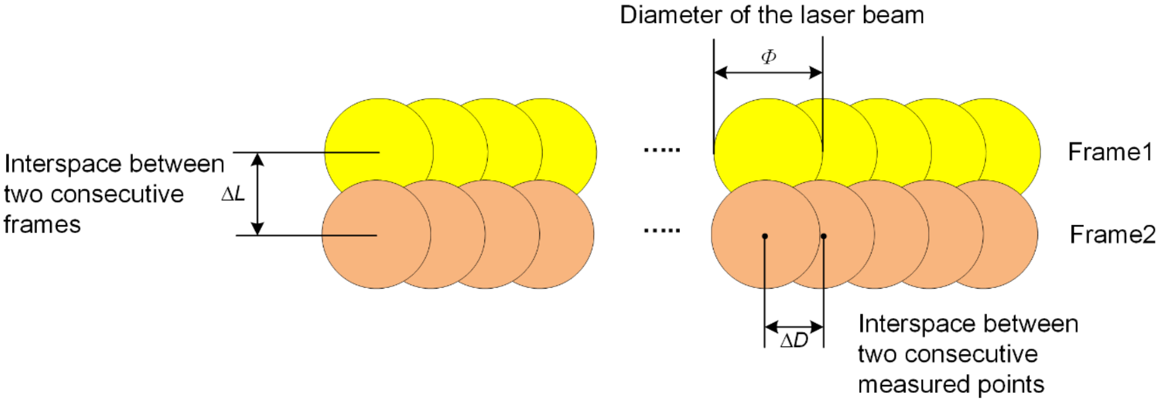

Figure 2.3. Schematic for full scanning without gaps along a cross section from a moving tractor.

2.2.2.1. Angular resolution

Figure 2.4 shows a geometric model to determine the angular resolution of LiDAR. A and B are two adjacent measured points. Distances from LiDAR to these two measured points are OA and OB, respectively. Let θ be the configured angular resolution, the angle $\varphi = \angle O'OB$, and H the mounting height of LiDAR (Figure 2.4). The laser diameter of measured points A and B can be calculated using eq (2.2), and the interspace between the measured points A and B using eqs (2.3)–(2.5). D_2 and D_1 are the distances from the LiDAR to points A and B, respectively, in the horizontal direction.

$$D_1 = H\tan(\varphi), \tag{2.3}$$

$$D_2 = H\tan(\varphi-\theta), \tag{2.4}$$

$$\begin{aligned}\Delta D = D_1 - D_2 &= H\left[\tan(\varphi)-\tan(\varphi-\theta)\right]\\ &= H\left[\tan(\varphi)-\frac{\tan(\varphi)-\tan(\theta)}{1+\tan(\varphi)\bullet\tan(\theta)}\right],\\ &= H\frac{\tan(\theta)\left(1+\tan^2(\theta)\right)}{1+\tan(\varphi)\bullet\tan(\theta)}\end{aligned} \tag{2.5}$$

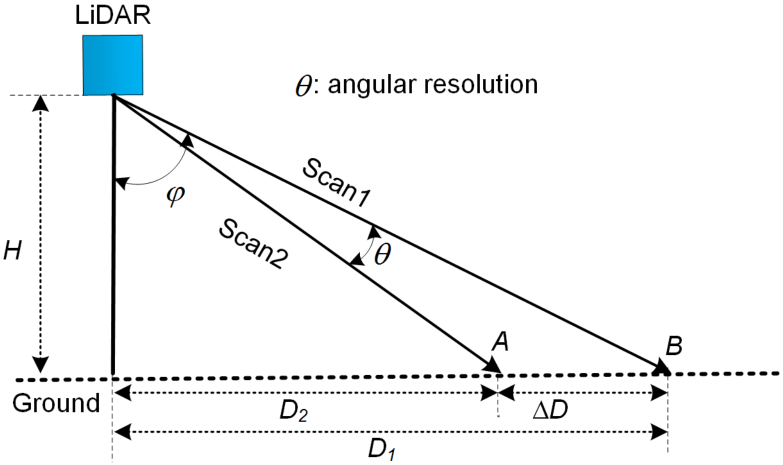

Figure 2.4. Geometric model for determining angular resolution of LiDAR.

If a coarse angular resolution was selected (Figure 2.5a), ΔD would be greater than Φ and some points of the objects would be missed. If a proper angular resolution was selected (Figure 2.5b and c), there would be no gap among consecutive measured points for each frame.

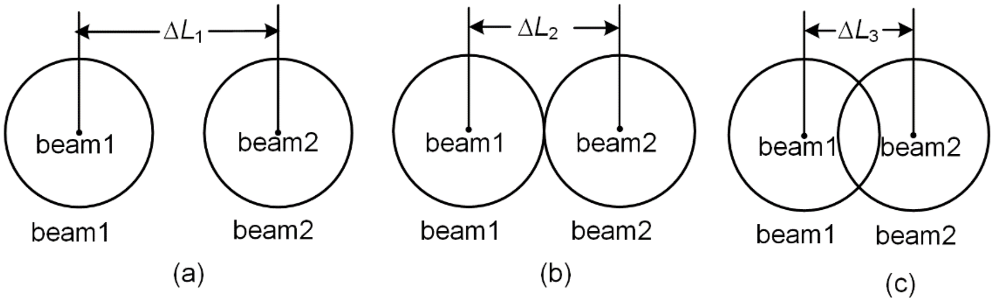

Figure 2.5. Influence of angular resolution: (**a**) $\Delta D_1 > \Phi$; (**b**) $\Delta D_2 = \Phi$; (**c**) $\Delta D_3 < \Phi$.

2.2.2.2. Mounting height

As explained in Section 2.2.1, the mounting height plays a significant role for the system since it affects the distance from LiDAR to the measured points. Mounting height is also an important factor influencing the number of rows that can be simultaneously scanned by LiDAR. In order to maximize throughput, LiDAR should simultaneously scan as many rows as possible without missing any plants. Figure 2.6a shows an example in which one plant in row 2 could not be scanned by LiDAR since it is blocked by its neighboring plant. Figure 2.6b–d demonstrate the relationship between the mounting height and the number of rows that can be simultaneously scanned. Here, we only considered the situation in which the LiDAR was mounted directly above the middle plant, and in this situation, only odd numbers of rows were scanned by LiDAR. Figure 2.6b,c show one and three rows being scanned, respectively. For these two situations, the mounting height should be higher than the tallest plants. Figure 2.6d illustrates a model used to retrieve the relationship between the mounting height and the scanned rows when five rows are scanned. Based on the two similar triangles with red dashed lines, eq (2.6) was derived, which can be rearranged to obtain the mounting height as shown in eq (2.7).

$$\frac{\Delta h}{H-h_2}=\frac{d}{\left(\frac{N-1}{2}\right)d}=\frac{2}{N-1}, \tag{2.6}$$

$$H=\frac{(N-1)h_1}{2}+\frac{(3-N)h_2}{2}, \qquad N=5, \tag{2.7}$$

In eq (2.6) and (2.7), d is the interspace between two adjacent rows; N is the number of rows simultaneously scanned; H is the mounting height of LiDAR; h_1 and h_2 are the height of plants p_1 and p_2, respectively; and $\Delta h = h_1 - h_2$, the difference between the heights of plants p_1 and p_2. Here, the extreme situation is that h_1 is the height of the tallest plant, and h_2 equals zero, which means there is no plant at the p_2 position.

The LiDAR is able to scan a larger range when it is attached at a higher height, but the laser spot size increases as the distance from the LiDAR to the measured point increases (eq (2.2)), resulting in a decreased spatial resolution. Therefore, the accuracy will decrease when the LiDAR measures a point at a far distance.

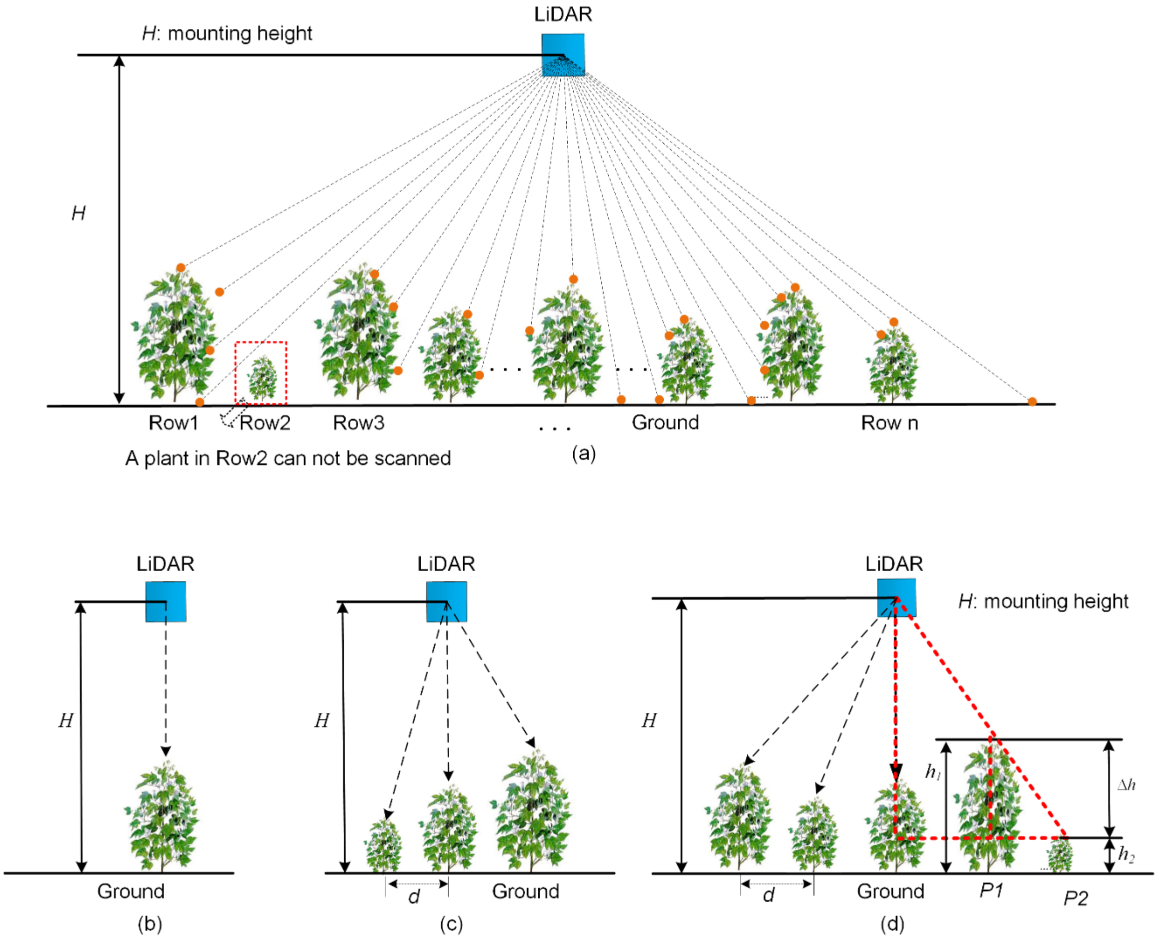

Figure 2.6. Relationship between mounting height and scanned rows: (a) diagram of one missed plant in Row 2; (b) one row was scanned; (c) three rows were scanned; (d) five rows were scanned.

2.2.2.3. Moving speed of the sensor unit

Similar to angular resolution, the interspace between two consecutive frames ΔL, which is the sampling resolution along the direction in which the sensor is moving, should be less than the diameter of the laser beam. ΔL can be determined by eq (2.8):

$$\Delta L = {}^{v}\!/_{f}\ , \tag{2.8}$$

where v is the velocity of LiDAR (which is the tractor's speed), and f is the sampling frequency of LiDAR in frames per second.

2.2.3. Experimental setup

2.2.3.1. Lab experiment setup

To evaluate the height measurement approach and validate the parameter configuration methods, a wooden frame was constructed, and experiments were conducted in the lab. The LiDAR was mounted on the frame and used to scan cotton plants from above to obtain the top view while a cotton plant was put on a cart and moved in and out of the frame during tests (Figure 2.7). Five cotton plants were used for lab tests (Figure 2.8): plants 1, 3 and 5 were in leaf and canopy development growth stage, while plants 2 and 4 were in flowering and boll development growth stage. Each plant was scanned ten times for each configured angular resolution; the average of the measurements was used as the LiDAR measured height. Manual measurements were used as a reference to evaluate the system performance. Cotton plant height, the distance between the highest point of the plant and the ground, was measured using a roller tape. The variable of angular resolution was used as an example to demonstrate the impacts of different configuration values on measurement performance. Plants were scanned under 0.33° and 0.5°, respectively. The data for angular resolution of 1° and 3° was obtained by taking every second and sixth data point from the data set for 0.5°, respectively. Angular resolutions of 1° and 3° were applied to demonstrate impacts on measurement performance more clearly. During lab tests, the LiDAR was attached at a fixed height of 1803 mm, while the scanning frequency was configured to be 50 Hz, and the cart was manually pushed slowly. Although no exact speed value was measured, we estimated the average speed ranged between 0.09 m/s and 0.12 m/s, which ensured that there was no gap between two consecutive frames. The mounting height value was planned to be the same as the mounting height of field experiments (1824 mm), but since the wooden frame was built manually, the dimension was not maintained well resulting in 21 mm difference.

The system should be able to fully scan cotton plants of various heights within a plausible range. Therefore, the plants used for the lab tests were different heights. The tallest and shortest plants represent the two extreme situations. In lab experiments, the tallest plant was plant 2 with a height of 1295 mm, and a height of 0 mm was used as the shortest plant, which meant that the seed was not geminated. For the lowest height situation, the LiDAR scanned the ground base.

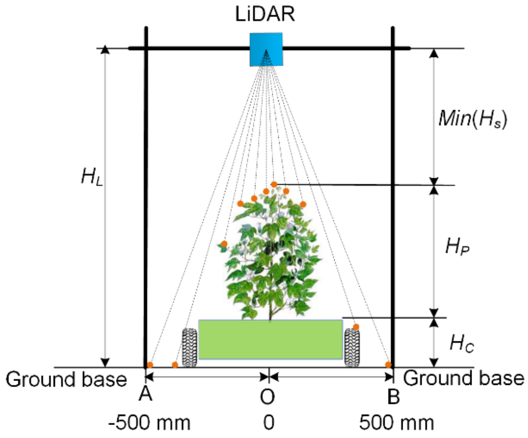

Figure 2.7. Scheme of height measurement for lab tests. The LiDAR was attached on the frame at a height of 1803 mm. Points A and B are two terminal points of the frame at ground base, and O is the projected point of the LiDAR; let O be the original point, A is the position of −500 mm, and B is 500 mm.

Plant 1
Height = 599 mm

Plant 2
Height = 1295 mm

Plant 3
Height = 707 mm

Plant 4
Height = 1038 mm

Plant 5
Height = 512 mm

Figure 2.8. Plants used in lab tests.

The height of the scanned cotton plant was derived using eq (2.9):

$$H_p = H_L - H_C - \min(H_S), \tag{2.9}$$

where H_p is the height of the cotton plant; H_L is the mounting height of the LiDAR (H_L = 1803 mm); H_C is the height of the cart (H_C = 328 mm); and min(H_S) is the minimum distance between the LiDAR and the plant (or the maximum plant height), measured by the point cloud.

2.2.3.2. Field experiment setup

Field tests were conducted in Watkinsville, GA, USA (33.86631°N, −83.54592°E) in autumn of 2015 (Figure 2.9). The maximum wind speed was 16 km/h. At that time, cotton was in mature growth stage. In the field, there were 6 rows, each containing 20 plots. Each plot was sowed with 15 seeds with 152 mm between adjacent seeds. The alley length was 1830 mm and the row space was 914 mm. There were 6 cultivars, which were randomly planted. The start and end point positions for each plot were measured with the RTK-GPS.

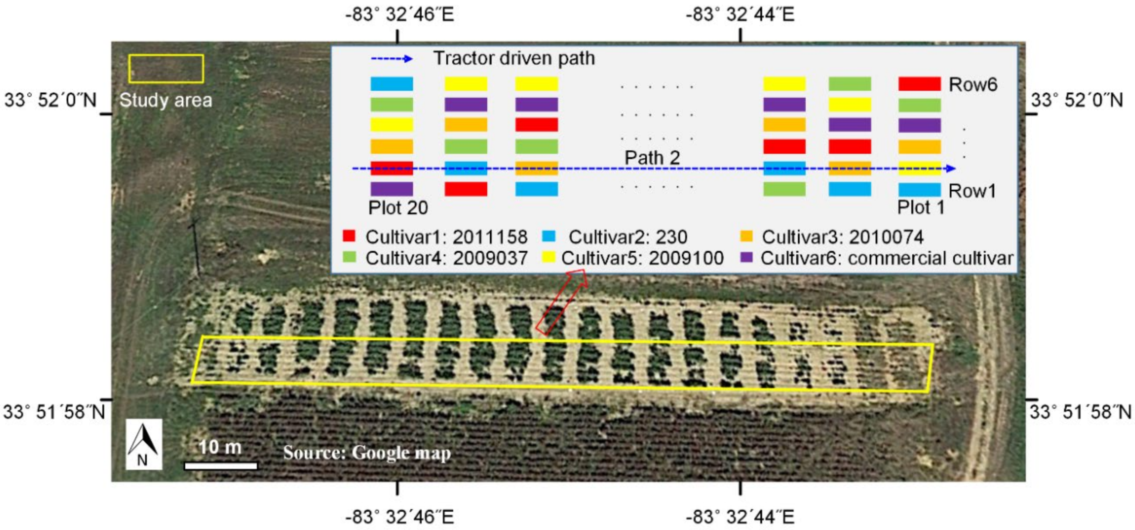

Figure 2.9. Design of field experiments and the moving direction of the tractor.

During data collection, the LiDAR mounting height was 1824 mm with an angular resolution of 0.5° and a scanning frequency of 50 Hz. The tractor was driven down each row from row 1 to row 6 and three rows were simultaneously scanned for each of the four middle paths. For the border paths (along rows 1 and 6), data for only two rows were used for further processing. The speed of tractor was between 0.45 and 0.54 m/s. For field tests, the maximum height of each plot was measured manually to provide a reference. Similar to lab experiments, cotton plant height was measured using a roller tape as the distance between the highest point of the plant and the ground.

2.2.4. Data processing algorithm and performance evaluation

Figure 2.10 illustrates the data processing pipeline for the LiDAR data. Four steps were contained in the method:

Step 1 Read raw data

The LiDAR scanned frames including timestamps, and GPS tags were retrieved from test files by a program developed in MATLAB 2016a. The raw LiDAR data is shown in Figure 2.10a, b.

Step 2 Preprocess the point cloud of LiDAR

The raw data along the *Y* axis was processed using eq (2.10):

$$H_{pt} = H_m - H_{scan}, \tag{2.10}$$

where H_m is the LiDAR mounting height, H_{scan} is the detected distance between each scanned point along the Y axis and the LiDAR, and H_{pt} is the real height value of each scanned point. Distance filters were then used to eliminate out-of-range data along the Y and Z axis. Along the Y-axis direction, the distance filter threshold was determined by the rows scanned by the LiDAR. For example, if three rows were scanned at a time, the threshold would be 1372 mm which is equal to 1.5 times the length of interspace between two rows. Along the *Z*-axis direction, the threshold is set to be the mounting height of the LiDAR; points below the LiDAR were kept. An example of reconstructed 3D point clouds is shown in Figure 2.10c. The *Y* axis was the direction of cross section, the *Z* axis depicted the plant height, and the *X*-axis denoted the tractor's direction of movement. The *Y*-axis and *Z*-axis indicate lengths in millimeters, while the *X*-axis indicates the number of scanned frames since GPS data was not merged.

Step 3 Fuse GPS data with LiDAR data

GPS data was used to make the conversion of the unit of the *X*-axis from the frame number to distance. Let P_{GPS} be the set of collected GPS data, and F_{LiDAR} be the set of the scanned frames of LiDAR (eq (2.11)). The number of GPS points was *N*, and the number of LiDAR frames is *M*. The GPS data and LiDAR data were synchronized using timestamp.

$$\begin{aligned} \mathrm{P}_{GPS} &= \left\{ p_{GPS0}, p_{GPS1}, \cdots, p_{GPS(N-1)} \right\} \\ F_{LiDAR} &= \left\{ f_{LiDAR0}, f_{LiDAR1}, \cdots, f_{LiDAR(M-1)} \right\} \end{aligned} , \tag{2.11}$$

The distance between two adjacent GPS points denoted by ΔP_{GPS} was computed by eq (2.12). f_{LiDAR} and f_{GPS} were the data acquisition frequency of LiDAR and GPS, respectively. In this study, the data acquisition frequency of GPS was $f_{GPS} = 5$ Hz, and LiDAR scanning frequency was $f_{LiDAR} = 50$ Hz. Therefore, there were 10 scanned frames, each containing 381 points (The aperture angle was 190° with angular resolution 0.5°), between every two adjacent GPS points (eq (2.13)). Assume that the tractor was moving at a constant speed during the interval (200 ms) of two adjacent GPS points. The distance of the two adjacent frames within two adjacent GPS points was computed using eq (2.14). Therefore, the position of each LiDAR scanned frame was able to be obtained using eq (2.15). D_{offset} was the offset between LiDAR and GPS. In this study, D_{offset} was fixed during data collection in the field, and the measured point at 0° scanning angle was used to depict the frame position. Figure 2.10d showed the reconstructed 3D model with X-axis indicated by millimeter units. The point cloud of individual plot was retrieved from the 3D model based on the field layout information (Figure 2.9). First, the 3D model was segmented into 20 blocks along the tractor moving direction according to the premeasured start and end points of each row and the length of the plot, and then plots within each block were segmented based on the interspace between two rows.

$$\begin{cases} \Delta\vec{P}_{GPS}(i) = p_{GPS}(i) - p_{GPS}(i-1), & i = 1,2,\cdots N-1 \\ \Delta\vec{P}_{GPS}(0) = \vec{0} & i = 0 \end{cases}, \tag{2.12}$$

$$\alpha = \frac{f_{LiDAR}}{f_{GPS}}, \tag{2.13}$$

$$\vec{d}_i = \frac{\Delta\vec{P}_{GPSi}}{\alpha}, \qquad i = 0,1,2,\cdots N-1' \tag{2.14}$$

$$\begin{gathered} f_{LiDAR}(k) = f_{LiDAR}(i\alpha + j) = p_{GPS}(i) + j \times \vec{d}_i + \vec{D}_{offset} \\ i = 0,1,2,\cdots N-1, j = 0,1,2\cdots 9, k = 0,1,\cdots,M-1 \end{gathered}, \tag{2.15}$$

Step 4 Extract height trait

A canopy height profile (CHP) of one plot (Figure 2.10e) would be derived by calculating the maximum height of each frame. Based on CHP, the maximum height and histograms of canopy height were extracted (Figure 2.10f and g). A threshold of 200 mm was set for the histogram to segment the plants from the ground.

The data processing algorithm was developed and implemented in software MATLAB 2016a (The Math Works Inc., Natick, MA, USA) on a laptop that was used for data collection. The laptop used an Intel i5-4210M CPU 2.60 GHz with 8G RAM, running an operating system of Windows 8.1 Pro. An accuracy assessment of the system was performed to evaluate the performance of the designed system based on the comparison of LiDAR height measurement and manual measurements. The mean error and standard deviation were computed as well as R^2 value and RMSE, and a simple linear regression analysis was conducted. For field experiments, we performed an accuracy assessment of the system using a total of 288 samples. There were 90, 108, and 90 samples for left rows, middle rows, and right rows, respectively. The first and second plots of all six rows did not germinate, so data from 18 plots (plots 3 to 20) in each row were used for processing. An ANOVA test analysis was conducted to investigate the effect of cultivar on height trait. In addition, algorithm efficiency was tested by performing the algorithm for 100 rounds for each tractor's path. The average running time with standard deviations was calculated for each path.

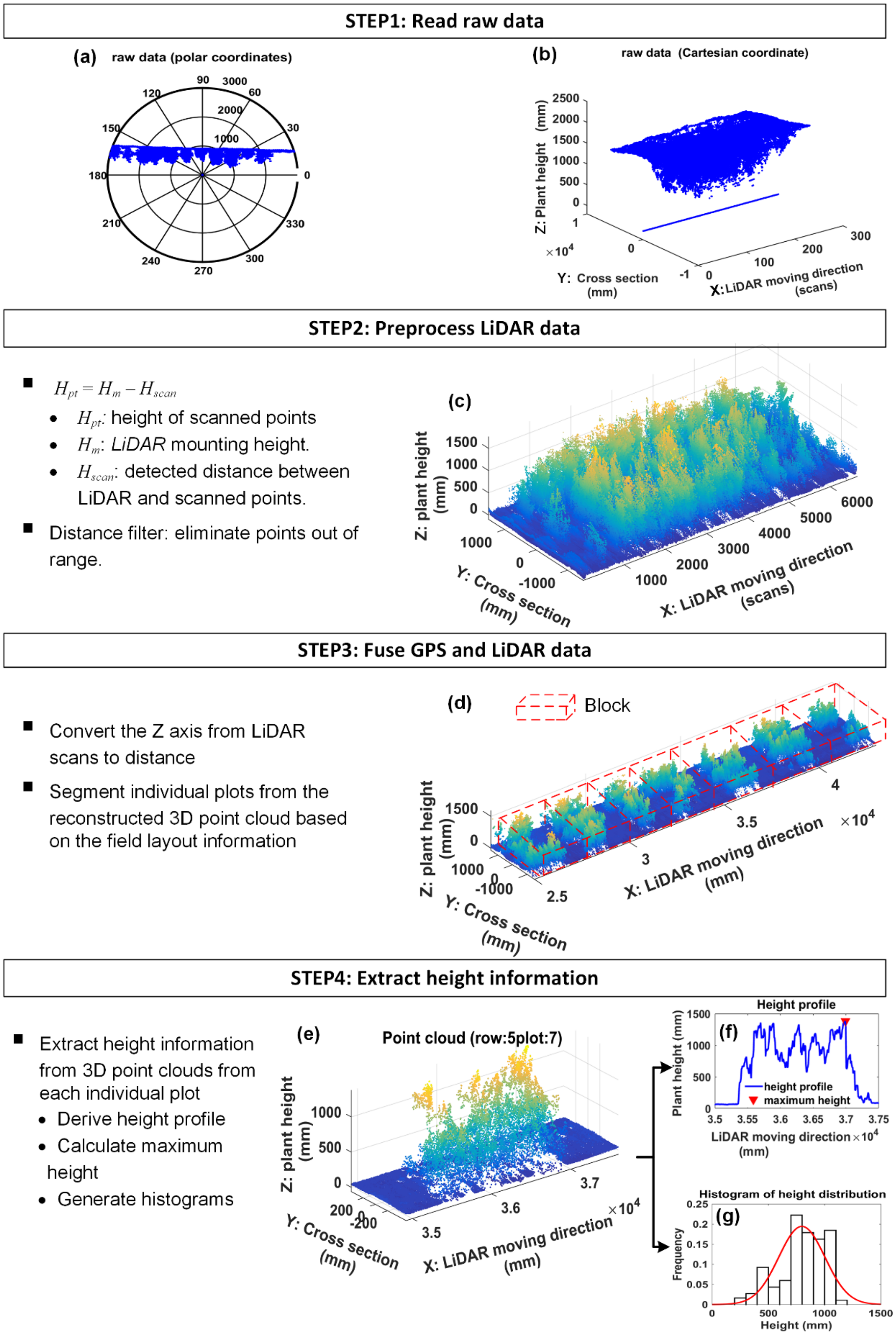

STEP1: Read raw data

STEP2: Preprocess LiDAR data

- $H_{pt} = H_m - H_{scan}$
  - H_{pt}: height of scanned points
  - H_m: *LiDAR* mounting height.
  - H_{scan}: detected distance between LiDAR and scanned points.
- Distance filter: eliminate points out of range.

STEP3: Fuse GPS and LiDAR data

- Convert the Z axis from LiDAR scans to distance
- Segment individual plots from the reconstructed 3D point cloud based on the field layout information

STEP4: Extract height information

- Extract height information from 3D point clouds from each individual plot
  - Derive height profile
  - Calculate maximum height
  - Generate histograms

Figure 2.10. Data processing pipeline for LiDAR point cloud.

2.3 Results

2.3.1. Results of lab tests

Lab experiments showed that the angular resolution must be at least 0.5° in the following two situations: (1) when the plants have not germinated with the ground base level (0 mm) and (2) when the plants fully have developed at a maximum height of 1623 mm. This angular resolution would meet the full coverage requirement: i.e., the diameter of the laser beam (*Φ*) should be greater than the distance between two adjacent laser points (Δ*D*). The height 1623 mm was obtained by combining the height of plant 2 (1295 mm) and the height of the cart (328 mm). As the angular resolution decreased (i.e., from 0.33° to 3°), the diameter of the laser beam did not change noticeably at both heights. At ground level (Figure 2.11a), *Φ* was greater than at 1623 mm (Figure 2.11b) given the same angular resolution, because the scanning distance was longer at ground level. In contrast, Δ*D* increased dramatically as the angular resolution decreased. The line of Δ*D* started to intersect with the line of *Φ* at the angular resolution of 0.5° (indicating Δ*D* > *Φ*) both at the ground level and the elevated height. The results suggest that if an angular resolution lower than 1° was used, a full scan could not be obtained and some parts of the scanned objects would not be covered by the laser, resulting in significant measurement errors.

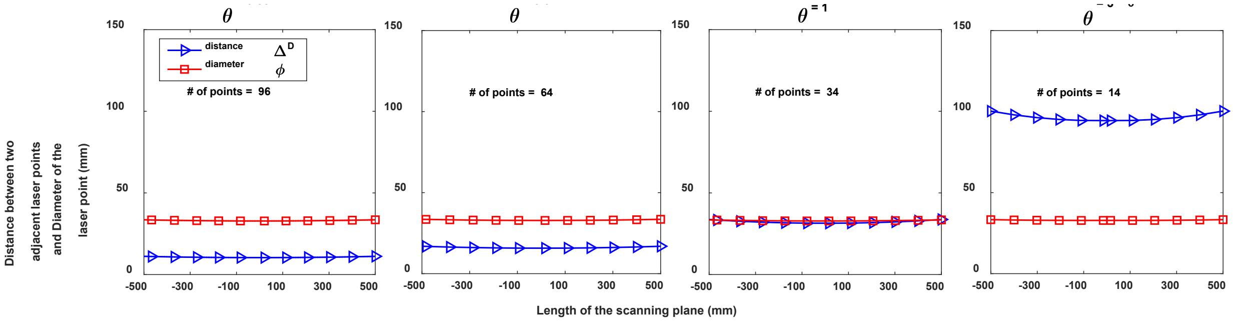

(a)

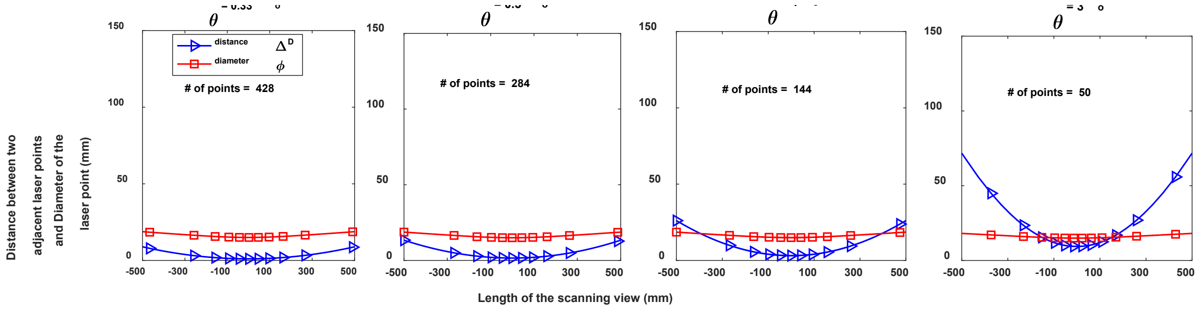

(b)

Figure 2.11. The varying pattern of the laser beam diameter and the distance between two adjacent laser points across a 1000 mm long scanning plane for lab tests at (a) the ground base level (0 mm), and (b) a height level of 1623 mm. The LiDAR was at the height of 1803 mm.

Height measurement results (Table 2.3 and Figure 2.12) in the lab were in a good agreement with the analysis in Section 2.2. The system achieved high accuracies for angular resolutions of 0.33°, 0.5°, and 1°, while performance decreased when the angular resolution was 3° (Table 2.3). For the correlation analysis (Figure 2.12), although the R^2 value was the same for four different angular resolutions, the RMSE for 3° was 7.45 mm which was significantly larger than the value for the other three angular resolutions. If the angular resolution is too low, gaps between two laser points may emerge and this may result in poor measurement performance; if the angular resolution is too high, more storage space and computing resources are needed since more points are generated even though these points may not contribute to enhancing measurement accuracy. Therefore, 0.5° angular resolution was chosen for the lab tests.

The lab tests indicated that the system with fine parameter configurations could measure cotton plant height with high accuracy in the lab (controlled environment). These findings provided useful guidelines for cotton plant height measurement in field conditions.

Table 2.3. Height measurement results using four different angular resolutions in a lab test.

Angular Resolution	**Manual Measurement (mm)**	**Plant No.**					**Mean**
		1	**2**	**3**	**4**	**5**	
		599	1295	707	1038	512	/
0.33°	Height (mm)	598	1296	702	1033	508	/
	Error (%)	−0.14	0.09	−0.68	−0.47	−0.84	−0.41
	Std [1]	2.01	1.72	1.03	4.79	1.38	2.39
0.5°	Height (mm)	600	1292	702	1035	508	/
	Error (%)	0.19	−0.20	−0.71	−0.27	−0.85	−0.37
	Std	3.75	4.21	2.19	3.42	2.83	3.28
1°	Height (mm)	599	1292	702	1035	506	/
	Error (%)	−0.01	−0.26	−0.76	−0.31	−1.26	−0.52
	Std	3.90	4.42	2.51	3.16	3.91	3.58
3°	Height (mm)	595	1289	698	1032	501	/
	Error (%)	−0.67	−0.46	−1.27	−0.58	−2.15	−1.03
	Std	3.18	4.29	2.10	5.02	5.09	3.94

[1] Standard deviation.

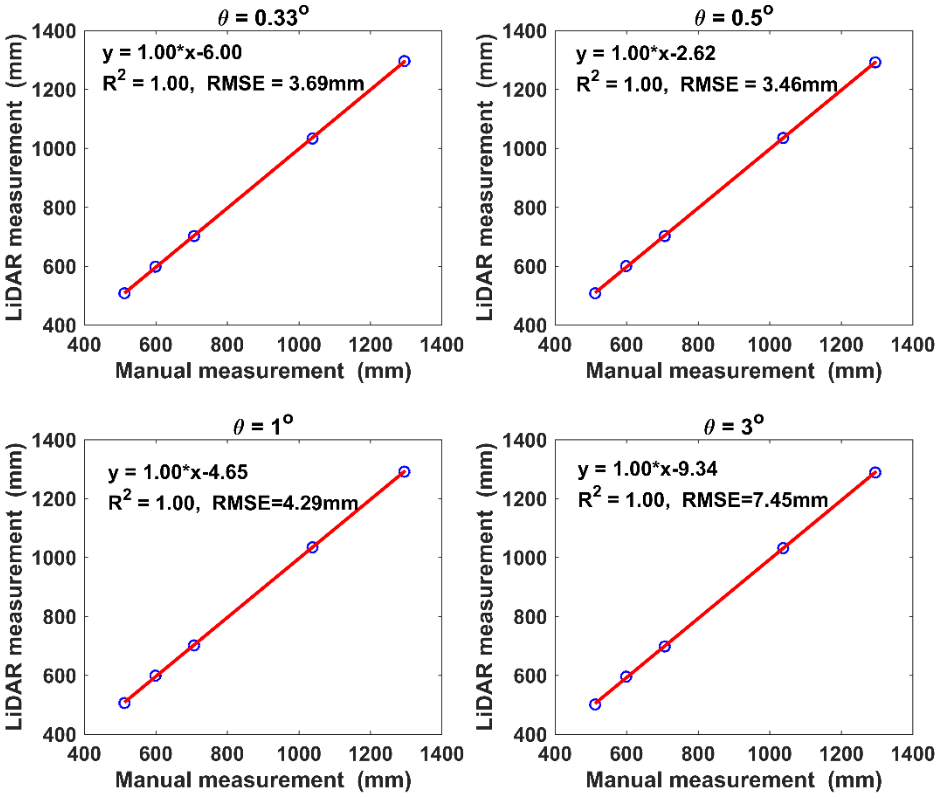

Figure 2.12. Correlation analysis for different angular resolutions.

2.3.2. Results of field tests

Since three rows were scanned for field tests, the corresponding scanning range at ground base level was [−1372, 1372] mm in the horizontal direction (Figure 2.13). The working hypothesis was that the highest points of cotton plants would not be beyond this range. For field tests, there was much variation in plant growth. For example, some seeds may not have germinated in a plot. The angular resolution at ground base level was selected to ensure that the system was able to make a full scan for all situations. When the angular resolution was set at 1° or 3°, the distance between adjacent laser points was greater than the diameter of the laser point in certain parts (for 1°) or in the entire scanning range (3°). When the angular resolution was set at 0.33° or 0.5°, the diameter of the laser point was always greater than the distance between adjacent laser points. Given that both 0.33° and 0.5° produced satisfactory results, the angular resolution was configured to be 0.5° for field tests. The tractor speed varied between 0.45 and 0.54 m/s (1.0 to 1.2 mph) during field data collection. In order to ensure that the system would make a full scan along the moving direction of the tractor (the distance between two consecutive scanning planes being less than the laser point diameter), the frame rate was set to 50 Hz. Therefore, the resolution along the moving direction of the tractor was between 9 and 10.8 mm/frame. This distance between consecutive frames was less than the smallest laser point diameter. Based on the data and analyses, no scanning gap would occur either along the LiDAR scanning plane or along the moving direction of the tractor.

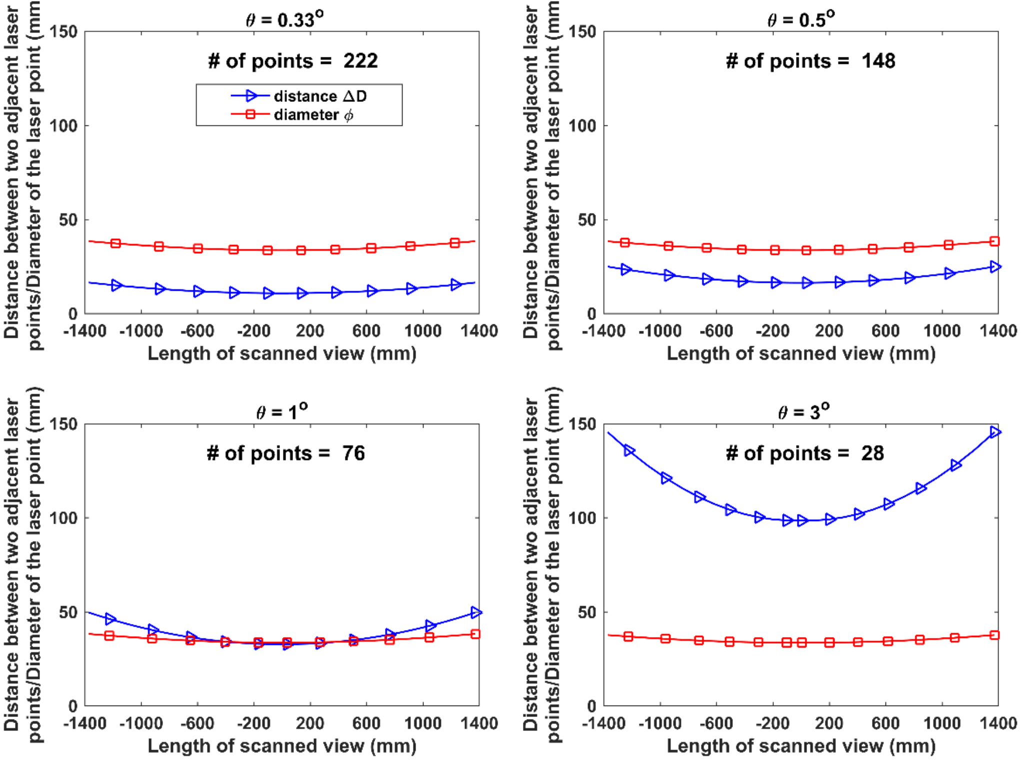

Figure 2.13. The varying pattern of the laser beam diameter and the distance between adjacent laser points across a 2743 mm scanning length for the field tests. The LiDAR was at the height of 1803 mm.

Three plots (left, middle, and right rows) were scanned by the LiDAR simultaneously (Figure 2.14a). The 3D plant model reconstructed from the LiDAR data showed that the scanning points were denser for the middle row (directly below the LiDAR) than the left and right rows (further away from the LiDAR) (Figure 2.14b). It was also observed that the ground plane was not level, with the elevation decreasing from left to right (Figure 2.14a). The uneven ground level would result in a system error for measurement results.

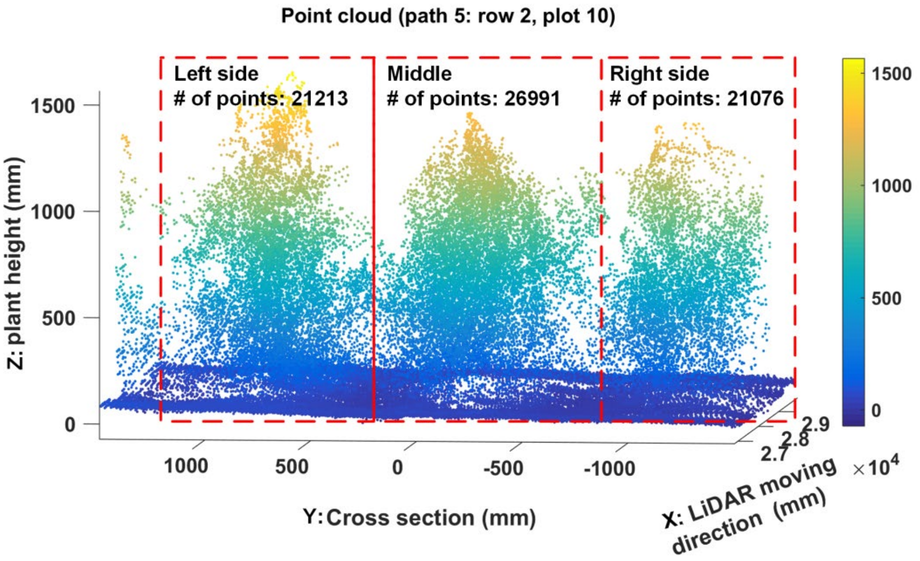

(**a**)

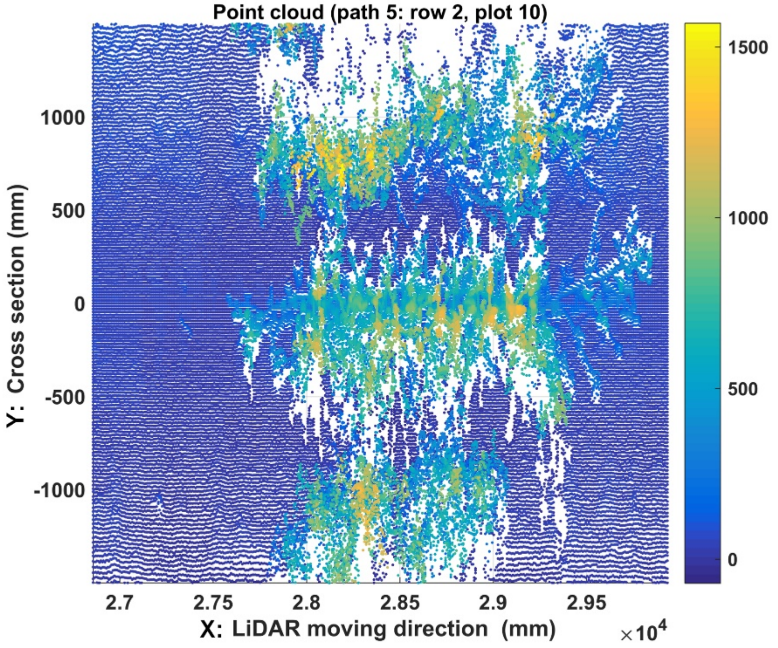

(**b**)

Figure 2.14. Example of 3D reconstruction. (a) 3D view of the 3D structure model; (b) Top view of the 3D structure model.

Overall, the average height error was −0.02% and the standard deviation of the error was 6.84% (Table 2.4), which indicated that plant heights measured by the LiDAR system in naturally illuminated fields were in good agreement with ground truth. The results were also in line with previous studies reported by Zhang and Grift (2012). The system achieved better overall performance for the middle rows than for the left and right rows. For the middle row, the R^2 value was 0.99, the RMSE was 54 mm, and the mean of the error was −0.37%. The means of the error for left and right rows were 0.58% and −2.62%, respectively, which indicated that the system overestimated the height for the left rows and underestimated the height for the right rows. Two factors could contribute to this systematic error: locally uneven ground plane and not well levelled measurement system. These factors could prevent the LiDAR from being parallel to the measured plane. In this study, the measurement system was levelled. However, if the ground plane has a greater gradient or the LiDAR scans a wider range, measurement errors would increase. If necessary, a height normalization process should be applied (Carlone et al., 2015), expressing heights with respect to the local ground plane. In the present study, normalization was not necessary, given that the small slope and the short scanning range would not result in significant negative impact on measurement performance. From the error distribution data (Figure 2.15), we can see the measurement errors followed similar distributions with 92.41%, 93.75%, and 92.50% of the total measurements within ±10% of the measurement error for left side, middle, and right side plots, respectively.

Table 2.4. Statistic results of field tests.

	Overall	**Left Side**	**Middle**	**Right Side**
Mean Error [1] (%)	−0.02	1.34	0.40	−1.86
Std Error [2] (%)	6.84	6.27	6.23	7.69

[1] The mean error; [2] The standard deviation of error.

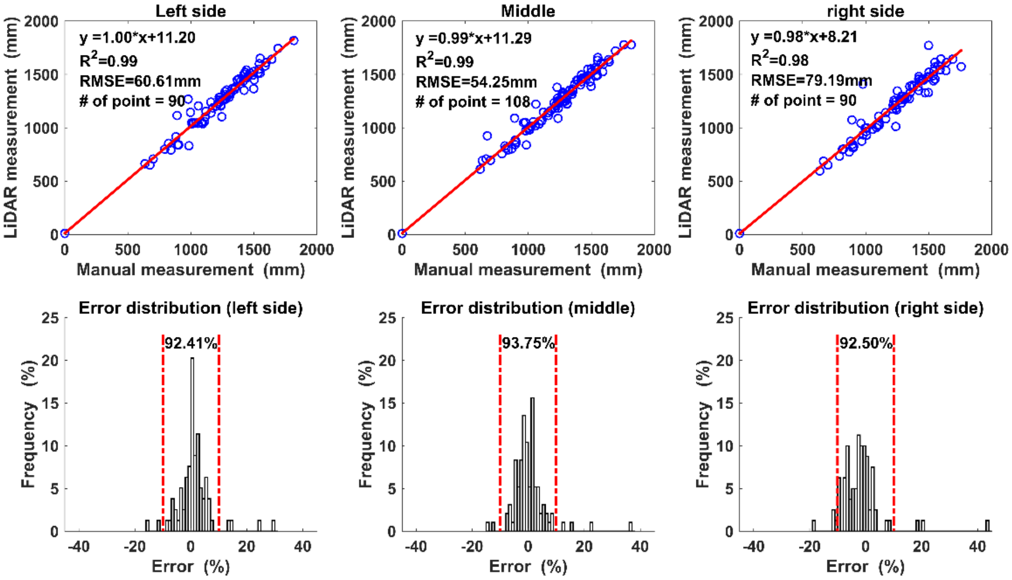

Figure 2.15. Correlation and error analysis between LiDAR and manual measurements. Two vertical dashed lines in the histograms indicate the ±10% error range.

2.4 Discussion

The designed system has been demonstrated to be capable of using LiDAR for data collection in a high throughput fashion under field conditions. In this study, one row in the field tests was about 90 m long and the average tractor speed was about 0.5 m/s. Therefore, it took roughly 3 min to finish collecting data along one path (three rows). For the 6-row field, the HTP system was able to finish data collection in about 6 min. This relatively high throughput was a major benefit of the HTP system, compared to the side view scan utilized in similar studies (Rosell Polo et al., 2009; Zhang and Grift, 2012) and manual measurements. This gain of throughput would be particularly useful if the system was applied in larger fields. If the LiDAR was installed at a higher distance above the plants (Tilly et al., 2015), more rows could be scanned, which would result in even higher throughput. In addition, the proposed data post processing method achieved average running time of 3.22 s for each path with the standard deviation 0.06 s. For the 6-row field, the proposed method could extract the maximum height trait for all plots within 10 s. Each frame of LiDAR data occupied 0.71 KB, and thus the data volume was 35.5 KB/s. Therefore, it was possible to integrate the proposed data analysis method with the proposed system for online height measurement. For the typical experiments mentioned in (White et al., 2012), 20,000 plots are required. If one row has 100 plots, there are totally 200 rows. Assume each plot has the same size to our experimental field. It will take about 16 h to scan the whole field and within 20 min to calculate the maximum height for all plots. Assume a person walks 3 km/h and takes 30 s to measure the height of each plot based on our field work experience, it would need about 200 h to finish all measurements. Mounting the LiDAR at greater height could make the LiDAR scan more rows, however, the likelihood of missing plants would increase. Because if the laser beam is larger than the objects, the total amount of light reflected back to the sensor is not sufficient, the object may not be detected. In addition, faster tractor speed could also improve data collection efficiency, but there was a maximum speed limitation for the tractor since high speed may lead to gaps between two connective frames. This needs to be further explored.

The study has shown that the method to optimize system configurations ensured that the system made full scans without gaps during field data collection. A high quality 3D plant map, which plays a significant role in cotton plant height measurement and other structural traits extraction (Carlone et al., 2015), was reconstructed with the help of an RTK-GPS. Although some outward-facing plant branches in the left and right rows were beyond the scanning range of the LiDAR (Figure 2.14), our system settings ensured that the laser pulses were able to scan most parts of the plants including the highest points. These outlier branches would not result in large errors of height measurement. Crommelinck and Höfle (2016) stated that for crops with homogenous surfaces such as maize, crop height could be measured with low point density. This study has demonstrated that it is necessary to scan with high point density without gaps due to the complex plant structure of cotton plants (Mauney, 1986). In addition, the dense point cloud could also be helpful for plant volume estimation using the partial scanned plants (Auat Cheein et al., 2015).

The LiDAR measurement results were less stable under field than lab conditions, which was mainly attributed to the uncontrolled environment in the field. Wind and the tractor's vibration and movement during data collection could make plants move, leading to inaccurate measurements (Crommelinck and Höfle, 2016). In some unusual cases, errors were around 40%, which could be caused by movements created by tractor or wind during data collection. Weeds were also a major source of noise for LiDAR data, especially at the early growth stage. These factors could be better controlled in the future by weeding before data collection, collecting data on calm days, and mounting the LiDAR in front of the tractor. In addition, more advanced filtering algorithms (Steder et al., 2011) should be applied to reduce noise in the raw data.

The height trait could be used to help plant breeders' select cotton genotypes. For example, plant height is used as an indicator to identify early maturing cotton cultivars (Baloch et al., 2014) that can avoid yield losses due to diseases and insect-pest complexes, and increase economic return by reducing input cost. In this study, histograms of the height distribution showed differences among the six cotton genotypes (Figure 2.16). An ANOVA test showed that the difference was significant (p-value < 0.05). In addition, the height trait also has the potential to predict crop yield and leaf area index (Luo et al., 2015).

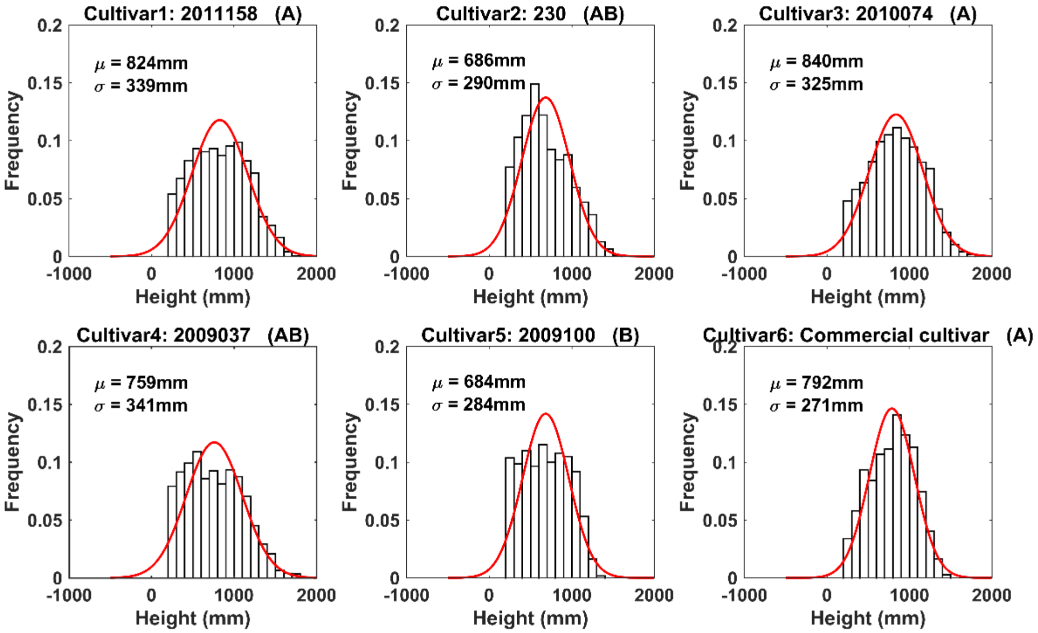

Figure 2.16. Height histograms for six cotton cultivars. Cultivars with the same letter in the title are not significantly different.

2.5 Conclusions

The high-throughput phenotyping system developed in this study accurately measured cotton plant height at the plot level under natural illumination in the field. This is advantageous compared to image based methods that require controlled lighting conditions. In addition, the LiDAR in this system can scan three rows at a time with the current mounting height. More rows could be scanned simultaneously by raising the mounting height of the LiDAR, resulting in even higher throughput. This could be particularly useful for large fields. The system also can be used for height measurement of other crops such as soybean, wheat, and rice. Future work will be focused on measuring other traits—such as crown size, plant volume, and leaf area index—from the reconstructed 3D point cloud model.

CHAPTER 3

IN-FIELD HIGH-THROUGHPUT PHENOTYPING AND COTTON PLANT GROWTH ANALYSIS USING LIDAR[2]

---

[2] Sun, S.; Li, C.; Paterson, A.; Jiang, Y.; Xu, R.; Robertson, J.; Snider, J. *Frontiers in Plant Science* 2018, 9, 1-17. Reprinted here with permission of publisher.

Abstract

Plant breeding programs and a wide range of plant science applications would greatly benefit from the development of in-field high throughput phenotyping technologies. In this study, a terrestrial LiDAR-based high throughput phenotyping system was developed. A 2D LiDAR was applied to scan plants from overhead in the field, and an RTK-GPS was used to provide spatial coordinates. Precise 3D models of scanned plants were reconstructed based on the LiDAR and RTK-GPS data. The ground plane of the 3D model was separated by RANSAC algorithm and a Euclidean clustering algorithm was applied to remove noise generated by weeds. After that, clean 3D surface models of cotton plants were obtained, from which three plot-level morphologic traits including canopy height, projected canopy area, and plant volume were derived. Canopy height ranging from 85th percentile to the maximum height were computed based on the histogram of the z coordinate for all measured points; projected canopy area was derived by projecting all points on a ground plane; and a Trapezoidal rule based algorithm was proposed to estimate plant volume. Results of validation experiments showed good agreement between LiDAR measurements and manual measurements for maximum canopy height, projected canopy area, and plant volume, with R^2 values of 0.97, 0.97, and 0.98, respectively. The developed system was used to scan the whole field repeatedly over the period from 43 to 109 days after planting. Growth trends and growth rate curves for all three derived morphologic traits were established over the monitoring period for each cultivar. Overall, four different cultivars showed similar growth trends and growth rate patterns. Each cultivar continued to grow until ~88 days after planting, and from then on varied little. However, the actual values were cultivar specific. Correlation analysis between morphologic traits and final yield was conducted over the monitoring period. When considering each cultivar

individually, the three traits showed the best correlations with final yield during the period between around 67 and 109 days after planting, with maximum R^2 values of up to 0.84, 0.88, and 0.85, respectively. The developed system demonstrated relatively high throughput data collection and analysis.

3. 1 Introduction

The global population is estimated to approach nine billion by 2050, and demand for food and fiber crops is expected to increase by 60% (Gerland et al., 2014; Tilman et al., 2011). New plant breeding approaches need to be developed to overcome these tremendous challenges. An important step in this direction is to gain a better understanding of the relationship between genotype and phenotype (Goggin et al., 2015; Großkinsky et al., 2015; Rahaman et al., 2015). However, in-field high throughput phenotyping technologies, which can facilitate automatic measurement of phenotypic traits over the entire growing season, are still considered to be a major bottleneck limiting crop improvement (Cobb et al., 2013; Furbank and Tester, 2011).

Plant morphologic traits can often be used for evaluating plant growth (Hosoi and Omasa, 2012; Taheriazad et al., 2016), which determines plant performance in terms of final crop biomass and yield (Dhondt et al., 2013). Several studies showed that morphologic traits such as canopy height and leaf area index (LAI) were strongly related to plant species, type of cultivation, plant growth rate, and final yield (Friedli et al., 2016; Gebbers et al., 2011; Sharma and Ritchie, 2015; Sun et al., 2017). Importantly, plant growth and yield is dependent upon leaf area development, the average photosynthetic efficiency of all leaves in the plant canopy (Gardner, 1985; Krieg and Sung, 1986), and partitioning of dry matter to the harvested portion of the crop (Earl and Davis, 2003).

Thus, plant canopy development should provide some indication of the crop's capacity for growth and yield.

The traditional manual measurement of plant morphologic traits is time consuming, labor intensive, and sometimes destructive. Novel technologies for plant phenotyping in a non-invasive and high throughput manner with high spatial and temporal resolution offer improved efficiency (Dhondt et al., 2013; Furbank and Tester, 2011; Großkinsky et al., 2015). Over the past decade, several non-invasive approaches using sensing technologies were developed for in-field phenotyping (Lin, 2015; Simko et al., 2016). Computer vision was one commonly-used technology. Usually, plant traits were extracted from color (RGB) images. Li et al. (2016) introduced a method for in-field cotton boll detection based on color and texture features using 2D color images. Si et al. (2015) developed a machine vision system to automatically recognize and locate apples; over 89.5% accuracy was achieved. Such 2D image-based methods provide potential to conduct phenotypic measurements with a high spatial resolution, but are limited by plant occlusion. In addition, one major challenge with 2D digital image methods is that image quality is significantly affected by highly variable illumination conditions in the field, which limits automatic data processing (Li et al., 2014).

The use of 3D model-based methods for plant phenotyping are receiving increasing attention, as they permit multiple morphologic traits such as canopy height, plant volume, and LAI to be simultaneously extracted (Bietresato et al., 2016; Gibbs et al., 2017; Vazquez-Arellano et al., 2016) while mitigating plant occlusion. Moreover, 3D models have the potential to assist growers to continuously monitor and quantify plant growth and development, as well as plant responses to environmental stresses. A stereo-imaging based 3D reconstruction system was established to capture rape seedling leaf area and plant height (Xiong et al., 2017); two identical RGB cameras were utilized as an imaging unit. The mean error for leaf area and plant height measurements was 3.68% and 6.18 %, respectively. The system was put in a well-designed box, in which homogenous illumination was provided. Thuy Tuong et al. (2015) developed a 3D reconstruction system based on ten digital color cameras that were mounted on a custom structure, and an illumination system was used to enhance the visual texture of plants from all camera viewpoints. The system produced very high quality, dense, and complete point clouds. However, as both systems were designed for indoor use, they would need to be modified for field applications under natural illumination. 3D models can also be produced by time of flight (TOF) cameras; however, similarly to RGB image based methods, data quality would be significantly affected by sunlight under field conditions, which limits in-field applications. In Busemeyer et al. (2013b) and Jiang et al. (2016) the TOF cameras were mounted inside an enclosure in order to mitigate the influence of sunlight.

LiDAR (light detection and ranging) technology provides an alternative approach for 3D plant model reconstruction. LiDAR is a remote sensing technology to measure the distance between the sensor and an object of interest by illuminating the object with a laser and analyzing the TOF. LiDAR may be the best known and most widely used sensor for 3D canopy reconstruction (Deery et al., 2014; Gibbs et al., 2017). A 2D LiDAR collects two dimensional scans in a measured plane, and a 3D model can be obtained by moving the sensor along the perpendicular direction to the scanning plane. Although the spatial resolution of the 3D model produced by LiDAR is not as dense as those obtained by camera-based methods, it is sufficient for the extraction of most plant morphologic traits (Bietresato et al., 2016; Rosell-Polo et al., 2009; Sun et al., 2017). In Deery et al. (2014), a LiDAR (LMS400, SICK AG, Waldkirch, Germany) with a monochromatic red laser light source was used to generate intensity images of several crops including rice, wheat, and maize. It was concluded that LiDAR is a potential alternative to image-based methods for phenotyping morphologic traits at the plot or plant level under field conditions. Moreover, in contrast to image based methods, the LiDAR based method uses its own light source, mitigating problems with highly variable illumination conditions in the field. In addition, LiDAR can be used with a high scanning frequency and a large scanning range (Lin, 2015). Therefore, LiDAR has excellent potential for in-field plant phenotyping. 3D point clouds can also be generated by some other sensors such as triangulation line scanner (Paulus et al., 2014b) and ultrasonic sensing (Llorens et al., 2011). A very dense 3D model can be reconstructed using a triangulation line scanner and morphologic traits at the organ level could be extracted, however the relatively short working distance limits its application for large plants such as cotton.

Growth dynamics of plant morphologic traits provide important information toward determining plant productivity. Tessmer et al. (2013) described a high-throughput phenotyping platform for plant growth modeling and functional analysis (HPGA). Plant growth curves were generated by the platform, which were used to gain a deeper understanding of energy distribution. Friedli et al. (2016) introduced a terrestrial 3D laser scanner-based plant growth monitoring system which could be used for monitoring canopy height growth for different crops under field conditions. Paulus et al. (2014b) monitored the organ-specific growth dynamics of cereal plants with a high precision triangulation line laser scanner by scanning every 2–3 days. Three morphologic traits including leaf area, stem height, and plant volume were measured, allowing quantification of the growth dynamics of the barley plant.

In the present study, three morphologic traits—canopy height, projected canopy area, and plant volume—of cotton plants were derived based on data collected by a 2D LiDAR. Morphologic trait data was collected and growth analysis was conducted. Several improvements were made over previously mentioned studies. A one-centimeter accuracy level RTK-GPS was used in this study in order to provide accurate spatial coordinates for LiDAR scans so that a precise 3D surface model could be reconstructed, which is important because the model is the basic dataset for further analysis. In addition, analyses of growth dynamics and correlation of morphologic traits with final yield were conducted over the growing season. The system repeatedly scanned plants over the growing season, permitting analysis of the effects of different cultivars on the growth and final yield of cotton plants.

The overall goal of this work was to develop a high throughput phenotyping system for morphologic traits of cotton plants using LiDAR under field conditions. This LiDAR-based system is one component of our broader effort to develop field-based high throughput phenotyping (HTP) systems, and it complements other image-based sensors such as Kinect V2, thermal camera, and hyperspectral camera. This LiDAR-based system provides accurate morphologic traits in a robust and fast way, and saves storage space and computing resources compared to image-based sensors. Specific objectives were to: (1) develop algorithms to extract multiple morphologic traits—canopy height, projected canopy area, and plant volume—from a 3D point cloud obtained with a 2D LiDAR; (2) conduct 4D monitoring (3D plant reconstructions over time) of the derived plant morphologic traits to detect growth patterns of plants from different cultivars; and (3) explore relationships between derived morphologic traits and final yield.

3.2 Materials and Methods

3.2.1 Experimental field

The study site was located at the Iron Horse Farm (IHF) in Greene County, GA, USA. The entire study included 128 plots arranged in 16 rows and 8 columns (Figure 3.1a), using a randomized complete block design with four cultivars of cotton and 32 replicate plots per cultivar. Four plots of each cultivar were planted in each column. The distribution of cultivars in each column was randomly assigned (Figure 3.1b). Plots were 3.05 m wide. A total of 15 seeds were sowed in each plot at spacing of 0.15 m. Inter-row spacing was 1.52 m, and inter-column spacing was 1.83 m. Cotton seeds were sowed on June 13, 2016.

The four cotton cultivars were GA2011158 (cultivar 1), GA2009037 (cultivar 2), GA2010074 (cultivar 3), and UA48 (cultivar 4) which is commercialized by the private seed company Americot. All four cultivars were developed by conventional breeding possessing no transgenic insects or herbicides tolerant traits. However, they have different fiber quality, growth habits, and plant architecture due to adaptation to different production regions. Cultivars 1, 2, and 3 are elite breeding lines developed by the University of Georgia cotton breeding program for adaptation to the southeastern cotton production region, bred to have indeterminate growth habit to take advantage of the long growing season in the southern US cotton belt. Plants from these cultivars will continue adding vegetative growth at the same time as the reproductive development, therefore they can grow excessively tall and rank in high nitrogen environment or if there are severe insects damage causing excessive square loss. Cultivar 4, on the other hand, was released by the University of Arkansas cotton breeding program, bred to have an early maturity growth habit for adaptation to the northern region of the US cotton belt. It has a determinate growth habit which resulting in shorter statured, extended sympodial branches, and shorter flowering date.

(a) Aerial view of the experimental field

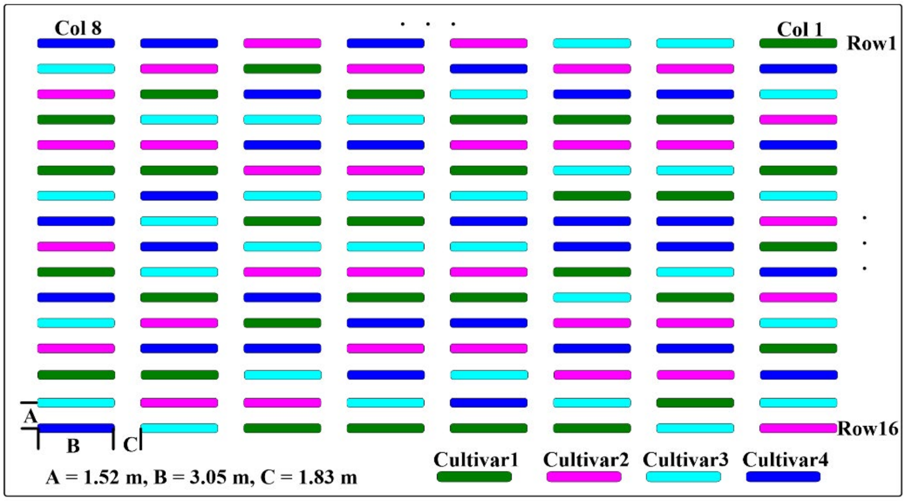

(b) Field layout information and cultivars planted in the experimental site

Figure 3.1. Experimental field layout. (a) Aerial view of the experiment field; (b) illustration of experimental design with cultivar and field layout information.

3.2.2 Data acquisition

The data collection system mainly consisted of a LiDAR (LMS 511 PRO SR, SICK AG, Waldkrich, Germany) (Figure 3.2a), an RTK-GPS (Cruizer II, Raven Industries Inc., Sioux Falls, SD, USA) (Figure 3.2b), and a rugged laptop as a DAQ (data acquisition) and storage device. The LiDAR was mounted on a tractor (Spider DL, LeeAgra, Inc, Lubbock, TX, USA) platform at a height of 2.4 m to scan cotton plots from directly above (Figure 3.2c). The RTK-GPS was mounted on the roof of the tractor, which provided the spatial coordinates during data collection. The LiDAR and RTK-GPS receiver were aligned to the center of the tractor (Figure 3.2d).

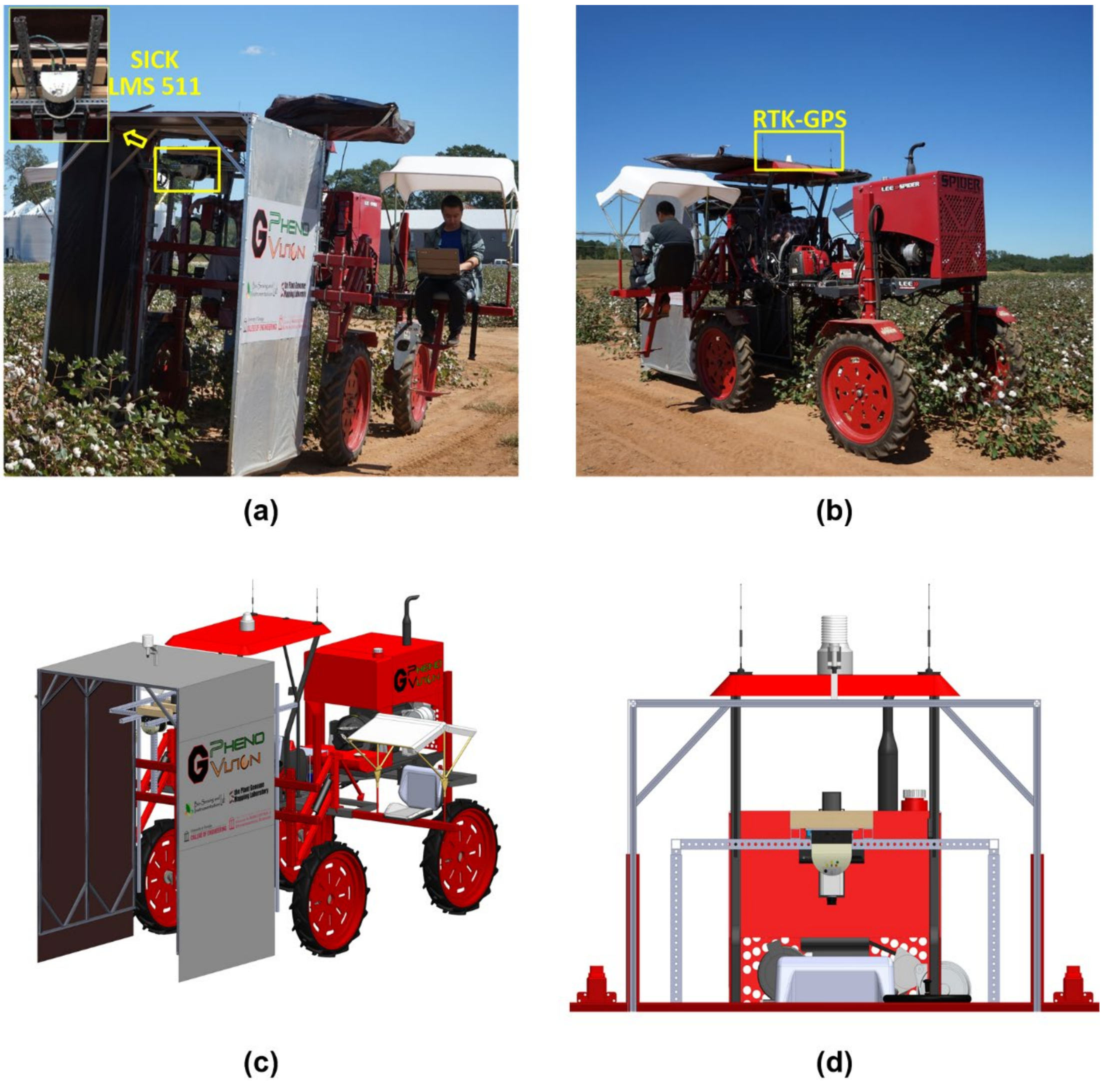

Figure 3.2. Data collection platform. (a) Front view; (b) back view; (c) 3D model of data collection platform; (d) zoomed view of sensors. The consent obtained from the depicted individual for the publication of these images was both informed and written.

The LiDAR was developed for outdoor use, and measured in 2D radial coordinates from -5–185° with a maximum range of 80 m. Line scans could be acquired at a rate of 25–100 Hz with an angular resolution of 0.1667–1°. The built-in filters eliminated interference from particles of dust, raindrops, and snowflakes. An enclosure was used to provide a controlled environment for data acquisition. The RTK-GPS provided coordinates with 1 cm accuracy with an update rate up to 10 Hz.

Data collections were conducted in the field from July 26 to September 30, 2016, i.e., from 43 to 109 days after planting (DAP) (Table 3.1). When scanning plants, the angular resolution of the LiDAR was configured to be 0.33° with a sampling frequency of 50 Hz, and the echo filter and particle filter were enabled. The update frequency of the RTK-GPS was 5 Hz. The tractor scanned the field row by row. For each row, the tractor travelled from column 1 to column 8 with an average speed of about 0.5 m/s. Since the first two sample dates—July 26 and 28—were close to each other, the data for July 26 were not presented except for growth rate analysis.

Table 3.1. Summary of data collection dates (Year: 2016)

Period	**P1**	**P2**	**P3**	**P4**	**P5**	**P6**	**P7**	**P8**
Date	26 July ~ 28 July	28 July ~ 04 Aug	04 Aug ~ 19 Aug	19 Aug ~ 26 Aug	26 Aug ~ 09 Sep	09 Sep ~ 16 Sep	16 Sep ~ 23 Sep	23 Sep ~ 30 Sep
DAP	43~45	45~52	52~67	67~74	74~88	88~95	95~102	102~109

3.2.3 Data processing algorithms

After raw data was collected in the field, further processing and analysis were performed in the lab. The data processing and analysis program was developed and implemented in MATLAB 2016b (The Math Works Inc., Natic, MA, USA) on a desktop equipped with an intel I7-6700 CPU 3.40 GHz with 16 GB RAM, running on a Windows 10 Enterprise operating system.

Two steps were executed to derive plant features (Figure 3.3): 3D plant surface model generation (section 3.3.1) and morphologic plant parameter extraction (section 3.3.2).

3.2.4 Generation of 3D model

The 3D model for each row was reconstructed based on GPS and LiDAR data. The GPS and LiDAR dataset was depicted by eq. (3.1). The two kinds of data were synchronized using timestamps.

$$\begin{aligned} \boldsymbol{P}_{GPS} &= \{P_{GPS0}, P_{GPS1}, \cdots, P_{GPS(N-1)}\} \\ \boldsymbol{F}_{LiDAR} &= \{F_{LiDAR0,} F_{LiDAR1,\cdots,} F_{LiDAR(M-1)}\} \end{aligned} \tag{3.1}$$

$\boldsymbol{P}_{\mathrm{GPS}}$ was the set of collected GPS data, and $\boldsymbol{F}_{\mathrm{LiDAR}}$ was the set of scanned frames of LiDAR. The number of GPS points was *N*, and the number of LiDAR frames was *M*.

The distance between two adjacent GPS points, denoted by $\Delta\boldsymbol{P}_{\mathrm{GPS}}$, was computed by eq. (3.2). f_{LiDAR} and f_{GPS} were the data acquisition frequency of LiDAR and GPS, respectively. In this study, the data acquisition frequency of GPS was f_{GPS} = 5 Hz, and LiDAR scanning frequency was f_{LiDAR} = 50 Hz. Therefore, there were 10 scanned frames, each containing 571 points (the aperture angle was 190° with angular resolution 0.33°) between every two adjacent GPS points (eq. (3.3)). Assuming that the tractor was moving at a constant speed during the interval (200 ms) of two adjacent GPS points, the distance of the two adjacent frames within two adjacent GPS points was computed using eq. (3.4). Therefore, the position of each LiDAR scanned frame was obtained using eq. (3.5). $\boldsymbol{D}_{\mathrm{offset}}$ was the offset between LiDAR and GPS. In this study, $\boldsymbol{D}_{\mathrm{offset}}$ was fixed during data collection in the field, and the measured point at 0° scanning angle was used to depict the frame position.

$$\begin{cases} \Delta\vec{P}_{GPS}(i) = p_{GPS}(i) - p_{GPS}(i-1), & i = 1,2,\cdots N-1 \\ \Delta\vec{P}_{GPS}(0) = \vec{0} & i = 0 \end{cases} \tag{3.2}$$

$$\alpha = \frac{f_{LiDAR}}{f_{GPS}} \tag{3.3}$$

$$\vec{d}_i = \frac{\Delta\vec{P}_{GPSi}}{\alpha}, \qquad i = 0,1,2,\cdots N-1 \tag{3.4}$$

$$\begin{gathered} f_{LiDAR}(k) = f_{LiDAR}(i\alpha + j) = p_{GPS}(i) + j \times \vec{d}_i + \vec{D}_{offset} \\ i = 0,1,2,\cdots N-1, j = 0,1,2\cdots 9, k = 0,1,\cdots, M-1 \end{gathered} \tag{3.5}$$

More details related to this processing can be found in (Sun et al., 2017). Figure 3.3a shows an example of the reconstructed 3D model of one scanned row. A distance filter was used to remove points hitting the enclosure. A plot level 3D model was extracted from the 3D model of the row according to the proportions of the field layout (Figure 3.3b). The standard RANSAC algorithm was applied to cut-off points of the ground plane (Figure 3.3c and 3d). An Euclidean clustering algorithm (Rusu et al., 2008) was used to remove points generated by weeds that were not attached to cotton plants (Figure 3.3e).

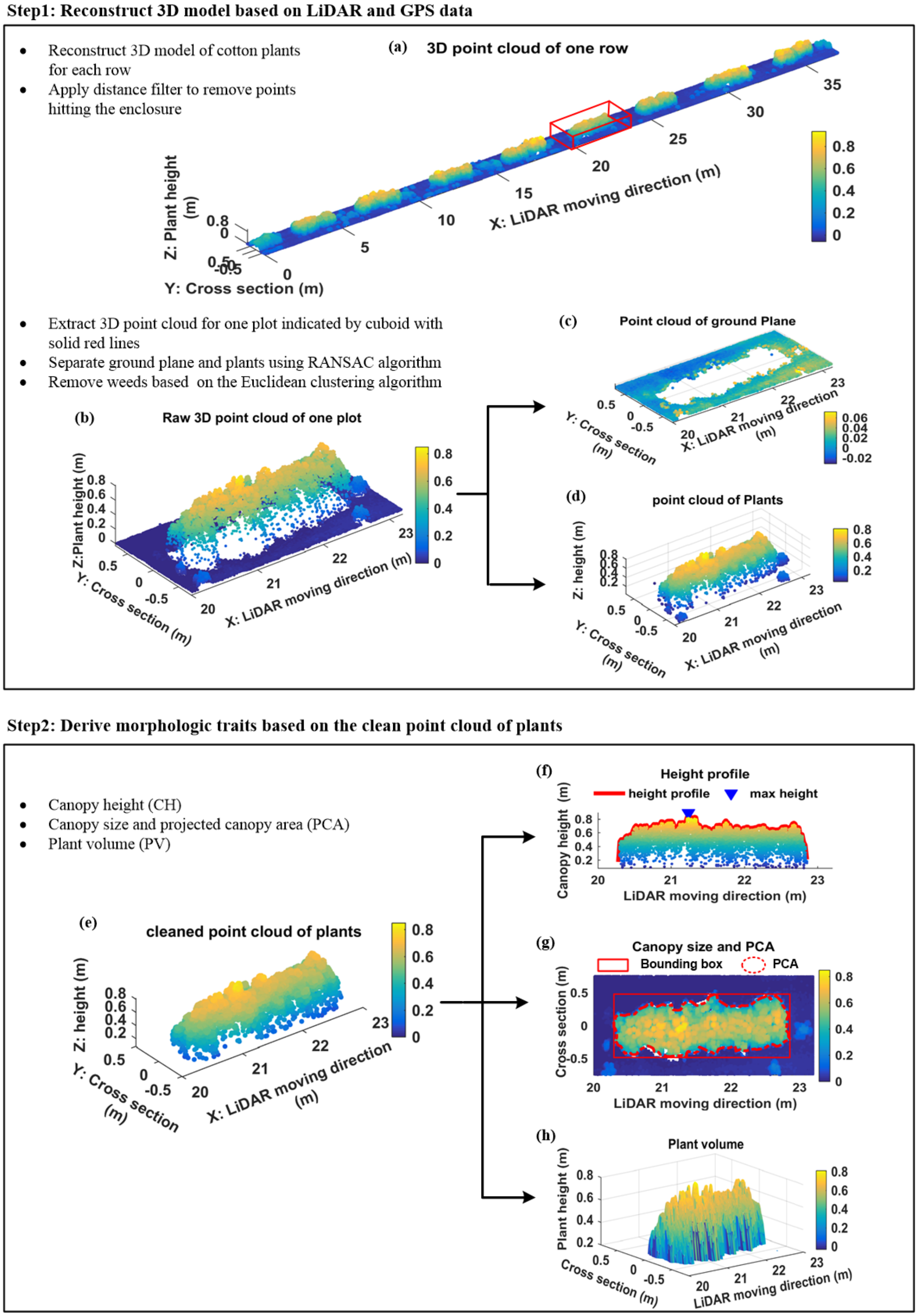

Figure 3.3. Data processing pipeline

3.2.5 Extraction of morphologic traits

The maximum canopy height (CH) was measured by calculating the distance from the ground plane to the apex of all measured points (Figure 3.3f). In addition, different percentiles canopy height—from 85th to maximum CH with steps of 3%—were calculated based on the histogram of the *z* coordinate for all measured points. The boundary points of the plant canopy were detected by projecting all points onto the ground plane, and the projected canopy area (PCA) and bounding box of canopy structure (representing maximum length and width occupied by the canopy) were extracted from boundary points (Figure 3.3g). A Trapezoidal rule based algorithm was used to calculate plant volume (PV) (Figure 3.3h) in order to provide an indication of the 3D space occupied by each plot.

$\boldsymbol{S}$ denoted the line scan set for a plot (eq. (3.6)) which contained k line scans. For a scan s_i which contained n measured points, the dashed line was the surface profile and the red spots were measured points by LiDAR (Figure 3.4). The area denoted as A_i under the line scan s_i could be estimated using the measured points (red spots in Figure 3.4) based on Trapezoidal rule (eq. (3.7)), where (x_i, y_i) were the coordinates of the ith measured point.

$$\boldsymbol{S} = \{s_1, s_2, \cdots, s_k\} \tag{3.6}$$

$$A_i = \sum_{j=1}^{n-1} \left(x_{j+1} - x_j\right)\left(\frac{y_{j+1} + y_j}{2}\right) \tag{3.7}$$

Therefore, the area set denoted as $\boldsymbol{A}$ for the plot was obtained using eq. (3.8).

$$\boldsymbol{A} = \{A_1, A_2, \cdots, A_k\} \tag{3.8}$$

Similar to the area calculation process, PV was obtained with eq. (3.9).

$$\mathrm{PV} = \sum_{i=1}^{k-1}\left(l_{i+1} - l_i\right)\left(\frac{A_{i+1} + A_i}{2}\right) \tag{3.9}$$

l_i was the position along the tractor moving direction of the ith line scan.

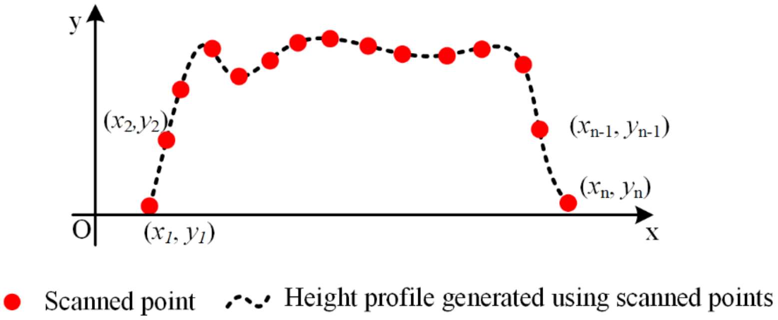

Figure 3.4. Estimated area (the area under height profile curve) using Trapezoidal rule

3.2.6 Validation experiments

To verify the accuracy of canopy height measurements using point cloud data, 96 samples of maximum CH—the perpendicular distance from the highest point to the ground plane—were manually measured using a tape measure during data collection in the field. The samples were measured on four different days: July 28, August 04, August 26, and September 09, 2016. On those days, the average wind speeds were around 2.7 m/s, 3.4 m/s, 2.3 m/s, and 2.5 m/s, respectively.

For PCA validation experiments, eight 'dummy plants' were made with different canopy shapes using printed paper leaves and metal wires. The dummy leaves were in three different sizes—10 cm^2, 41 cm^2, and 92 cm^2—and there were six of each size. The leaves of two dummy plants were arranged to be overlapped. Each dummy plant was scanned by LiDAR and imaged by a DSLR camera (FUJIFILM X-A10 mirrorless camera, FUJIFILM, Tokyo, Japan). A scale bar was used to calibrate the real size of the plant. The ground truth of PCA was computed by segmenting leaves based on color information.

For PV validation experiments, eight plants at different growth stages were used, among which five were real cotton plants, one was a shrub plant, and two were dummy plants. The six real plants were in the leaf and canopy development growth stage, whereas the two dummy plants were used to mimic flowering and boll development growth stages. Each plant canopy was divided into 50 mm cylindrical discs from the top to the bottom and the diameter of each disc was manually measured using a tape measure. The diameter and height of each cylindrical disc were used to estimate the volume of each disc, and then the volume of the canopy was obtained by summing the volumes of each disc. Manual measures of the three traits were plotted versus point cloud estimates, and regression analysis was used to compute the root mean square error (RMSE) and coefficient of determination (R^2).

3.2.7 Plant growth analysis

Plant growth dynamics were obtained by monitoring plants over the growing season when plant morphologic traits were extracted. Growth trends and growth rates for each morphologic trait noted above (CH, PCA, PV) were computed and analyzed over the monitoring period. Growth trends were determined as the variation in measured traits over the monitoring period. The results were given as mean values and standard deviations of all morphologic parameters. A three-parameter logistic model (3PLM) was used to fit growth curves of the three detected traits for each cultivar (Tessmer et al., 2013). The model is a function of time *t* as shown in eq (3.10).

$$y(t) = \frac{x_0 x_n}{x_0 + (x_n - x_0)e^{-\tau(t-T)}} \tag{3.10}$$

where t was the time which was denoted by days after planting in this study, τ was a coefficient, $y(t)$ was detected traits at time t, x_0, x_n were the initial value and the upper horizontal asymptote of the detected trait, respectively, and T was the first day of data collection which was also denoted by days after planting (in this study $T = 45$). x_0, x_n and τ can be estimated using non-linear least squares based on the observations of the detected traits.

Growth rate was determined as the average change in measured traits over a time interval. Growth rate was calculated by eq. (3.11).

$$GR = \frac{P_t - P_{t-\Delta t}}{\Delta t} \tag{3.11}$$

where GR was the growth rate, Δt was the time internal, P_t was the measured plant trait at time t.

3.2.8 Correlation analysis between morphologic traits and yield

Seed cotton (mature fiber plus seeds to which it was attached) was harvested manually on November 4, 2016, and yield was expressed as g/plot. In order to explore the relationship between derived morphologic traits and final yields, linear regression analysis was conducted for each cultivar over the monitoring period. The coefficient of determination (R^2) was computed.

3.3 Results

3.3.1 Morphologic traits extraction and validation

Morphologic trait information of cotton plants was derived from the reconstructed 3D point clouds. Figure 3.5 shows the 3D point clouds over time compared to the 2D color images of the same plot. The reconstructed 3D point clouds on August 19, August 26, and September 9, respectively, were obtained using 207, 256, and 263 scans and contained 11,403, 14,379, and 14,485 points. The cuboids indicated by solid red lines for graphs in row 2 of Figure 3.5 are 3D bounding boxes and points within the cuboids belong to plants. The rectangles indicated by red solid lines for graphs in row 3 of Figure 3.5 are 2D bounding boxes, and the dashed red lines are the detected boundaries from which PCA was derived. Morphologic traits including CH, PCA, and PV were extracted from the 3D point clouds.

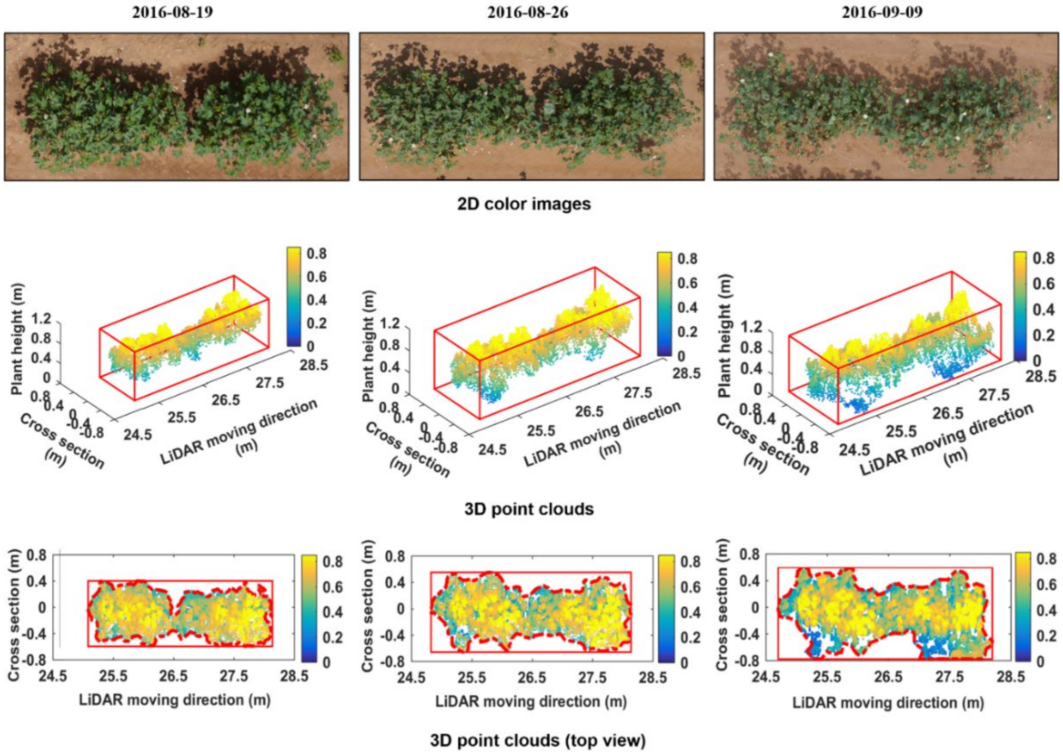

Figure 3.5. Reconstructed 3D point cloud of one plot (Plot ID: row 8, column 6) and its evolution from August 19 to September 09, 2016. The first row shows 2D color images taken from above. The second row shows the reconstructed 3D point clouds of cotton plants. The third row shows height maps of cotton plants, obtained by projecting all points on the ground plane (color indicates height).

CH, PCA, and PV values derived from LiDAR data were highly correlated with manually measured values, with R^2 values of 0.97, 0.97, and 0.98 and RMSE values of 0.03 m, 0.007 m^2, and 0.011 m^3, respectively (Figure 3.6).

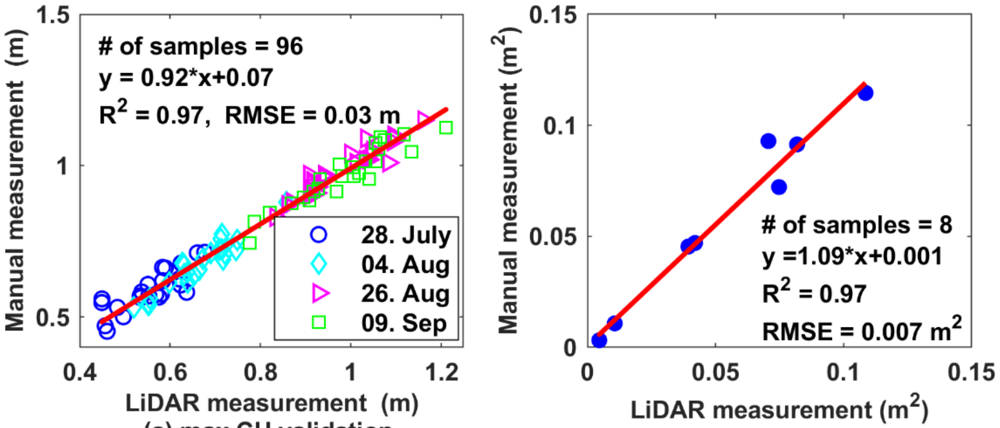

(a) max CH validation

(b) PCA validation

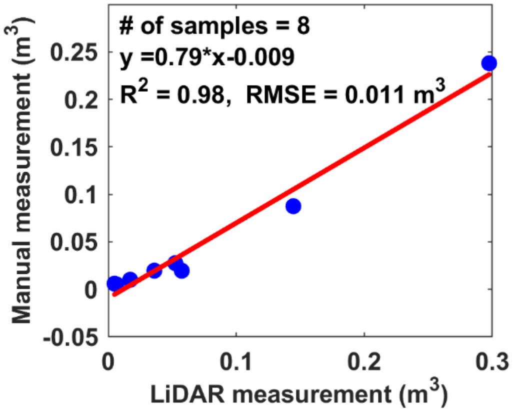

(c) PV validation

Figure 3.6. Comparison of maximum CH, PCA, and PV values based on LiDAR data with ground-truthing.

Figure 3.7a shows the side view of the point cloud of the plot presented in Figure 3.5. The data was collected on August 19 and consisted of 207 line scans. The number of measured points for each line scan varied depending on the width of plants. A total of 66 points were measured for the 144th scan (Figure 3.7b). Points near the center were denser than points located at two terminal areas because the inter-distance between two adjacent points increased with increasing distance between the LiDAR and measured points. A minimum threshold of 0.05 m was applied to remove points. Based on the proposed PV calculation method, the area under the profile and PV were estimated: $A_{144} = 0.52$ m^2, PV = 2.33 m^3 (Figure 3.7c).

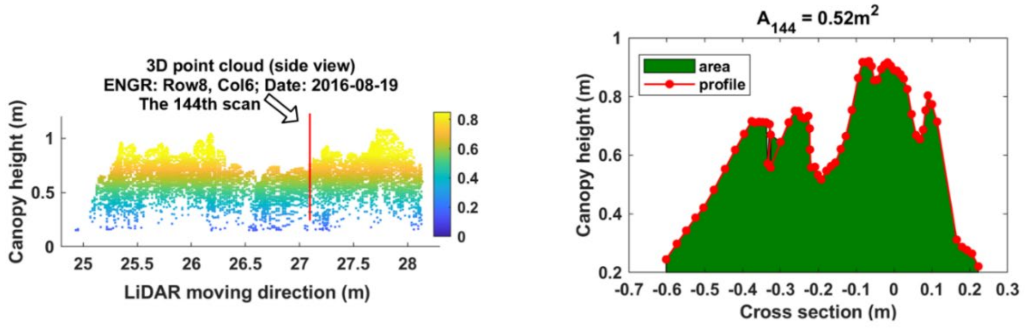

(a) 3D point cloud from side view

(b) Estimated area of the 144th scan

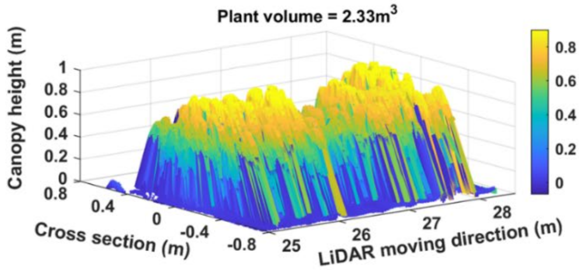

(c) Estimated volume of the scanned plot

Figure 3.7. Example of plant volume computation of a plot (plot ID: row 8, column 6, Date: August 19, 2016) using the proposed Trapezoidal rule based method. (a) Side view of 3D point cloud; (b) estimated area under the profile of scan 144; (c) computed plant volume.

3.3.2 Plant growth analysis

Overall, the three measured morphologic traits—CH, PCA and PV—showed similar growth trends over the monitoring period based on the measurements from the sensor, but the actual value was cultivar specific for each trait (Figure 3.8). For maximum CH, all cultivars reached the maximum height on around day 88. Cultivar 1 and 2 had similar average maximum heights of 1.08 m, while cultivars 3 and 4 reached the peak values of 0.96 m and 0.88 m, respectively. Cultivar 1 and 2 were around 22.7% higher than cultivar 4. PCA continued to increase until around 95 DAP, which was 7 days longer comparted to maximum CH. The maximum PCAs of cultivars 1, 2, 3, and 4 were 2.73 m^2, 2.23 m^2, 2.47 m^2 and 2.34 m^2, respectively. Cultivar 1 had much larger PCA value than the other three cultivars which had similar PCA. It is around 22.4% larger than cultivar 2 which had the minimum area. Cultivar 2 showed the highest CH, but lowest PCA over the whole monitoring period due to less horizontal canopy expansion in the horizontal direction. For the growth curve of PV, the maximum points for all four cultivars were reached on day 88, they were 2.75 m^3, 2.17 m^3, 2.11m^3 and 1.59 m^3 for cultivar 1, 2 3, and 4. Larger differences among cultivars were observed for PV than PCA. The maximum volume was around 73.0 % larger than the minimum one. In summary, cultivar 1 had the largest canopy (highest PV, CH, and PCA) while cultivar 4 had the lowest maximum CH and PV. Although cultivar 2 had high maximum CH, its PCA was the lowest, making its PV in the middle range among the cultivars. The derived values and variation of morphologic traits over time were in good agreement with the developmental phases of cotton (Ritchie et al., 2007).

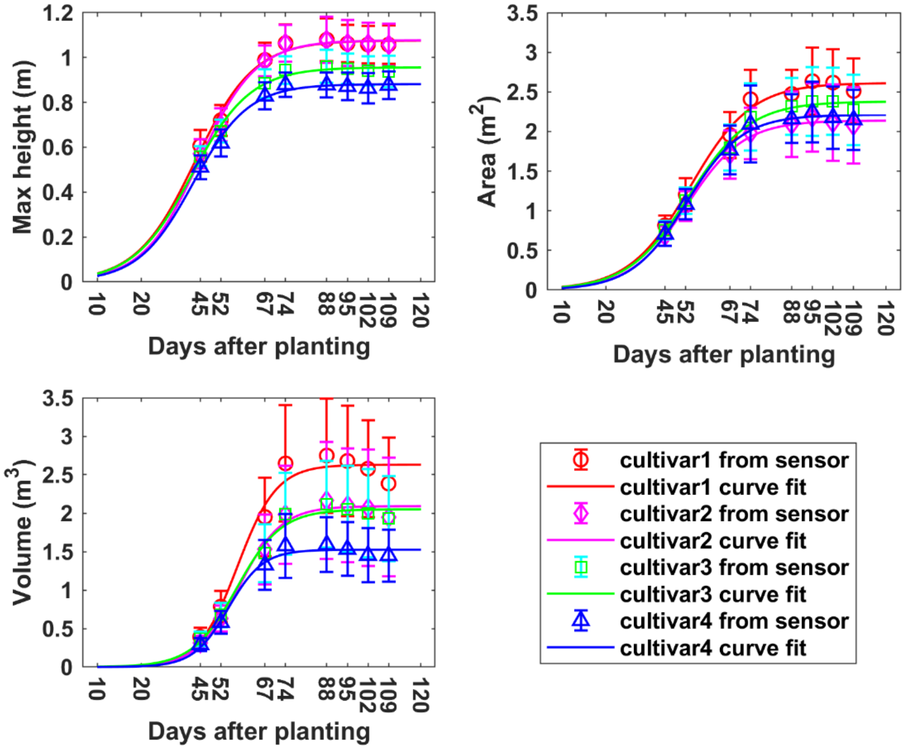

Figure 3.8. Growth curves for derived morphologic parameters over the monitoring period. (a) Maximum canopy height; (b) projected canopy area; (c) plant volume.

Growth curves generated for each cultivar of all three detected traits showed good correlation with the sensor measurements. The date when the traits reached their upper horizontal asymptotes and the values of their upper horizontal asymptotes were similar to the results obtained from measured data. The growth curve varied little after reaching the upper horizontal asymptotes, while the sensor measurements showed a decreasing trend which was mainly due to defoliation.

Figure 3.9 shows the growth rates of maximum CH, PCA, and PV at different periods of time. For maximum CH, cultivars 1 and 2 had similar growth rates, and grew faster than cultivars 3 and 4 during the period from P1 to P5. The peak of GR of cultivar 1 and 2 was observed during P3 (between 52 and 67 DAP), which was around 0.018 meters per day (m/d); However, it was during P2 for cultivar 3 and 4, which was around 0.015 m/d (Figure 3.9a). For PCA, all four cultivars had similar GR during P2 and P3; However, large differences emerged during the period from P3 to P6. The peak of GR for cultivar 1 and 3 was in P4, with the values of 0.065 m^2/d; while it was in P2 for cultivar 2 and 4, with the same value of 0.054 m^2/d. PCA increased until P6 (95 DAP) and then started to decrease (Figure 3.9b), 21 days later than the period when the maximum CH started to decrease. During the PCA increasing period, cultivar 1 grew faster than the other three. PV had a faster GR than the other three cultivars during P1 to P4—it reached the peak in P4 with the value of around 0.1 m^3/d. Cultivar 2, 3 and 4 reached the peak of GR in P4 (0.06 m^3/d), P4 (0.07 m^3/d), and P3 (0.05 m^3/d), respectively. In summary, the fastest GRs for all three traits were during P2 to P4, that was from 45 to 74 DAP, which was also indicated by the growth curves in Figure 3.8.

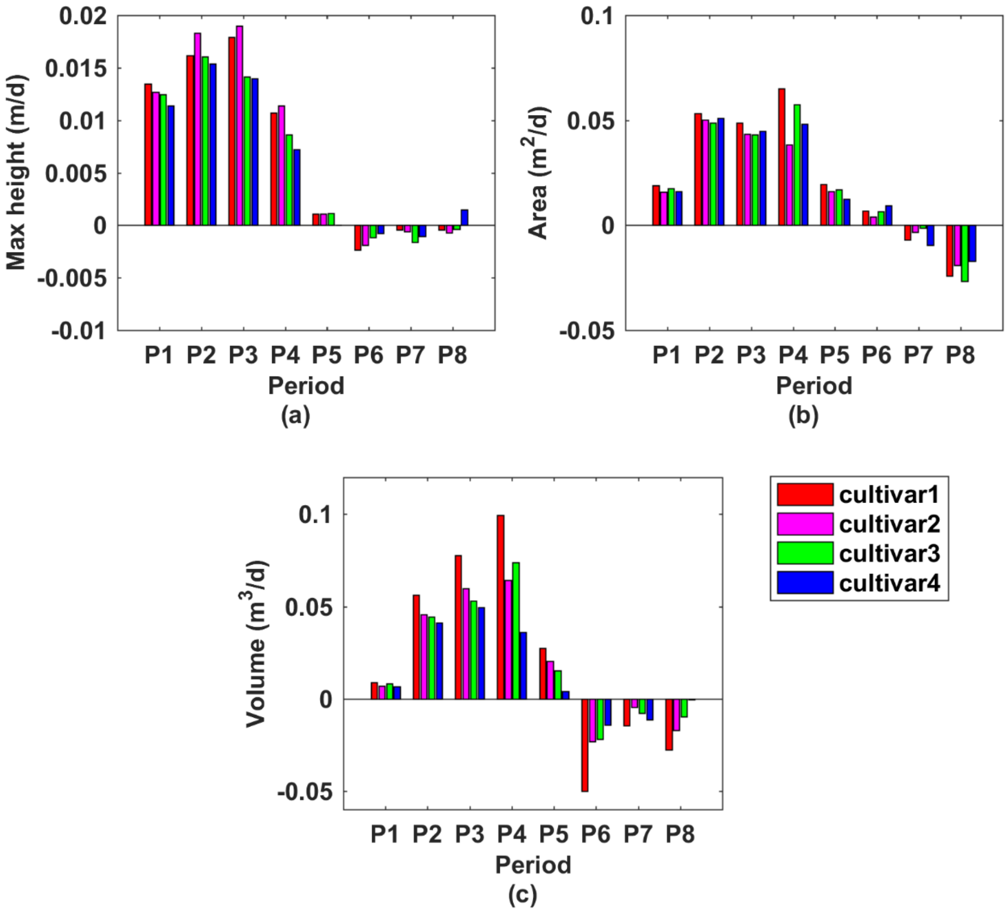

Figure 3.9. Growth rates for derived morphologic parameters at different time frames during the monitoring period. (a) Maximum canopy height; (b) projected canopy area; (c) plant volume.

ANOVA tests showed that cultivars had a significant influence on the derived morphologic traits over the monitoring period (Table 3.2). This allowed us to utilize regression analysis to determine which morphologic traits and measurement times were most closely associated with final yield for each cultivar.

Table 3.2. Effects of cultivars on derived parameters over the monitoring period (Year: 2016)

	July28 (DAP45)	**Aug 04 (DAP52)**	**Aug19 (DAP67)**	**Aug 26 (DAP74)**	**Sep 09 (DAP 88)**	**Sep 16 (DAP 95)**	**Sep 23 (DAP 102)**	**Sep 30 (DAP109)**
maxCH	< 0.001**	< 0.001**	< 0.001**	< 0.001**	< 0.001**	< 0.001**	< 0.001**	< 0.001**
PCA	0.003**	0.003**	0.034*	0.005**	0.001**	0.001**	0.002**	0.006**
PV	0.002**	0.001**	< 0.001**	< 0.001**	< 0.001**	< 0.001**	< 0.001**	< 0.001**

* significant at the 0.05 probability level, ** significant at the 0.01 probability level

3.3.3 Relationship between Morphologic Traits and Yield

A significant difference in the final yield was observed between the four cultivars (Table 3.3). Cultivar 2 produced significantly lower yields than cultivar 3 and 4.

Table 3.3. Differences in final yield between four cultivars (p-value < 0.05, different letters indicate significant differences between cultivars)

Cultivar	**Mean yield (g/plot)**
Cultivar1	928.51^{AB}
Cultivar2	781.58^{B}
Cultivar3	954.18^{A}
Cultivar4	937.22^{A}

The relationship between CH and final yield showed similar trends using data from various CH percentiles, especially between the 85th and 94th percentiles. The R^2 values for cultivar 1, 3, and 4 increased over the monitoring period although there existed only slight variation, whereas cultivar 2 exhibited a decreasing trend (Figure 3.10). Among the cultivars studied, cultivar 4 had the highest R^2 values (up to 0.84) from day 67 on, based on the 85th CH to maximum CH. The variation curve of cultivar 1 was analogous to the curve for cultivar 3, both reaching the highest R^2 values between 88 and 95 DAP. In contrast, cultivar 2 demonstrated the highest correlation with yield at an early growth stage around 52 DAP. Based on the results from this study, percentiles from 85% to 94% of CH during the period from 67 to 109 DAP are recommended for yield estimation application due to not only high but also stable R^2 values for all four cultivars.

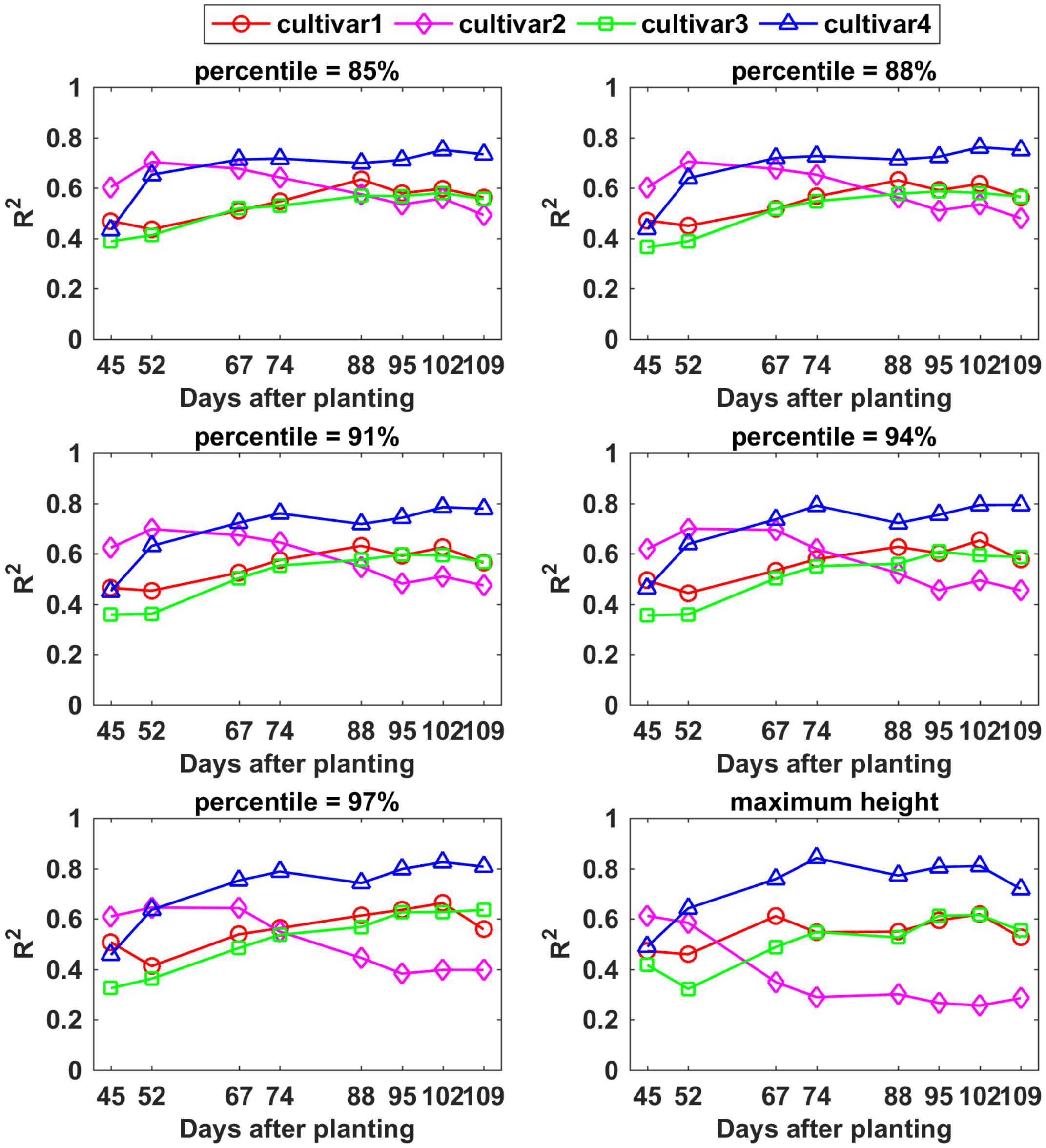

Figure 3.10. Correlation analysis results between different percentiles of canopy height and yield by days after planting for each cultivar.

Overall, the R^2 values between PCA and final yield increased over the monitoring period for all four cultivars (Figure 3.11a). The R^2 values for cultivars 2, 3, and 4 on each data collection day were similar, while cultivar 1 exhibited lower R^2 values. Compared to CH parameters, a major difference was that cultivar 2 had an opposite variation trend. The highest R^2 values for all four cultivars were reached between 88 and 109 DAP, and they were 0.65, 0.83, 0.87, and 0.88 for cultivars 1, 2, 3, and 4, respectively. This indicated that PCA was more closely related to final yield than CH. For both CH and PCA, cultivar 4 showed the strongest correlation with final yield among the four cultivars.

For PV, the difference in R^2 values between the four cultivars became smaller over the monitoring period compared to CH and PCA, especially between 88 and 102 DAP (Figure 3.11b). The maximum R^2 values were 0.77, 0.85, 0.84, and 0.83 on 95, 67, 74, and 74 DAP for cultivars 1, 2, 3, and 4, respectively, which were similar to the values for PCA, and better than CH. This indicated that PV was a more stable trait than CH and PCA and could feasibly be used to predict cotton final yield.

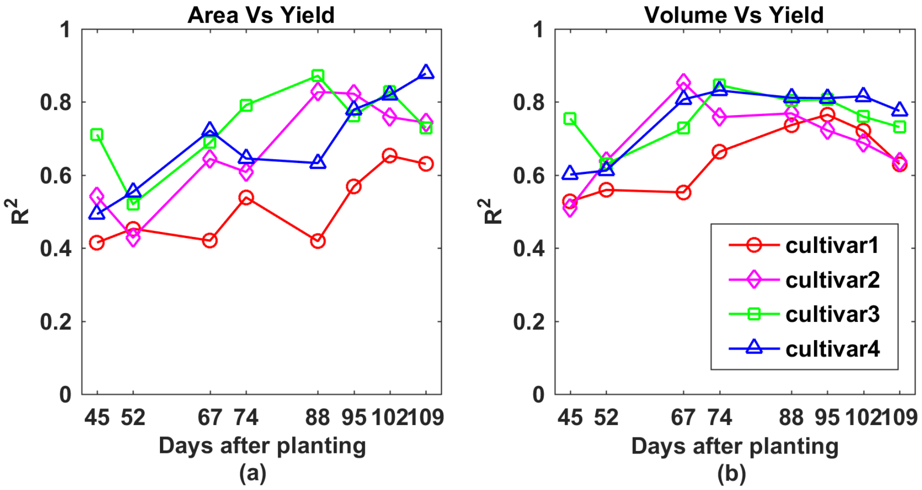

Figure 3.11. Correlation analysis results between (a) projected canopy area and yield, and (b) plant volume and yield by days after planting for each cultivar.

PCA and PV had higher R^2 values than CH over the monitoring period (Figure 3.12) when combining all cultivars. The R^2 values increased steadily to a final value of 0.72 for PCA. PV reached the highest R^2 value (0.56) on 67 DAP—although the PV R^2 values were less than those of PCA from 67 to 109 DAP, they were more stable than those of PCA. The lowest correlation was found between CH and final yield. A decreasing trend was observed from 45 to 109 DAP which was mainly due to cultivar 2.

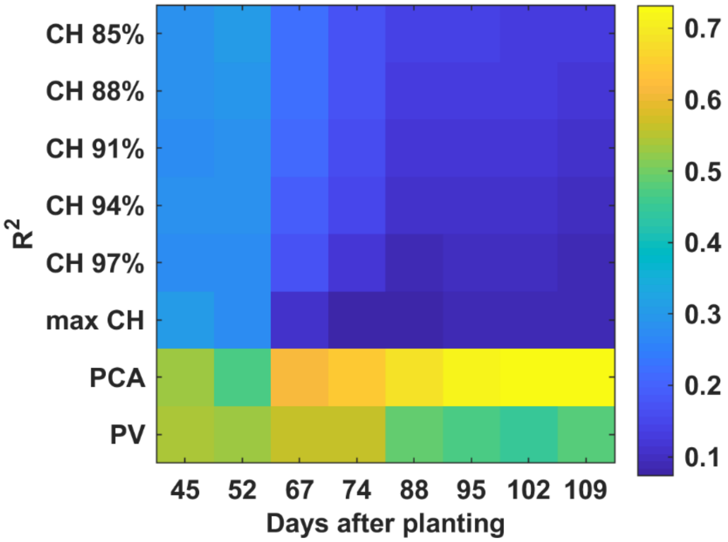

Figure 3.12. Correlation analysis results between derived parameters and yield with all cultivars combined by days after planting.

3.4 Discussion

We have demonstrated that 3D point clouds reconstructed based on data collected by a 2D LiDAR and an RTK-GPS, and associated data processing methodology, accurately estimated specific morphologic traits from cotton plants under field conditions. The precise 3D point cloud, which was the basic dataset for analysis, was critical for the successful extraction of plant morphologic traits (Duan et al., 2016; Paproki et al., 2012; Paulus et al., 2014b). The reconstructed

3D model visually represented plant canopy structures (Figure 3.5). The CH, PCA, and PV derived by our system were highly correlated (the slopes were close to one) with those measured manually (Figure 3.6).

The system demonstrated great potential for high-throughput phenotypic analysis. The number of points for each plot varied from 2,000 to 20,000 over the monitoring period, depending on the plant size. The tractor was driven in the field at a speed of around 0.5 m/s for data collection, taking about six seconds to scan one plot that contained 15 plants. Thus, one could anticipate scanning about 600 such plots per hour. The average time consumed for 3D reconstruction and parameter extraction was around 5.27 seconds per plot so about an hour for the aforementioned 600-plot field. Therefore, both data acquisition and data analysis speeds are suitable for application to field experiments of the sizes used in many breeding programs. The system also has great potential to implement online data analysis with faster computing power in the future, which is particularly useful for large field applications.

The high throughput phenotypic analysis by a LiDAR-based method has several advantages compared to image-based methods. Paproki et al. (2012) conducted cotton plant morphologic trait analysis using an image-based 3D reconstruction method, requiring about seven minutes to collect images for each plant and an average processing time of 15 minutes for 3D reconstruction work of each plant. Additionally, image quality could be significantly affected by highly variable illumination conditions (Nuske et al., 2014), which limited its in-field applications. In contrast, LiDAR is more versatile in a wide range of light conditions since it is equipped with its own light source. For manual operation, approximately 30 minutes were required for a typical analysis per plant depending on the size and complexity, and destructive harvests were often required (Paproki et al., 2012).

The high throughput of the proposed system and its non-invasive features permit data acquisition repeatedly over the growing season, opening the door to acquisition of plant growth rate variation, which is valuable for a wide range of applications such as building plant growth models (Tessmer et al., 2013; Weraduwagel et al., 2015), exploring factors influencing growth processes (Awlia et al., 2016; Rahaman et al., 2015), genomics-assisted crop breeding (Watanabe et al., 2017), and QTL analysis (Bac-Molenaar et al., 2015; Cui et al., 2017). In this study, all plants in the experimental field were scanned from 43 to 109 DAP. Plant growth curves were generated and correlation between derived parameters and the final yield were explored, which could be used for yield prediction (Sharma et al., 2015) and species identification (Remagnino et al., 2016). Thus, the system described herein not only provides an indication of which LiDAR-derived parameters are most closely associated with yield, but also allows us to define the period during the growing season in which a morphologic trait has the greatest correlation with final yield.

While CH in the current study was highly correlated with within-cultivar yield variation in some instances (i.e. cultivar 4 on later sample dates), it should be noted that correlations between CH and yield for all cultivars combined were substantially lower than those obtained for other derived parameters such as PCA and PV. This is not surprising since the cotton crop exhibits a quadratic response of yield to CH (Sui et al., 2012), where internode elongation must often be controlled using exogenously applied plant growth regulators (PGRs) in real-world production scenarios (Dodds et al., 2010). While CH may not be inherently predictive of genotypic differences in yield, the deployment of high-throughput methods for estimating maximum CH and rate of change in

CH could strongly influence cultivar-specific PGR management strategies. Specifically, cultivars with rapid plant height development typically require more aggressive management strategies (Collins, 2013).

PCA and PV were more strongly associated with yield than CH when considered across all cultivars, suggesting these parameters might have greater utility as high-throughput phenotyping tools to identify potential differences in productivity. The impact of canopy development on yield is easily understood when yield is expressed as the product of total intercepted photosynthetically active radiation, radiation use efficiency, and harvest index (Earl and Davis, 2003; Monteith, 1994; Monteith and Moss, 1977; Stöckle and Kemanian, 2009). Within this conceptual framework, the amount of intercepted photosynthetically active radiation during a growing season will be strongly impacted by the length of the growing season and the leaf area available to intercept solar radiation. Thus, PCA may serve as a suitable proxy for leaf area magnitude and persistence throughout the growing season. PV incorporates both CH and PCA, which could potentially be related to both the amount of leaf area available to intercept incoming solar radiation and the three dimensional space available for developing fruit. Both of these considerations are important given the indeterminate nature of cotton. As fruit development progresses, vegetative growth slows, and Constable and Bange (2015) have clearly illustrated that the ability of the cotton crop to attain high yield potential will be influenced by total leaf area and number of fruiting sites available prior to the development of a large fruiting load on the plant. Thus, it is not surprising that PCA and PV were correlated with yield for much of the growing season. Future work should couple the aforementioned measures with high-throughput assessment of fruit development as fruiting dynamics can drastically impact final yield in cotton (Constable and Bange, 2015).

The top view scan setting of LiDAR provided precise 3D surface models of plants; however, organs under the canopy could not be reached due to plant occlusion. This does not reduce the accuracy of CH and PCA measurements, but hinders the estimation of PV by our system, especially when plant structure becomes complex. Multi-view scan is a commonly used method to reduce plant occlusion effects (Paulus et al., 2014b), and in our future studies two side view scans could be added. In addition, algorithms such as plant shape models (Pastrana and Rath, 2013) have been proposed to overcome plant occlusion effects. However, when plant structure complexity increases, especially at the mature stage with a greatly increased number and size of leaves and stems, occlusion effects would still be present. Plant occlusion remains a challenge for plant phenotyping, especially under field conditions with limited inter-row spacing (Paproki et al., 2012; Paulus et al., 2014a). Wind is another factor which could affect the accuracy of the derived traits since it might result in blurred point clouds. Therefore, calm weather conditions are best for data collection. Based on the CH validation results, our system has a certain robustness against wind influence; wind speed under 3 m/s was feasible. Another limitation was that the tractor speed was restricted by the scanning frequency of the LiDAR (Sun et al., 2017), limiting throughput. While the present system is already compatible with iterative study of thousands of plots, 3D LiDAR technology may greatly reduce this limitation (Weiss and Biber, 2011).

3.5 Conclusion

Precise 3D surface models were reconstructed by the high-throughput phenotyping system developed in this study under field conditions. Multiple morphologic traits at the plot level including plant height, projected canopy area, and plant volume were extracted simultaneously. The system could be used to scan the field repeatedly due to its relatively high data collection and processing capability, which was particularly useful for large field applications. The measured morphologic traits were most highly correlated with final yield during the period between around 67 and 109 DAP. Projected canopy area and plant volume were more closely correlated than plant height to final yield. Future work will focus on involving other sensor data to extract more phenotypic traits from the 3D point cloud. Although this system was solely tested on cotton plants, it is expected to be applicable for use with other crops such as wheat, rice, and soybeans.

CHAPTER 4

IMAGE PROCESSING ALGORITHMS FOR INFIELD SINGLE COTTON BOLL COUTNING AND YIELD PREDICTION[3]

---

[3] Sun, S.; Li, C.; Paterson, A.H.; Chee, P.W.; Robertson, J.S. *Computers and Electronics in Agriculture* 2019, 166, 1-15. Reprinted here with permission of publisher.

Abstract

Cotton boll number is an important component of fiber yield, arguably the most important phenotypic trait to plant breeders and growers alike. In addition, boll number provides a better understanding on the physiological and genetic mechanisms of crop growth and development, facilitating timely decisions on crop management to maximize profit. Traditional in-field cotton boll number counting by visual inspection is time consuming and labor-intensive. In this work, we presented novel image processing algorithms for automatic single cotton boll recognition and counting under natural illumination in the field. A digital camera mounted on a robot platform was used to acquire images with a 45° downward angle on three different days before harvest. A double-thresholding with region growth algorithm combining color and spatial features was applied to segment bolls from background, and three geometric-feature-based algorithms were developed to estimate boll number. Line features detected by linear Hough Transform and the minimum boundary distance between two regions were used to merge disjointed regions split by branches and burrs, respectively. The area and the elongation ratio between major and minor axes were used to separate bolls overlapping in clusters. A total of 210 images captured under sunny and cloudy illumination conditions on three days were used to validate the performance of the cotton boll recognition method, with an F1 score of around 0.98; whereas, the best accuracy for boll counting was around 84.6%. At the whole plot level, fifteen plots were used to build a linear regression model between the estimated boll number and the overall fiber yield with a R^2 value of 0.53. The performance was evaluated by another ten plots with a mean absolute percentage error of 8.92% and a root mean square error of 99 g. The methodology developed in this study provides

a means to estimate cotton boll number from color images under field conditions and would be helpful to predict crop yield and understand genetic mechanisms of crop growth.

4.1 Introduction

Cotton (*Gossypium spp.*) is among the most economically important fiber crops, accounting for almost 80% of total natural fiber production throughout the world with China, India, United States and Pakistan (Fangueiro and Rana, 2016). In 2017, an estimated 12 million acres of cotton were grown in the US, contributing $7 billion for the US economy (USDA, 2018a). Cotton boll number is an important indicator of fiber yield, arguably the most important phenotypic trait to plant breeders and growers alike. In addition to providing a better understanding on the physiological and genetic mechanisms of crop growth and development, boll number as an important yield indicator also provides a means to predict yield potential and assess crop growth conditions, facilitating timely decisions on crop management, thereby maximizing profit by preventing yield losses due to insects and diseases and reducing costs. Traditional yield prediction based on manual sampling (Huang et al., 2016) or visual inspection and prior experience (Feng et al., 2018) is prone to errors, and is not practical for evaluating thousands of plots in plant breeding programs. Computer vision based systems coupled with agriculture robots (Oberti and Shapiro, 2016) or unmanned aerial vehicles (UAV) (Zaman-Allah et al., 2015) could potentially automate boll counting and yield prediction, increasing efficiency and reducing human-error (Qureshi et al., 2017; Rahnemoonfar and Sheppard, 2017).

During the past decade, several studies have been conducted to explore the use of computer vision technologies for cotton boll detection. For example, cotton bolls can be separated from background using the saturation channel (S channel) from a hue-saturation-value (HSV) color space (Wei et al., 2008). Similarly, the YCbCr color space was used to segment cotton bolls from the branch and soil with an accuracy of 90.44% based on a dataset with 136 images (Liu et al., 2011). Further, the OHTA color space with a support vector machine (SVM) classifier could segment cotton bolls with an accuracy of 92.3% (Chen et al., 2013). More recently, a region-based semantic segmentation algorithm was proposed to detect bolls in images acquired in the field (Li et al., 2016). To segment cotton bolls from complex background such foliage, branches, sky and plastic, a 110-dimensional feature vector including color and texture features, was built to train a random forest (RF) classifier for boll segmentation, achieving an average accuracy of 99.4%. Although these studies provided potential solutions for cotton boll segmentation in various scenarios, none of them investigated separating each individual boll from all others and counting boll numbers, which is a substantially more challenging task than segmentation.

In addition to cotton bolls detection, researchers have developed computer vision techniques for other fruit crops detection using 2D color images and some of them explored fruit counting. For example, several machine learning based classifiers were trained using color, shape and texture features to segment immature peach fruit from images collected in orchards (Kurtulmus et al., 2013). Discriminant analysis and neural network classifiers exhibited the best detection performance with an accuracy of 85% for fruit detection. An X-means clustering algorithm with color and shape features to detect and count tomatoes achieved a recall of 0.80 and precision of 0.88 (Yamamoto et al., 2014). A stereo vision system was employed using random ring method (RRM) with color and shape features to detect apples and map their spatial positions with errors less than 20 mm when the camera working distance was between 400 mm and 1500 mm (Si et al., 2015). In another study (Bargoti and Underwood, 2017), a digital camera mounted on a robot-based platform was applied for fruit detection and counting in apple orchards. Two artificial intelligence methods—multi-scale multi-layered perceptron (ms-MLP) and convolutional neural network (CNN)—were used for apple segmentation, applying watershed segmentation (WS) and circle hough transform (CHT) methods for apple counting. Apple segmentation using CNN achieved better performance with the best pixel-wise F1-score of 0.791, and WS yielded a more accurate apple counting results with an F1-score of 0.858. To locate litchi positions, a binocular stereo vision system and a K-means based clustering algorithm was used to segment fruit from background and a label template matching method was applied to detect individual litchis (Wang et al., 2016a). The average litchi recognition rates were 98.8% and 97.5% for non-occluded and partially occluded situations, respectively, and 98% and 94% individual litchis were successfully matched for a total of 100 pairs of tested images. An adaptive boosting (AdaBoost) framework was applied based on color features (Luo et al., 2016) to separate individual grape clusters from two adjoining grape clusters, with a classification accuracy of 93.7%. However, the authors did not explain how to judge whether a detected region was a single grape cluster or two adjoining clusters, nor could the method deal with three or more adjoining and overlapping clusters. Color features in hue and red channels containing with shape features were applied to detect individual kiwifruits with a counting accuracy of 92.0% in night-time with flash (Fu et al., 2019). All these studies except (Fu et al., 2019; Yamamoto et al., 2014) were conducted in the field during daytime, and the common problem of fruit occlusion was one of the main factors in the reduced success rate of the classifiers.

While significant progress has been made in detecting individual fruits in some fruit crops, applying this technology broadly in agricultural applications is challenging due to complex background, non-uniform lighting conditions, and different fruit characteristics of various crops. Usually there are two main steps in fruit detection and counting: image segmentation and individual object detection. Image segmentation aims to separate a region of interest (ROI) (e.g., cotton boll) from the background (e.g., ground, branches, or foliage). The segmentation operation is usually conducted by transforming image regions into discriminative feature spaces and then associating them to either ROI or background. Color, texture, shape and size are commonly used features. Individual object detection aims to find individual objects from the segmented regions of the first step, which is usually implemented by merging or splitting ROI. In agriculture applications, objects are often clustered together, and individual objects are often split into disjointed regions by branches, foliage or other obstacles. Therefore, object detection algorithms should have the ability to separate individual objects in clusters, and to connect disjointed regions together as a single object.

The main contribution of this work was to develop 2D image processing algorithms for single cotton boll counting and to explore the relationship between boll number and yield. While several past studies have documented good performance for individual fruit detection, the CHT and blob-based methods used in these studies are not transferable to this study due to specific attributes of cotton bolls as well as the unique architecture of the cotton plants. Cotton bolls can have varied and complex shapes, especially as they open and fiber hangs out towards the late season. This is significantly different from fruits with rigid shapes such as apples, litchis and mangoes. Moreover, cotton plants have relatively complex physical structure among major field crops (Mauney, 1986), substantially increasing the challenge of individual boll counting. Therefore, new features and encoding methods are needed for boll counting. Specific objectives of this study were to (1) propose an image segmentation algorithm to distinguish bolls from a complex background with a combination of color and spatial information, (2) develop and validate a boll counting method based on geometric features of bolls, and (3) evaluate boll counting as a predictor of fiber yield at the plot level.

4.2 Materials and Methods

4.2.1 Experiment setup

The experiment was conducted at the University of Georgia Iron Horse Farm located in Greene County, GA, USA (Figure 4.1). The field experiment included 128 plots arranged in 16 rows and 8 columns, using a randomized complete block design with four cultivars of cotton and 32 replicate plots per cultivar. Each plot was about 3.05 m long with 15 seeds sowed at consistent spacing of 0.15 m per plant. Inter-row or plot spacing was 1.52 m and inter-column or range spacing was 1.83 m. Cotton seeds were sowed on June 13 and fiber was manually harvested on Nov 04, 2016. Four cotton cultivars were planted including GA2011158, GA2009037, GA2010074, and UA48.

Figure 4.1. Experimental field layout information and single plot details.

4.2.2 Experiment setup

A digital color camera (Lumix G6, Panasonic, Osaka, Japan) mounted on a robot (MMP-30, The machine Lab, Fort Collins, Colorado, USA) at a height of 1.3 m was used to photograph bolls with a downward angel of 45° (Figure 4.2(a)). The camera was configured to be in a shutter priority mode with shutter speed of 1/500 s, ISO of 150, and a focal length of 14 mm. The robot was remote controlled by an operator at speeds of 0.3 ~ 0.5 m/s in the middle of two rows with a camera working distance around 70 ~ 200 cm. Images were collected during 9:00 to 11:00 in the morning on three days, specifically Oct 07, Oct 19, and Nov 03, 2016, respectively, corresponding to 116, 128 and 143 days after planting (DAP). The first two days were cloudy, and the third day was sunny. All images were stored in JPG format, with a resolution of 3456 ×4608 pixels and a size of ~ 8 MB. Typical images for each day were shown in Figure 4.2(b), (c) and (d). On 116 DAP, cotton bolls were tight and there were still unopened bolls and some green leaves on the plants. By 128 DAP, almost all cotton bolls were opened with very few leaves left on plants, and bolls still held relatively round shapes. On 143 DAP, some bolls were open drooped due to the individual fiber bearing seeds were stringing out, resulting in complex shapes and varied sizes.

Figure 4.2. Imaging platform and representative images. (a) The MMP-30 based platform for imaging in the field. Typical images captured on (b) Oct 07, that was116 DAP; (c) Oct 19, 128 DAP; and (d) Nov 03, 143 DAP, in 2016. DAP was short for days after planting. Images were captured with the camera horizontally on the first and third days, and with the camera vertically on the second day.

4.2.3. Image processing

4.2.3.1. Method overview

After images were collected in the field, they were subjected to the image processing pipeline which was mainly composed of two operations: boll recognition and boll counting. In order to improve image processing efficiency, all input raw images were resized by a scale of 0.2 (Figure 4.3(a)). For boll recognition, the aim was to segment bolls from the background including branches, leaves and ground. The output was a binary image in which the foreground was classified as cotton bolls marked as white (pixel intensity of one) and the background marked as black (pixel intensity of zero) (Figure 4.3(b)). Boll recognition was implemented based on color and spatial features. For boll counting, the goal was to detect individual bolls and estimate the total number for each input image, which was implemented based on geometric features including line feature, position feature, shape and size features in each segmented binary image (Figure 4.3(c)). Red lines in Figure 4.3(c-1) were detected line features for contours of cotton boll regions; Figure 4.3(c-2) showed position features for three boll regions. The position feature was described as the minimum distance between two cotton boll regions. The area of a region (the number of pixels within the area) was used as the size feature descriptor, and the elongation ratio (ratio between major axis and minor axis) was used as the shape feature descriptor (Figure 4.3(c-3)). The final output was an image with a total number of detected bolls that were labeled by ellipses and centroid points (Figure 4.3(d)).

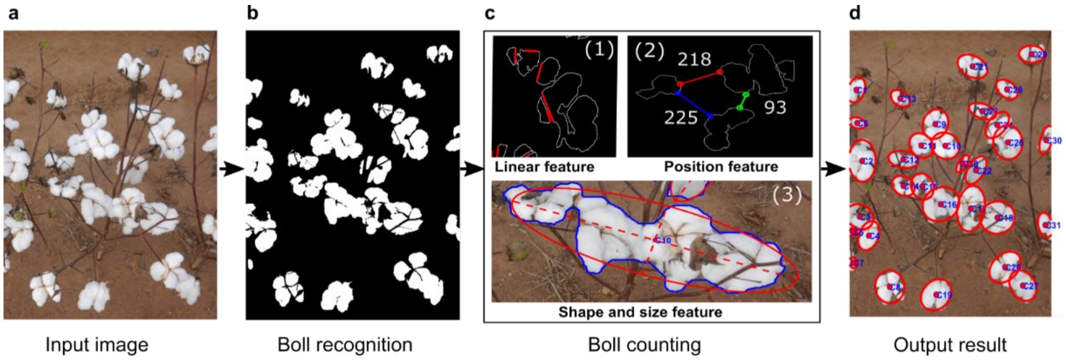

Figure 4.3. Image processing pipeline. (a) Raw image captured in the field were used as input. (b) Boll recognition was implemented based on color and spatial features. Boll pixels were indicated with white color and background black color. (c) Boll counting was implemented by merging and splitting segmented boll regions based on geometric features including line feature, position feature, shape and size features. (d) Boll counting result, with each inferred boll indicated using an ellipse with its centroid point.

The image processing and statistical analysis program was developed in MATLAB 2017b (The Math Works Inc., Natick, MA, USA) on a desktop equipped with an Intel I7-6700 3.40 GHz CPU and a 16 GB RAM, running on a Windows 10 Enterprise operating system.

4.2.3.2. Boll recognition

A double-thresholding with region growth algorithm was applied for boll recognition, which incorporated both color and spatial features (Szeliski, 2010). Images collected in this study had much simpler background due to a smaller field of view and much less foliage than those shown in a prior study (Li et al., 2016). There existed a clear and significant difference between boll and background in their color features. In order to quantitatively demonstrate the color feature difference, the pixel intensity histograms in RGB and HSV color spaces were presented based on sample pixels extracted under sunny and cloudy illumination conditions (Figure 4.4). Large overlaps between bolls and background were observed in channels R, G, and B (Figure 4.4(a), (b), and (c)), while bolls and background were well separated in channel S with a distinct bi-modal distribution (Figure 4.4(d)). In Figure 4.4(d), boll pixel intensity in saturation mainly ranged from 0 to 50, while background pixel was usually greater than 50. In order to compare with results in R, G and B channels, pixel intensity in channel S was linearly mapped from [0, 1] to the range [0, 255]. Histograms of channel H and V were not presented since color features in these two channels were not significantly different.

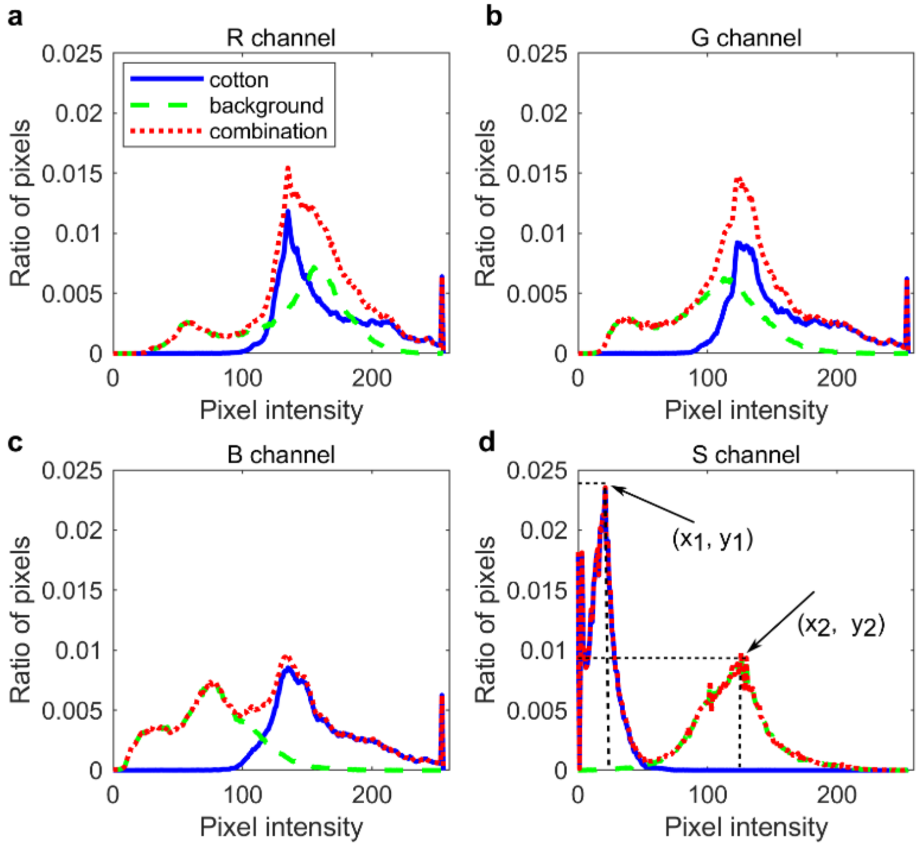

Figure 4.4 Comparison of cotton bolls and background in (a) Red channel, (b) Green channel; and (c) Blue channel in RGB color space and (d) Saturation channel in HSV color space.

Therefore, color features extracted in S channel were used for boll recognition. In addition, spatial features were incorporated in order to make boll recognition more robust to varied illumination conditions. The boll recognition method was described as follows:

Step 1: convert the raw image from the RGB to HSV color space, and compute the histogram for S channel. The red dashed line shown in Figure 4.4(d) was an example of the histogram.

Step 2: detect peaks in the range of [0, 50] and [50, 150], respectively. Label the peak as (x_1, y_1) which was closer to the intensity value of 50 between the two peaks in the range of [0, 50], and label the peak as (x_2, y_2) located in [50, 150] based on the same rule. The reason for two peaks in the range of [0, 50] was that some bolls were under shadow and some were under sunlight. The image was partitioned into three regions by eq (4.1).

$$\begin{cases} R_1 : \text{pixel intensity} \le x_1 \\ R_2 : \text{pixel intensity} \ge x_2 \\ R_3 : x_1 < \text{pixel intensity} < x_2 \end{cases} \tag{4.1}$$

where, R_1 was pure foreground (bolls), R_2 was pure background, R_3 was mixed population.

Step 3: for any pixel in R_3, if it had 4-neighbors in R_1, then reassign this pixel to R_1. Repeat this operation until no more pixels in R_3 can be reassigned to R_1. At last, reassign the remaining pixels in R_3 to R_2.

Step 4: binarize the image. Pixels in R_1 were set to be 1, others to be 0. A size filter was applied to remove the noise.

4.2.3.3. Boll counting

Boll counting methods including merging and splitting operations developed in this study relied on cotton boll morphological characteristics. Regular cotton bolls have sphere shapes (Figure 4.5(a)) which could be detected using methods such as CHT and blob detection similar to prior studies for apple (Bargoti and Underwood, 2017) and litchis (Wang et al., 2016a) detection ; however, some cotton bolls have complex shapes and varied sizes (Figure 4.5(b)), which are different from fruits with rigid shapes. A single boll could be split into two or more disjointed regions by branches laying in front of the boll (Figure 4.5(c)). In addition, a cotton boll was a dry dehiscent capsule composed of four or rarely five locules that hold together by a bur (Figure 4.5(d)), and burrs could split a boll into several regions. Therefore, the method should detect these regions and merge them together. Branches at the boll size level could be assumed to be a straight line which can be detected using Line Hough Transform (LHT), and burrs were very thin, resulting in split regions that were very close to each other. These two features were used for the merging operation in this study. Another problem for boll counting was that bolls were clustered together and often overlapped with each other in images (Figure 4.5(e)). Clusters usually have a larger elongation ratio and area than single bolls. A splitting algorithm that can separate a cluster into individual bolls was developed based on the cluster size (region area) and shape (elongation ratio) features.

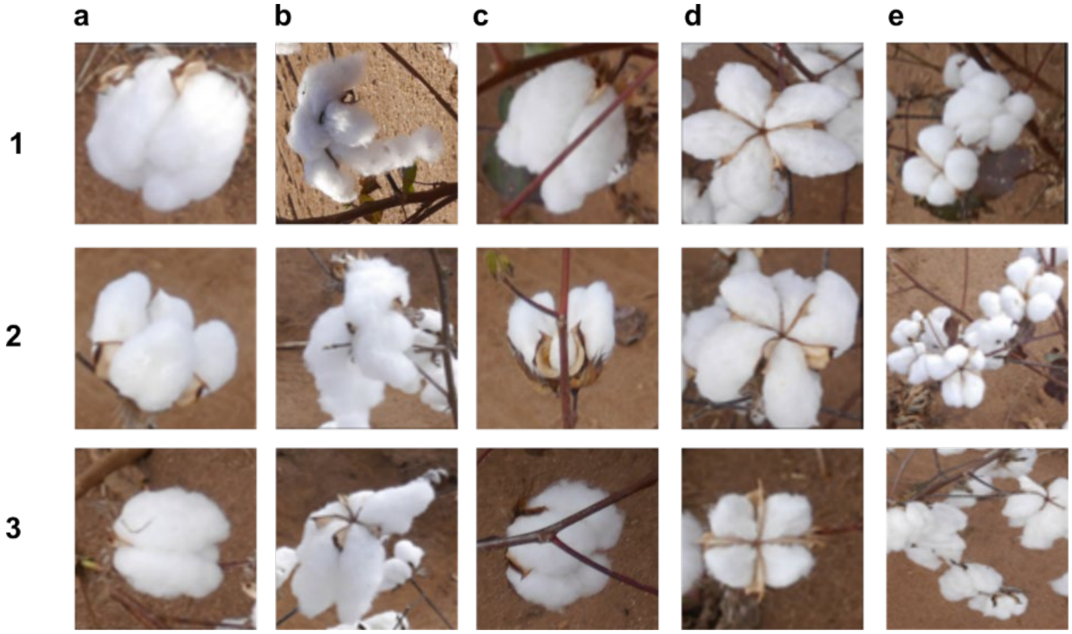

Figure 4.5. Typical challenges for cotton boll counting. (a) Regular cotton bolls with good shapes and similar sizes; (b) Cotton bolls with variable shapes and sizes; (c) Single bolls split by branches; (d) Single bolls with four locules; (e) Bolls connected in clusters.

Disjointed regions of a boll split by branches could be merged together based on line features with the assumption that a branch at the boll size level is a straight line. Denote B as the output binary image from image recognition operation, and from which disjointed regions R were obtained using connected component labeling (CCL) algorithm, the contour set of all regions in R

was depicted as C. For each contour in C, LHT was applied to detect whether there exist lines, resulting in a set L for R. L_i was a vector used to store detected lines in contour C_i; if no line was detected, $L_i = \emptyset$. $C_i \in C$, $L_i \in L$. Therefore, L could be divided into two subsets, $L1$ and $L2$. $L1$ was a subset of L without detected lines, and $L2$ was a subset of L with detected lines, $L1 \cup L2 = L$, $L1 \cap L2 = \emptyset$. Accordingly, C was divided into two subsets, $C1$ and $C2$. If lines detected in two contours in $C2$ were parallel and close enough, the two corresponding regions would be grouped together as one sharing the same label. The LHT-based merging was described in Algorithm 1.

In Algorithm 1, two regions would be merged if two corresponding lines were parallel and close enough (Figure 4.6(a)). Two lines were parallel if the lines were with the same slope. A slope could be expressed by an angle between the line and the horizontal axis. In this study, the angle difference between the two lines were used to check the parallel condition. In order to tolerate noise, the parameter of angle difference τ_1 was set to be 3°. The distance between middle points of the two lines, indicated by pixels, was used to check whether the two lines were close enough. This parameter τ_2 was estimated by the configuration of the camera (eq (4.2)) and branch size.

$$V = \frac{s \times d}{f} \tag{4.2}$$

where V was image field dimension, s was sensor size, d was camera working distance (distance from then lens to object), and f was the focal length. In this study, the camera sensor size was 17.3 × 13 mm, the camera working distance ranged from 70 cm to 200 cm—the distance 70 cm was selected to estimate the parameters. At the selected working distance, the field dimension of images was around 865 mm × 650 mm, resulting in spatial resolution of ~0.94 mm/pixel based on the resized images. The diameter of a branch was usually less than 10 mm, that was ~11 pixels, τ_2

= 11. Therefore, if the angle difference was less than 3° and the middle points distance was less than 11 pixels, the corresponding two regions would be merged as one.

Algorithm 1: Merge cotton bolls split by branches

```
Input: $B$    # binary image output from boll recognition operation
$R = CCL(B)$         # connected component labeling function
$C = contour(R)$     # contour function
$L = LHT(C)$         # linear Hough transform function
$L \rightarrow L1, L2$         # divide $L$ into $L1$ (subset without lines) and $L2$ (subset with lines)
$C \rightarrow C1, C2$       # divide $C$ into $C1$ and $C2$ according to the division of $L$
$C1 = \{C1_1, \cdots, C1_n\}$, $C2 = \{C2_1, \cdots, C2_m\}$, $L2 = \{L2_1, \cdots, L2_m\}$
# find regions which should be merged in $C2$
$flag = \{[1], \cdots, [m]\}$ # initialize a table flag used to label regions in $C2$ which should be merged, $flag(i) = [i]$
for $i = 1$ to $(m - 1)$ do
    for $j = (i + 1)$ to $m$ do
        if $l_i$, $l_j$ are parallel and close enough # $l_i$, $l_j$ are lines in $L2_i$, $L2_j$   then
            $flag(i) \leftarrow [flag(i), j]$      # add the index of $C2_j$ into $flag(i)$
        end
    end
end
# conduct merging operation
$i = 1$     # label for regions after merging operation
while $flag \neq \emptyset$ do
    $M(i) \leftarrow flag(1)$     # $M$ is a set for merged regions
    $tmp = [1]$        # index of regions should be merged, update in the following loop
    for $j = 2$ to $size(flag)$ do
        if $M(i) \cap flag(j) \neq \emptyset$ then
            $M(i) \leftarrow [M(i), flag(j)]$
            $tmp \leftarrow [tmp, j]$
        end
    end
    $flag \leftarrow flag \setminus tmp$     # remove the rows with the index in $tmp$ from $flag$
    $i \leftarrow i + 1$
end
$C_B = [M, C_1]$;   # $C_B$: new region set, $C_B = \{C_{B1}, C_{B2}, \cdots, C_{Bk}\}$
Return $C_B$
```

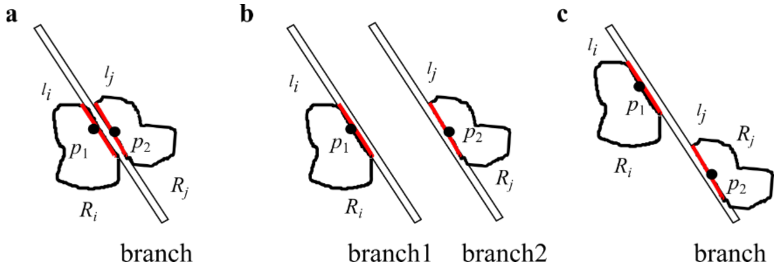

Figure 4.6. Schemes for merging two regions split by branches. (a) Two regions split by the same part of a branch; the two lines were parallel and close enough and should be merged as one. (b) Two regions split by two branches; (c) Two regions split by two different parts of the same branch. For the last two situations, although the two lines were parallel, they were far away, therefore, they should be two individual regions. R_i, R_j were two regions with detected lines l_i, l_j indicated using red color, p_1 and p_2 were the middle points of l_i, l_j, respectively.

The cotton burrs were not straight even at boll size level, and were usually much thinner than branches (Figure 4.5(d)), which indicated that the split regions should be very close (almost connected) to each other. Therefore, regions split by burrs can be merged based on the position features. In this study, the minimum boundary Euclidean distance between two regions was used as the position feature descriptor (eq. (4.3)). Let C_{Bm}, C_{Bn} denote the two contours with a pixel number of N_1 and N_2, respectively. Pixel (x_{mi}, y_{mi}) was the element in C_{Bm}, and (x_{nj}, y_{nj}) was the element in C_{Bn}.

$$\begin{aligned} d &= \Omega\left(C_{Bm}, C_{Bn}\right) \\ &= \min\left\{\sqrt{\left(x_{mi}-x_{nj}\right)^2+\left(y_{mi}-y_{nj}\right)^2}\right\} \\ i &= 1,2,\cdots,N_1, j=1,2,\cdots,N_2 \end{aligned} \tag{4.3}$$

Position feature based merging was described in Algorithm 2. A parameter τ_3 was used to evaluate whether two regions should be merged. Similar to Algorithm 1, it could be derived by the configuration of the camera and thickness of burrs. The thickness of burrs was usually less than 3 mm, so τ_3 was set to be 4 in this study.

Algorithm 2: Merge cotton bolls split by burrs

```
Input: $C_B = \{C_{B1}, C_{B2}, \cdots, C_{Bk}\}$ # $C_B$: output from Algorithm 1, contour for each labeled region
flag = {[1], ···, [k]}
for $i = 1$ to $k$ do
    for $j = i + 1$ to $k - 1$ do
        $d \leftarrow \Omega\,(C_{Bi}, C_{Bj})$
        if $d < \tau_3$   # parameter used to check whether two regions are close enough then
            $flag\,(i) \leftarrow [flag\,(i), j]$;
        end
    end
end
# the following merging operation is similar as in Algorithm 1
$i = 1$
while $flag \neq \emptyset$ do
    $C_L(i) \leftarrow flag\,(1)$      # $C_L$ is a set for merged regions
    $tmp = [1]$          # index of regions should be merged, update in the following loop
    for $j = 2$ to $size(flag)$ do
        if $C_L(i) \cap flag\,(j) \neq \emptyset$ then
            $C_L(i) \leftarrow [C_L(i), flag(j)]$
            $tmp \leftarrow [tmp, j]$
        end
    end
    $flag \leftarrow flag \setminus tmp$ # remove the rows with the index in tmp from flag
    $i \leftarrow i + 1$
end
Return $C_L$
```

Clusters composed of several connected bolls usually had a higher elongation ratio and larger area than individual bolls. Usually, a single boll had the elongation ratio around 1 to 1.5 based on observations in this study. A common situation under field conditions was that two bolls were connected as a cluster with an elongated shape and a larger elongation ratio than that of single bolls Figure 4.5(e-1). Sometimes, the cluster included more bolls (Figure 4.5(e-2)). Another situation was that the cluster had a round shape as shown in Figure 4.5(e-3), and the elongation ratio might be similar to single bolls. Therefore, the elongation ratio and region area were used to determine whether a region is a cluster. In this study, a region was considered to be a cluster if the region area a_i was larger than τ_4 (the size parameter) times the average region area A_m, $a_i > \tau_4 \cdot A_m$; or the area was between $[1, \tau_4]$ times the average area and the elongation ratio was greater than τ_5 (shape parameter). The splitting operation was described in Algorithm 3, and the size parameter τ_4

= 3 and the shape parameter τ_5 = 1.8 were selected based on the experiments conducted in this study.

Algorithm 3: Split cotton bolls connected in clusters

```
Input: $C_L = \{C_{L1}, C_{L2}, \cdots, C_{Ln}\}$    # $C_L$: output contour set from Algorithm 2
$R = \{r_1, r_2, \cdots, r_N\}$      # corresponding regions in $C_L$
$L = \{l_1, l_2, \cdots, l_N\}$       # major length of each region
$S = \{s_1, s_2, \cdots, s_N\}$      # minor length of each region
$P = \{p_1, p_2, \cdots, p_N\}$    # centroid of each region
$\Theta = \{\theta_1, \theta_2, \cdots, \theta_N\}$   # orientation of each region
$A = \{a_1, a_2, \cdots, a_N\}$   # area of each region
$E_i = L_i / s_i$      # elongation ratio for each region
$A_m = \frac{\sum a_i}{N}$      # average area for all regions
$Nc = size(R)$   # the number of regions in $R$
condition ← True
while condition do
    for $i = 1$ to $N_c$ do
        if $a_i > \tau_4 * A_m$ # splitting according to area feature; $\tau_4$: size parameter then
            $ri \rightarrow r_{i1}, r_{i2}$  # split $r_i$ into two sub-regions $r_{i1}$, $r_{i2}$ along minor axis
        end
        if $Am \le a_i \le \tau_4 * A_m$ and $E_i > \tau_5$  # splitting according to area and shape features; $\tau5$: shaper parameter then
            $r_i \rightarrow r_{i1}, r_{i2}$
        end
    $R = \{r_1, r_2, \cdots, r_{i1}, r_{i2}, \cdots, r_N\}$  # update $R$
    end
    update $L, S, P, \Theta, A, E_i, Am$
    $N_s = size(R)$  # the number of regions in $R$ after splitting
    condition ← $N_c \ne N_s$
    $N_c \leftarrow N_s$
end
Return $R$
```

4.2.4 Statistical analysis

In order to qualitatively evaluate boll recognition and counting performance, a total of 210 images were randomly selected from three days—116 DAP, 128 DAP and 143 DAP, each containing 70 images. Three metrics were computed to evaluate boll recognition performance.

$$\text{Pr} = \frac{TP}{TP+FP} \tag{4.4}$$

$$\mathrm{Re} = \frac{TP}{TP + FN} \tag{4.5}$$

$$F1 = 2 \times \frac{\mathrm{Pr} \times \mathrm{Re}}{\mathrm{Pr} + \mathrm{Re}} \tag{4.6}$$

where *Pr*, *Re* and F1 stand for precision, recall and F1-score, respectively. TP, FN, and FP were true positive, false negative, and false positive, respectively. If part of a boll was segmented, the boll was considered to be successfully recognized.

Another four metrics were proposed to evaluate the performance of boll counting.

$$MAPE = \frac{1}{n}\sum_{i=1}^{n}\left|\frac{N_d - N_g}{N_g}\right| \tag{4.7}$$

$$RMSE = \sqrt{\frac{1}{n}\sum_{i=1}^{n}\left(N_d - N_g\right)^2} \tag{4.8}$$

$$OSR = \frac{N_s}{N_g} \tag{4.9}$$

$$OMR = \frac{N_m}{N_g} \tag{4.10}$$

where, N_d, N_g, N_s, and N_m were the total number of detected bolls using the proposed algorithms, ground truth, number of over-splitting bolls, and number of over-merging bolls, respectively. *MAPE*, *RMSE*, *OSR* and *OMR* were short for mean absolute percentage error, root mean square error, over splitting rate and over merging rate, respectively. For a cluster including *m* individual bolls, if (*m*+*n*) bolls are detected by the algorithm, the over splitting number is n; similarly, if (*m*-

n) are detected, the over merging number is *n*. *n* is a positive integer. Moreover, simple linear regression analyses were conducted between the sensor detected boll number and manually counted boll number from the image. The coefficient of determination R^2 was calculated to assess the effectiveness of using one variable to predict the other.

4.2.5 Yield prediction

In order to analyze the relationship between boll number and the yield at the plot level, images from each plot were stitched together using the 'Auto Blend' tool in Adobe Photoshop CC 2017 (Adobe System Incorporated; San Jose, California, USA) to estimate the boll number for the whole plot. A total of 25 plot images, which were collected on Nov 03, 2016, were selected for yield prediction. All of the 25 plots were hand harvested and weighed. A linear regression model between estimated boll number and the fiber yield was built based on 15 plots, and the other 10 plots were used to evaluate the performance of the model.

4.3. Results

4.3.1 Boll recognition

Overall, the proposed segmentation method achieved good performance for boll recognition under both sunny and cloudy illumination conditions (Fig.7). Most bolls were successfully separated from the background, although there were false negative (FN) (Figure 4.7(b)) and false positive (FP) (Figure 4.7(d)) pixels as indicated by red circles in the figure. For images collected on sunny days, bolls under dark shadows had a higher possibility to be misclassified as background (FN) than bolls under direct sun light (Figure 4.7(a) and (b)). However, the FN pixels would not make a significant negative effect on further boll counting because the boll counting algorithm had great potential to correctly recognize a segmented region as a boll even if just a small part of a boll was misclassified (Figure 4.7(b)). In addition, the shadow effect could be reduced by selecting a suitable time window for data acquisition. For example, since shadow was mainly generated by the plant itself in this study, if data were collected around noon when sunlight was perpendicular to ground, shadowed area would be decreased. On the other hand, FP pixels could be generated from leaves with specular reflections such as those found on sunny days. For images collected under cloudy days (Figure 4.7(c)), all bolls were successfully segmented from the background, although there were still some FN pixels and FP pixels (Figure 4.7(d)). Compared to Figure 4.7(a), there was no obvious shadow areas in Figure 4.7(c), resulting in much less FN pixels. FP pixels were from leaves, which could result in overestimation of boll numbers. Fortunately, it is a common practice to spray cotton fields with hormonal defoliants such as Ginstar® or Finish® to artificially remove leaves from the plants so that very few leaves are left at the harvest stage. Furthermore, some algorithms such as size filtering could be used to further remove some FP pixels.

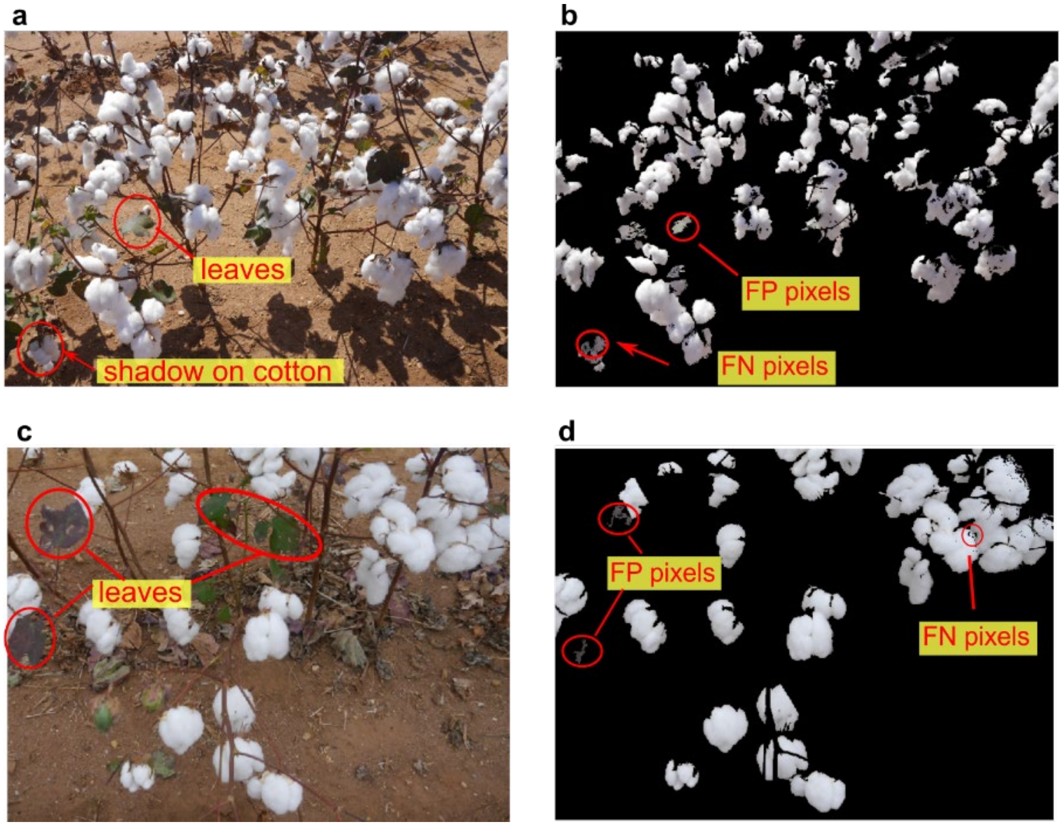

Figure 4.7. Representative results of cotton boll recognition under sunny and cloudy illumination conditions. (a) raw image in RGB color space under sunny day (Nov 03, 2016); (b) boll recognition results of (a). (c) raw image in RGB color space under cloudy day (Oct 07, 2016); (d) boll recognition results of (c). In order to present results clearly, in (b) and (d) foreground was marked as original color, and background was marked as black (pixel intensity was 0).

Statistical tests revealed that the performance of the proposed boll recognition method was robust under sunny and cloudy weather conditions in this study (Table. 4.1). For all three days, the *Pr* and *Re* were around 0.98, resulting in an F1 score of around 0.98.

Table 4.1. Performance of cotton boll recognition on different days and under different illumination conditions. Each day contained 70 images.

DAP	I.C.	Pr	Re	F1
116	Cloudy	0.97	0.98	0.98
128	Cloudy	0.98	0.99	0.99
143	Sunny	0.98	0.98	0.98

I.C. stands for illumination condition.

4.3.2 Boll counting

Algorithm 1 not only could merge disjointed regions of the same boll split by one branch, but also was suitable for bolls split by several branches (Figure 4.8(a) and (b)). In Figure 4.8(a-2), a boll was split into three disjointed regions by two branches, and just two regions were detected by the boll recognition operation. The boll was successfully detected by merging the two disjointed regions (Figure 4.8(b-2)). This example demonstrated that sometimes if part of a boll was not recognized, our methods still had chance to successfully detect it. Similar to Algorithm 1, bolls split by burrs could also be successfully merged into a single object using Algorithm 2 (Figure 4.8(c) and (d)). The limitation of this method was that it might merge individual bolls between which the minimum boundary distance was less than the threshold τ_3. This issue could be overcome by Algorithm 3 as described later in the subsection. Typical results of separating individual bolls in clusters were shown in Figure 4.8(e) and (f). If there was not too much overlap area between bolls in a cluster and individual bolls were tight and maintained a roughly round shape, Algorithm 3 usually could successfully separate individual bolls and obtain the exact number of bolls in a cluster (Figure 4.8 (e-1), (e-2) and (f-1), (f-2)). However, more complex situations were often encountered in field conditions. For example, some bolls overlapped too much in a cluster, and the cluster itself had complex shape with drooping fibers, as shown in Figure 4.8(e-3) and (e-4). Algorithm 3 achieved less desired splitting performance for these situations. The split number tends to overestimate the actual boll number within the cluster representing the main error source for boll counting.

Figure 4.8. Representative results of merging and splitting operations. (a) Bolls split by branches; (b) Detected bolls after merging operation using Algorithm 1; (c) Bolls split by sepals; (d) Detected bolls after merging operation using Algorithm 2; (e) Connected bolls; (f) Detected bolls after splitting operation using Algorithm 3.

There were situations where two bolls were mis-merged by Algorithm 2 but they were later successfully separated by Algorithm 3 (Figure 4.9). Conversely, two bolls were initially detected by Algorithm 1 (Figure 4.9(a)) but they were later merged by Algorithm 2 because the minimum boundary distance was less than the threshold τ_3 (Figure 4.9(b)). The mis-merged boll was successfully split into two individual bolls along the minor axis by Algorithm 3 (Figure 4.9(c) and (d)). Usually since there was no overlap for this kind of mis-merged bolls, they had relatively larger areas and elongation ratios than single bolls. Algorithm 3 had great potential to split them into exact individual bolls.

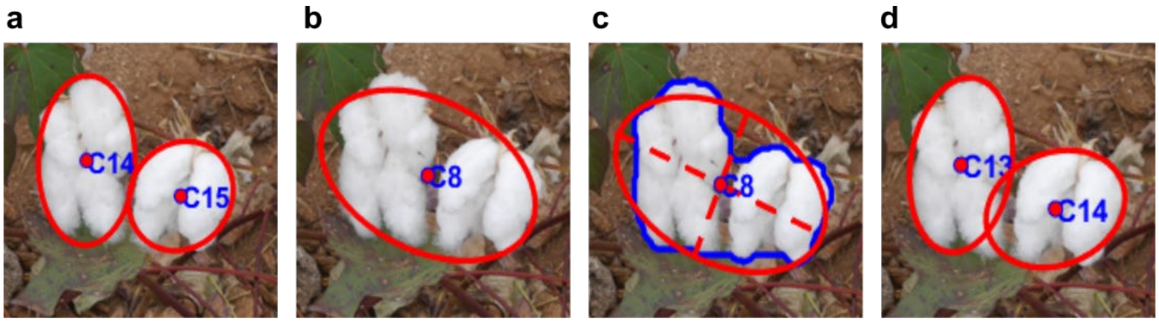

Figure 4.9. Example of two bolls mis-merged by Algorithm 2, but successfully split by Algorithm 3. (a) Two bolls detected by Algorithm 1. (b) Bolls merged as one by Algorithm 2. (c) Shape and size features of the merged boll. Solid blue lines depicted boundary, dashed red lines depicted major and minor axes. (d) The cluster was successfully separated into two individual cotton bolls. Each detected boll was denoted by an ellipse generated by major and minor axis with the central point.

Boll counting accuracy generally decreased for the three days' data (Table. 4.2). This was not unexpected because more bolls were drooped as the season progressed, which resulted in more and more bolls clustered together, thereby limiting the performance of Algorithm 3 as explained in Figure 4.8. The accuracy for all three datasets were over 80%, with the best accuracy achieved on 116 DAP at 84.6%. The results showed that over-splitting was higher than over-merging, resulting in overestimation of cotton boll numbers.

Table 4.2. Performance of cotton boll counting on different days (μ denotes mean and σ denotes standard deviation). Each day contained 70 images.

DAP	MAPE (%)	RMSE	OSR (%)	OMR (%)
116	15.4	7.4	11.7	1.2
128	17.8	9.7	16.6	3.8
143	18.5	10.0	16.2	3.1

The best R^2 value between sensor-detected and manually-counted boll numbers was obtained from the data collected on 116 DAP, however, the values from different DAP were very close to each other (Figure 4.10). Although the R^2 in Figure 4.10(c) was a little higher than that in Figure 4.10(b), it was reasonable since the accuracy was affected by several other factors such as the maturity group of a cultivar and errors from manual counting. For example, the cultivar UA48 has an early maturity (or short season) growth habit, therefore the bolls are opened much earlier in the growing season, resulting in a higher number of bolls drooping during harvest when compare to cultivar such as GA201074 which has an indeterminate (or long season) growth habit. For the later cultivar, the best bolls opened at a relatively much later date, resulting in a relatively tight and regular shape during harvest. For manual counting, since bolls were counted from images, it was challenging to get the exact boll numbers when encountering much overlap.

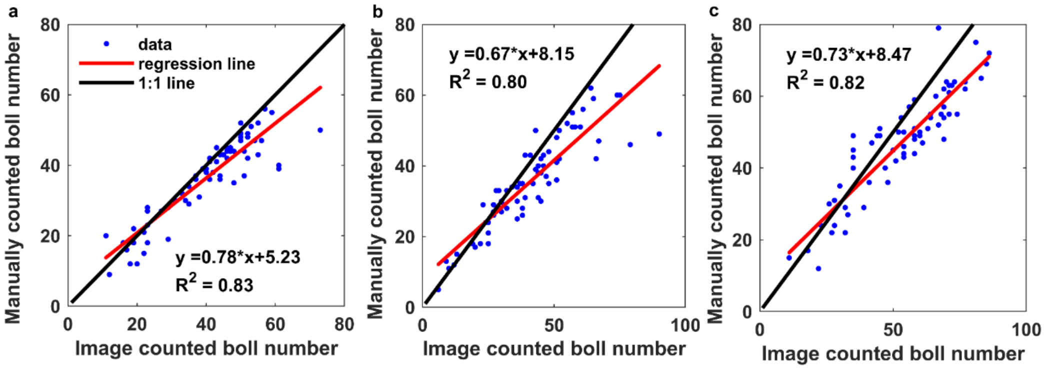

Figure 4.10. Correlation analysis between image and manual measurements of boll counting using images collected on (a) 116 DAP; (b) 128 DAP and (c) 143 DAP. Each day contained 70 images.

4.3.3 Yield prediction at the plot level

As an important yield component, information about boll number could be highly useful to cotton breeders as well as growers to assess the yield of experimental and commercial genotypes.

Therefore, boll number counting was conducted at the plot level after multiple images belonging to one plot were stitched together to form an image for the plot (Figure 4.11). Although not all bolls can be seen in 2D images due to occlusion of branches and other bolls, yield can be estimated based on detection results from 2D images, assuming that there exists a consistent relationship between the bolls shown in 2D images and the actual number of bolls.

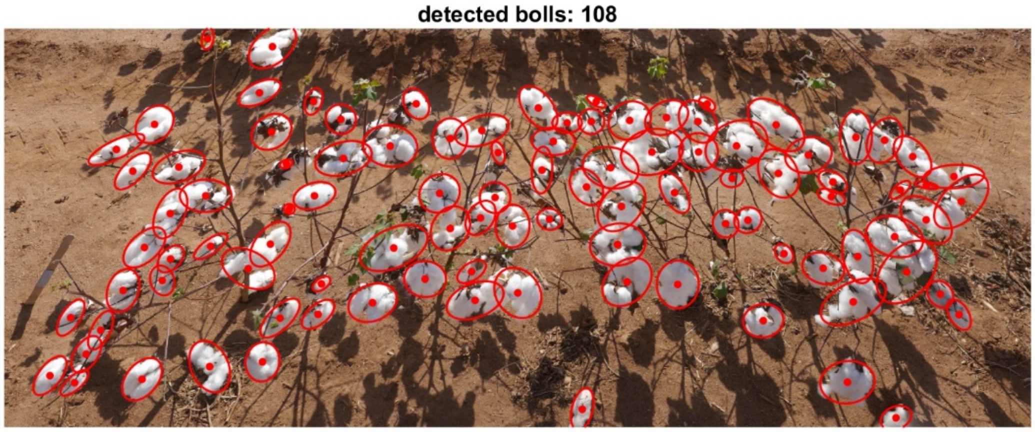

Figure 4.11. Example of boll counting for a plot. Each detected individual boll was indicated by an ellipse with its centroid point.

The number of bolls detected by the sensor was highly correlated with the number counted from the stitched images manually at the plot level, although the R^2 was less than that from single images (Figure 4.12). One potential reason could be due to image distortion created by the image stitching method utilized. More advanced image stitching algorithms (Zhu et al., 2016) and sensors such as cameras with wider field of view or even 360° cameras (Brown et al., 2012) will be explored to obtain plot-level images in the future in order to reduce the impacts.

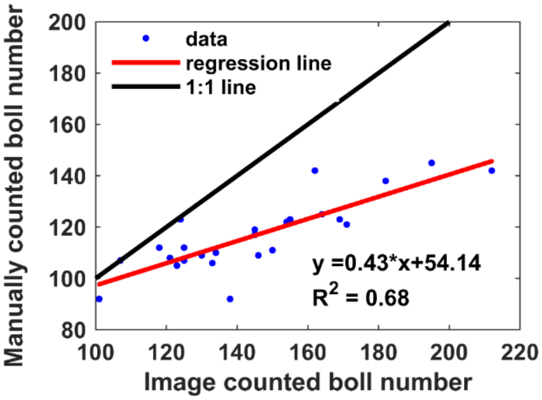

Figure 4.12. Correlation analysis between image and manual measurements of boll counting at the plot level. A total of 25 plots were selected for yield prediction analysis.

The image counted boll numbers correlated well with the fiber yield (Figure 4.13(a)), although the R^2 value (0.53) was less than that with the manually counted boll numbers (Figure 4.12). This was reasonable since the yield depended not only on the number of bolls, but also on other factors such as boll volume and fiber density. Based on this model, the yield of the other 10 plots were estimated with an MAPE of 8.92% and an RMSE of 99 g (Figure 4.13(b)). The result indicated that the proposed method could provide accurate fiber yield prediction, which was useful for breeders.

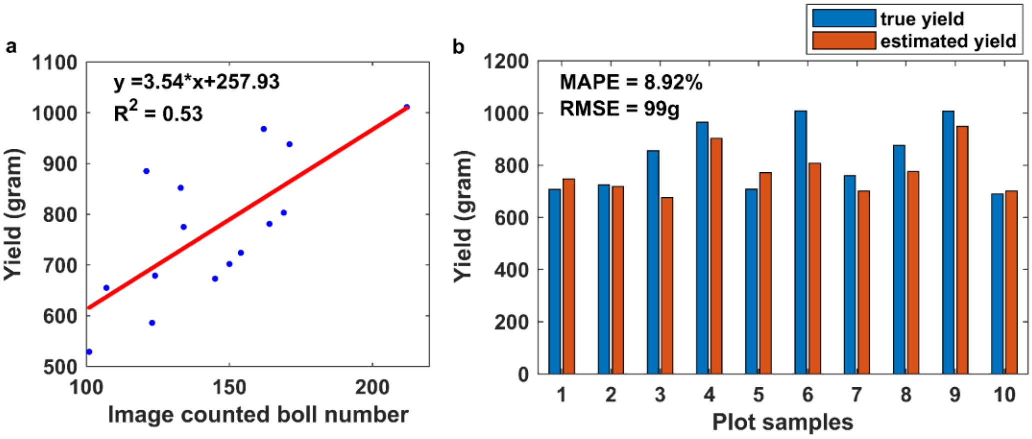

Figure 4.13. Yield prediction results. (a) A linear fit model built based on the data of 15 plots between yield and image detected cotton bolls. (b) The estimated cotton bolls against the ground truth yield for another 10 plots.

4.4. Discussion

This study demonstrated that the proposed boll recognition and counting methods could recognize and estimate cotton boll numbers reliably in field plots. Images were collected during late boll opening when very few leaves were left, resulting in a relatively simple background compared to a prior study (Li et al., 2016). The background mainly included plant stems, branches and soil, all of which had significant contrasts in color compared to white cotton bolls. In addition, the camera was equipped on a robot platform with a 45° downward angle. This setup removed other potential interferences such as sky from the field of view. These factors resulted in good cotton boll recognition performance with a relative simple image segmentation method. For boll counting, Algorithms 1 and 2 were effective in connecting disjointed regions of the same bolls. Algorithm 3 not only performed well in splitting a cluster with two bolls into individual bolls, but also showed potential to handle complex clustering situations. However, Algorithm 3 might not get the exact boll number with several bolls inside a cluster that has a very complex shape. This method may also not derive the real boundaries for individual bolls. This was the key error source for boll counting. It was mainly due to the splitting operation—splitting a cluster along the minor axis which did not work effectively under these conditions. The performance of the proposed method could be further improved if more advanced and complex features could be designed in the future. CNN technologies are effective to extract features from images and have been applied for object detection in agriculture applications (Bargoti and Underwood, 2017; Rahnemoonfar and Sheppard, 2017). A CNN-based image processing pipeline is under exploring for cotton boll detection by the authors. However, CNN-based methods need a training dataset which usually needs many labeled images, and the training process takes long time, depending on the size of the training dataset and computing capability. Based on our preliminary results, sometimes the trained network missed cotton bolls as well even if they were obvious in images. The challenge is that CNN sometimes is hard to explain why misclassifications happened. Therefore, methods with traditional computer vision technologies are still valuable for these applications. Another potential is to apply 3D point cloud based methods (Malambo et al., 2019), since 3D point clouds obtain depth information which is very useful to deal with occlusion problem which is one the biggest challenges for image-based methods. Further, 3D data would provide information not only for boll counting, but also for quantifying the spatial distribution. However, the cost of sensors (such as LiDAR) and computing resources will also increase.

Our method had a higher over-splitting rate than over-merging rate (Table. 4.2), resulting in overestimation of the number of cotton bolls (Figure 4.10 and 12). This effect could be reduced by applying adaptive parameters for each input image when conducting merging and splitting operations. For clusters in which overlap among individual bolls was usually less than half of a boll, Algorithm 3 was able to discern individual bolls even in clusters of 4-5 bolls. However, the performance decreased for clusters with complex shapes and much overlap among bolls, particularly involving open bolls with cotton drooping out, which had much more varied shapes than fruit with rigid shapes such as apples (Bargoti and Underwood, 2017) and litchis (Wang et al., 2016a). This situation could be avoided by selecting image collection time windows. Although relatively better accuracy can be obtained in the early stage of boll opening, there still exist unopened bolls in this stage and counting would be less precise because the white color of fiber is needed for contrast. If it is too late in season, bolls would be fully open and fiber drooped, which is not good either since it increases the possibility that bolls overlap in images. Therefore, the best timing for boll detection and counting would be when all cotton bolls are open but before the fibers start to droop. Counting errors were also observed in manual counting data, since it was very challenging to get the exact number of bolls in large clusters with more overlap. While this study partially solved cluster and overlap problems for boll counting in 2D images, capturing images with multiple views instead of a single view has the potential to improve counting accuracy.

In this study, images were collected at 1 Hz due to the limitation of the camera utilized. The throughput could be improved by using a camera with a higher frame rate (Bargoti and Underwood, 2017). In terms of image processing, the average running time was 1.65 s for each image, which could be improved by using faster computing resources. Compared to tractor based platforms, robot based platforms have greater flexibility, for example, to enter fields in wet conditions due to light weight and to cause less soil compaction. Compared to UAV based platforms, the robot-based platform could take images with much higher resolution, which is important for image processing especially when considering clustered and occluded bolls for boll counting. Moreover, not only top-view but side-view images can be obtained using a robot platform. In this study, the experimental field had a row spacing of 1.52 m, much wider than in commercial farms (0.91 m). Narrower row spacing may require use of custom-designed robots such as the portable Phenomobile Lite unit (Rebetzke et al., 2016).

It should be noted the image acquisition system and analysis algorithms developed in this study had some drawbacks. The first one is that the robot was under manual control during image collection. An autonomous navigation program would improve the autonomy of the system and enhance throughput. The input for boll counting algorithm included a segmented image and five parameters which were determined by the configuration of the camera and plant related features. Three of them (τ_1, τ_4, τ_5) could be fixed for use and the remaining two (τ_2, τ_3) need to recalculate based on eq. (4.2) for future applications. However, the parameters may be influenced by factors specific to the cultivars and environment studied. Automatic methods for parameter determination would be preferable in the future.

4.5. Conclusions

Good performances were achieved for boll recognition by a boll segmentation method under both sunny and cloudy weather conditions in the field. The boll counting algorithm achieved an accuracy of around 83%. The main source of error for counting was due to over-splitting of bolls overlapping each other in 2D images. This could be potentially addressed using 3D imaging in the future. Boll counting and yield estimation at the field plot level were promising, potentially leading to more efficient evaluation of experimental plots by agronomists and/or breeders, and of commercial fields. Accurate boll counting could lead to more efficient evaluation of experimental plots by agronomists and/or breeders, promising more rapid cotton improvement; and of commercial plots by growers, promising more effective crop management.

CHAPTER 5

THREE-DIMENSIONAL PHOTOGRAMMETRIC MAPPING OF COTTON BOLLS IN SITU BASED ON POINT CLOUD SEGMENTATION AND CLUSTERING[4]

---

[4] Sun, S., Li, C., Chee, P., Paterson, A., Jiang, Y., Xu, R., Robertson, J., Adhikari, J., Shehzad, Tariq., Submitted to *ISPRS Journal of Photogrammetry and Remote Sensing*, May 23, 2019.

Abstract

Three-dimensional high throughput plant phenotyping techniques provide an opportunity to measure plant organ-level traits which can be highly useful to plant breeders. The number and locations of cotton bolls, which are the fruit of cotton plants and an important component of fiber yield, are arguably among the most important phenotypic traits but are complex to quantify manually. Hence, there is a need for effective and efficient cotton boll phenotyping solutions to support breeding research and monitor the crop yield leading to better production management systems. We developed a novel methodology for 3D cotton boll mapping within a plot *in situ*. Point clouds were reconstructed from multi-view images using the structure from motion algorithm. The method used a region-based classification algorithm that successfully accounted for noise due to sunlight. The developed density-based clustering method could estimate boll counts for this situation, in which bolls were in direct contact with other bolls. By applying the method to point clouds from 30 plots of cotton plants, boll counts, boll volume and position data were derived. The average accuracy of boll counting was up to 90% and the R^2 values between fiber yield and boll number, as well as fiber yield and boll volume were 0.87 and 0.66, respectively. The 3D boll spatial distribution could also be analyzed using this method. This method, which was low-cost and provided improved site-specific data on cotton bolls, can also be applied to other plant/fruit mapping analysis after some modification.

5.1 Introduction

Crop demand is expected to increase due to the expanding global population (Cordell et al., 2009; Gerland et al., 2014; Tester and Langridge, 2010). New plant breeding approaches that improve rates of genetic gain can help to meet this demand. Plant phenotyping techniques, which provide measurements of phenotypic traits and assessments of plant development and performance, are increasingly used in crop breeding and research, and have become a rapidly evolving focus area in agriculture applications (Czedik-Eysenberg et al., 2018; Granier and Vile, 2014; Großkinsky et al., 2015). However, high throughput phenotyping, especially noninvasive field-based phenotyping, is still a major bottleneck in plant breeding and crop improvement (Campbell et al., 2018; Furbank and Tester, 2011).

To address this bottleneck, remote sensing combined with computer vision technologies have been increasingly used for plant phenotyping at both the canopy level and plant organ level such as cotton boll (Li et al., 2017), wheat ear (Velumani et al., 2017) and sorghum panicle (Malambo et al., 2019). These technologies provide opportunities to image plants with a high spatial resolution and help extract phenotypic traits effectively and efficiently. Specifically, three-dimensional (3D) model based phenotyping methods have received significant attention for plant scientists during the past decade (Gibbs et al., 2017; Gongal et al., 2015; Vazquez-Arellano et al., 2016). Depth information is provided by 3D models that address occlusion which is one of the biggest challenges for image-based methods. In addition, by using such a technique, a wider variety of phenotypical traits can be extracted. Three-dimensional models also improve opportunities to derive new traits from the same model at a later date, which is more difficult for 2D image-based approaches (Gibbs et al., 2017). Much effort has directed toward the application of 3D technologies in agriculture, such as in crop biomass estimation (Wallace et al., 2017; Wang et al., 2016b), plant architectural trait analysis (Bao et al., 2019; Conn et al., 2017; Guo et al., 2018a), digital elevation model generation (Toda et al., 2017), and dynamic crop growth monitoring (Dong et al., 2016; Duan et al., 2016; Pearse et al., 2016). For cotton, several studies were conducted for plant morphological trait measurement under field conditions using different

3D reconstruction methods such as utilizing Kinect-v2 sensors (Jiang et al., 2017), light detection and ranging (LiDAR) (Sun et al., 2018b) and RGB cameras (Xu et al., 2019). However, only plot level traits such as plant height, projected canopy area, and plant volume in these studies were measured due to limited point cloud resolution.

In recent years, much effort has been made toward detecting plant organ-level traits, that required more accurate point clouds and more advanced data processing methods. Several studies demonstrated that highly dense and accurate point clouds could be obtained by precision 3D sensors (Conn et al., 2017; Guo et al., 2018b; Paulus et al., 2014b) and reconstructed using multi-view images (Duan et al., 2016; Herrero-Huerta et al., 2015; Paproki et al., 2012). Plant organ-specific traits, such as the dimension features of leaves and stems were accurately measured by custom developed algorithms. Although 3D sensor-based methods were more effective and efficient than the SfM-based methods, the sensors are very expensive. The two SfM-based studies (Duan et al., 2016; Paproki et al., 2012) did not mention any illumination effects on point clouds when processing their data, since they were conducted under indoor conditions with a controlled illumination environment. Nguyen et al. (2016) developed a mobile ground mobile platform with 32 cameras was developed to capture images of single plants simultaneously from different perspectives under field conditions, and the system demonstrated that accurate point clouds could be obtained from the images. A field study was conducted by Underwood et al. (2016) to analyze the characteristics of flower and fruit distribution in individual almond plants. Flowers and fruits were detected in images and then projected to a low-resolution 3D point cloud obtained by a 2D line scan LiDAR. Although spatial data were obtained for the detected objects, occlusion was still difficult to contend with for image-based detection. Most recently, Velumani et al. (2017) introduced a wheat ear detection method using mobile laser scanning data. Two methods—voxel-based segmentation and mean shift segmentation—were used to segment wheat ears from the background and then an Ostu's threshold-based method was applied to classify ear segments from leaves and stems with an average detection rate of 85%. Malambo et al. (2019) presented field-based, individual sorghum panicle detection from point clouds obtained using a high-precision LiDAR. While an average accurate rate of ~89% was achieved, the performance of point cloud filtering operation was not robust because it relied solely on color features. In addition, as is common under field conditions, objects in direct contact with each other were not accounted for.

In this study, we proposed a data processing pipeline for detecting and characterizing individual cotton bolls from 3D point clouds that were obtained from image-based methods. Cotton (*Gossypium spp.*) was used as the model crop because it is among the most economically important fiber crops and the United States (US) is one of the top counties producing cotton. Around 79% of the natural fiber is produced from cotton in the whole world (Townsend and Sette, 2016). In 2017, an estimated 12 million acres of cotton were grown in the US, resulting in a value of around 7 billion for the US cotton industry (USDA, 2018a). Cotton boll, as a yield-related component, can be used as an indicator for fiber prediction, and from which physiological and genetic mechanisms of plant growth and development can be derived. Based on the review of plant phenotyping literature, detection and characterization of cotton bolls using 3D technologies remains unexplored. A similar study worked on cotton boll segmentation in color images (Li et al., 2017), but it did not count the number of bolls nor estimate the size of the bolls. While several studies have been done to detect organ-specific traits of other plants or crops from point clouds, these techniques, especially point cloud processing methods, can be further improved (Duan et al., 2016; Malambo et al., 2019). For example, in order to improve point cloud segmentation performance, features which are not related to color information were explored; Additionally, the detection of individual objects from a cluster, in which several single objects are physically connected, is still a challenge. Specifically, cotton bolls have varied and complex shapes–closed bolls can vary substantially in size, and open bolls can have a variety of shapes based on emerging cotton fibers, resulting in serious occlusion issue compared to other fruits with a more rigid structure, such as apples.

The overall goal of this study was to develop a data processing pipeline for detecting and counting individual cotton bolls from 3D point clouds reconstructed from multi-view images using SfM under field conditions. The specific objectives were to (1) implement a mobile 3D image acquisition system in the field; (2) develop a region-based semantic point cloud segmentation algorithm for foreground boll voxel recognition; (3) develop a density-based clustering algorithm for individual cotton boll detection and counting; (4) validate the performance of the proposed method as compared to the ground truth.

5.2 Materials and Methods

5.2.1 Experimental fields and image collection

The plant materials used in this study were planted in two experimental fields—a University of Georgia statewide variety testing field (SVT) and a nested association mapping (NAM) field—located at Iron Horse Farm in Greene County, GA, USA (Figure.1). Five Fuji X-A10 cameras (Fujifilm Holdings Corporation, NY, USA), which were mounted on a tractor platform, were used to scan the plants. One camera was set to photograph the plants from the top and the other four were mounted on one side of the plot to scan plants from a side view in order to ensure that there was enough overlap between adjacent images (Figure 5.2a and b). Therefore, the tractor had to go through each row twice in order to scan both sides of the plants. A custom-made scale bar was placed in front of each plot during image collection (Figure 5.2c). The rectangular scale bar consisted of four markers (marker 73, 74, 75 and 76 in Figure 5.2c). The horizontal edge was 0.2 m, and the vertical edge was 0.08 m. A local 3D Cartesian coordinate system could be built when coordinates of the four markers (73, 74, 75 and 76) were assigned, such as (0.1, 0.04, 0), (0.1, -0.04, 0), (-0.1, 0.04, 0), and (-0.1, -0.04, 0), respectively. A trigger device was developed to enable all five cameras to capture images at the same time, with a frequency of 1.5 frames per second. When scanning the plants, the cameras were configured to be in shutter-priority mode with a shutter speed of 1/250 s, and the tractor speed was around 0.2 ~ 0.3 m/s, resulting in approximately 10 to 15 seconds for one-side scanning (20 to 30 seconds for full scanning of one plot). Therefore, there were approximately 150 ~ 225 images collected per plot at a length of ~ 3 m. The 3D reconstruction was conducted using the SfM algorithm, which was implemented via Agisoft PhotoScan software (Geoscan. Inc., Moscow, Russia). The four markers could be automatically detected by the software, and the prebuilt 3D coordinate system could be used as hyper parameters for the software to calibrate the actual size of the reconstructed 3D point clouds.

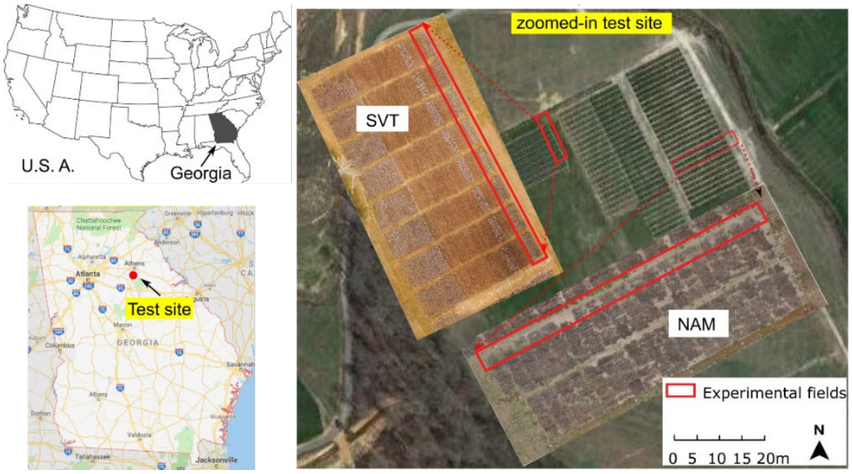

Figure 5.1. Experimental fields. Experiments were conducted in two fields. One was called SVT field and the other was NAM field.

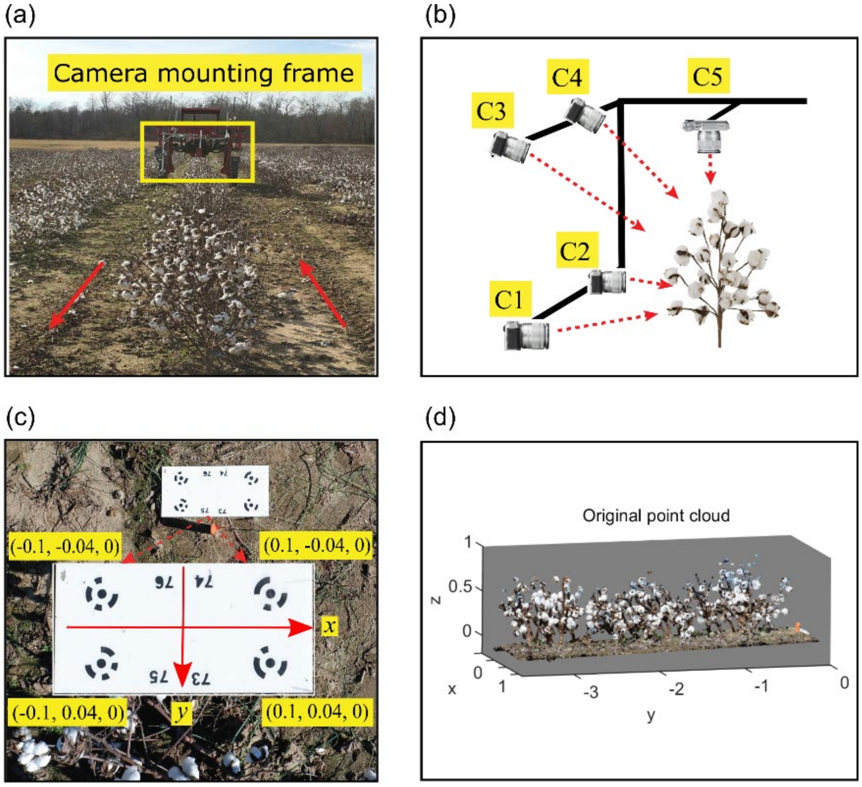

Figure 5.2. Multi-view image acquisition system and plant 3D point cloud reconstruction. (a) Multi-view cameras mounted on a tractor platform. (b) Camera layout information. (c) A scale bar used to build a local 3D Cartesian coordinate system and calibrate the size of reconstructed 3D point cloud; (d) Example of a reconstructed point cloud for a plot with around 4 million points.

The first image collection was conducted on Nov 24, 2017 in the SVT field, and a total of 15 plots were scanned. The second collection was on Dec 14, 2017 in NAM field with another 15 plots being scanned. Hand-harvesting was conducted just after each image collection. The boll numbers for each plot were counted, and the yield was weighed. The summary of the hand harvesting is presented in Table 5.1.

Table 5.1. Ground truth data of boll number and fiber yield. A total of 15 plots for each dataset.

Field	**Boll number**			**Yield (g)**		
	Min	**Max**	**Mean**	**Min**	**Max**	**Mean**
SVT	85	349	218	330	1474	845.5
NAM	37	377	206	113	1633	747.3

5.2.2 Cotton boll detection and characterization

The 3D Cotton boll detection and characterization algorithm developed in this study worked on plot-level point clouds and involved three main steps. The first phase consisted of point cloud preprocessing. Next, point cloud segmentation occurred, which was meant to exclude branch points from point clouds. This operation relied on characteristic differences such as color and shape features observed between branches and bolls. Finally, individual bolls were detected based on the point density and boll size features, deriving boll number as well as volume, and position traits.

5.2.2.1 Point cloud preprocessing

Point cloud preprocessing included ground plane removal and point cloud rotation. The ground plane was removed by setting a threshold at z_h = 10 cm along the z axis direction since it was not useful for the subsequent data processing. Although every precaution was taken to place a scale bar, the y axis of the local coordinate created by the scale bar (Figure 5.2c) may not be aligned well with the planting line, resulting in an angle α between the x axis and the planting line (root base) (Figure 5.3a). Therefore, the planting line needed to be estimated in order to conduct point cloud rotation. To do this, a 3cm thick slice was cut starting from the bottom of the point cloud and a 2D density-based spatial clustering of applications with noise (DBSCAN) (Wierzchoń and Kłopotek, 2018) was then applied to cluster the sliced points with only x and y coordinates (Figure 5.3b); the two parameters—*minPts* which specifies how many neighbors a point should have to be included into a cluster, and *Eps* which specifies how close points should be to each other for a cluster, were set to be 5 and 2 cm for the 2D DBSCAN operation, respectively. The local mean x, y coordinates were used to represent the location of each cluster (Figure 5.3c), and a line was fit by random sample consensus (RANSAC). The fit line was considered to be the planting line.

Finally, the point cloud was rotated $(90 - \alpha)$ around the z axis by eq (5.1) to ensure that the planting line was at $x = 0$.

$$R_z(90-\alpha) = \begin{pmatrix} \cos(90-\alpha) & \sin(90-\alpha) & 0 & 0 \\ -\sin(90-\alpha) & \cos(90-\alpha) & 0 & 0 \\ 0 & 0 & 1 & 0 \\ 0 & 0 & 0 & 1 \end{pmatrix} \tag{5.1}$$

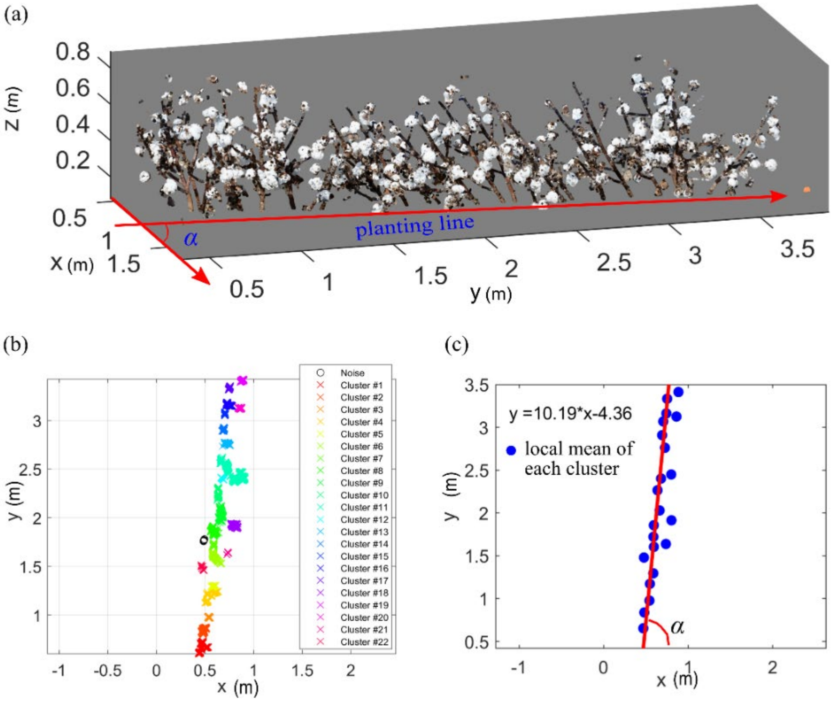

Figure 5.3. Rotation of a 3D point cloud. (a) An angle α between the x axis and the planting line was generated because the scale bar was not well aligned during data collection. (b) Clustering results of the 3 cm thick slice points. (c) A line (in red) was fit using RANSAC to calculate the angle α for rotation operation.

5.2.2.2 Point cloud segmentation

5.2.2.2.1 Over-segmentation of point clouds

Regions, which can result from over-segmentation methods, provide better spatial support from which to compute richer feature representations as compared to single points (Rusu, 2010; Tao and Zhou, 2017). The purpose of over-segmentation methods is to merge the points that are close enough in terms of predefined attributes. The output is a set of clusters, each one is a set of points. In this study, a voxel cloud connectivity segmentation (VCCS) algorithm (Papon et al., 2013), which is a region growing method incrementally expanding supervoxels from a set of seed voxels, is applied to produce over-segmented regions in order to perform boll points segmentation from the branch points. The general process of VCCS is as follows: the original point cloud is voxelized with a resolution of R_{voxel}. Each voxel can be represented in a 39-dimensional space (eq (5.2)).

$$F = \left\{x, y, x, L, a, b, FPFH_{1,2,\cdots,33}\right\} \tag{5.2}$$

where x, y and z are values of a local Cartesian coordinate system, L, a and b are intensities in the CIELab space, and $\text{FPFH}_{1\ldots33}$ are the 33 elements of a fast point feature histogram (FPFH), which is feature vector describing the voxel geometrical characteristics (Rusu et al., 2009). Then the voxel cloud space is divided into a voxelized grid with a resolution of R_{seed}. R_{seed} is significantly higher than R_{voxel}. For each grid of voxels, a seed voxel is initialized by selecting the voxel nearest to the center of the grid. Seed voxels are then moved to the connected voxel which has the smallest gradient within R_{seed} of the seed center. Supervoxels are grown by assigning voxels to seed voxels iteratively according to a distance measure calculated in F using eq (5.3).

$$D = \sqrt{\omega_c D_c^2 + \frac{\omega_s D_s^2}{3R_{seed}^2} + \omega_n D_n^2} \tag{5.3}$$

where D_c is the Euclidean distance in CIELab space, D_s is the spatial distance, which is normalized by the seeding resolution, and D_n is an angle distance between surface normal vectors in FPFH space. Parameters ω_c, ω_s and ω_n are color, spatial and normal weights. For a cluster center, a nearest voxel is selected, and starting from which adjacent voxels are selected through flowing outwards, the distances between the voxels and the center are calculated. If the distance is the smallest this voxel has been seen, its label is set. Once all voxels are assigned, the center of each supervoxel is updated by taking the mean of all its constituents. This is repeated either until the cluster centers stabilize, or for a fixed number of iterations. VCCS takes advantage of 3D geometry so that the over-segmentations conform to object boundaries better than existing methods while maintaining processing efficiency. A typical single boll was like a sphere, with diameter ranging from 5 to 10 cm (i.e., volume from 133 to 523 cm3). So, R_{seed} and R_{voxel} were selected as 8 cm and 2 mm, respectively, and the color, spatial and normal weights were set to be equal importance, i.e., $\omega_{\mathrm{c}} = 1$, $\omega_s = 1$ and $\omega_n = 1$.

Color-based region growing segmentation (CRGS) is another commonly used region growth method, which can produce over-segmented regions from point clouds. CRGS generates regions based on RGB color differences and Euclidean distances between the seed point and its neighboring points (Tao and Zhou, 2017). The general process of CRGS is as follows: a point with the minimum curvature value is picked from the original point cloud, and then is added to the set called seeds. The color differences in RGB space are calculated between the seed point and its neighboring points. If the difference is less than a predefined threshold t_c, the neighboring point is added to the current region. After every neighboring point is tested, the spatial differences between seed point and the neighboring points are calculated. If the difference is less than a threshold t_s, then the point is added to the seeds, and the current seed point is removed. Repeat this process until the seeds set is empty, resulting in a region. The procedure iterates until there are no labeled points in the original points. The parameters t_c was selected as a small value, $t_c = 10$, in order to get small scale over-segmented regions, and t_s was set to be 8 cm which was the same to the parameter R_{seed} in VCCS. We compared the two methods for cotton boll counting.

5.2.2.2.2 Feature extraction

A 97-demensional feature vector including color features, spatial features and shape features was extracted from each over-segmentation to describe the point cloud data. Denote $R = [p_1, p_2, \ldots, p_n]$ as an over-segmented region, where each point p_i contains Cartesian coordinates (x_i, y_i, z_i) and point intensity in an RGB color space (R_i, G_i, B_i). Obviously, we observed significant differences between foreground boll points and the points in the background in terms of color. Therefore, color information was a good descriptor for the region features. In this study, an 64-dimensional vector was extracted from RGB, HSV color spaces, which was histogram distributions of sixteen bins in channels R, G, B and S (Li et al., 2016; Sun et al., 2018a). Although the color of the points could be described in an RGB color space, the points in HSV color space showed fairly good light-interference resistant capabilities (Tao and Zhou, 2017).

Geometric features, including spatial features (Zhou and Tuzel, 2017) and shape features (Munoz, 2013; Verdoja et al., 2017), were required since some branches had almost the same color as the bolls due to the effects of sunlight during field image collection. For spatial features, the local mean was computed as the centroid of a region, denoted as (v_x, v_y, v_z); then the distance between each point p_i and the centroid was computed and denoted as $S = (x_i - v_x, y_i - v_y, z_i - v_z)$, $i = 1, 2, \ldots, n$. For each axis, a histogram distribution with 10 bins was computed, resulting in a 30-dimension feature vector for x, y and z coordinates. Shape features were extracted from the covariance matrix of a region. Let K_{XX} be the covariance matrix of a region X with N_p points (eq (5.4) and (5.5)), and $\lambda_0, \lambda_1, \lambda_2$ $(\lambda_0 > \lambda_1 > \lambda_2)$ be the eigenvalues of K_{XX}.

$$K_{xx} = \frac{1}{N_p} \sum_{q \in N_p} \left(q - \mu_p\right)\left(q - \mu_p\right)^T \tag{5.4}$$

$$\mu_p = \frac{1}{N_p} \sum_{q \in N_p} q \tag{5.5}$$

The three-dimensional eigen value vector $\{\lambda_0, \lambda_1, \lambda_2\}$ can be used as the region shape feature descriptor. If $\lambda_0 >> \lambda_1, \lambda_2$, the region has a linear structure, such as branches of cotton plants; if $\lambda_0 \approx \lambda_1 \approx \lambda_2$, the region has a spherical structure, such as cotton bolls in this study; and $\lambda_0, \lambda_1 >> \lambda_2$, the region has a planar structure.

5.2.2.2.3 SVM-based classifier

Support vector machine (SVM), which has good generalizability in pattern recognition and strong robustness and calculation capabilities (Vapnik, 2013), was used to train a classification model to discriminate between boll points in the front and the background points. A total of 651 over-segmentations with two categories—bolls and branches—were manually labeled based on a custom developed tool using MATLAB 2018b (The Math Works Inc., Natick, MA, USA). There were 328 boll samples and 323 branch samples, respectively. The dataset was divided into training and validation subsets with a ratio of 0.7: 0.3. During model training, a radial basis function (RBF) kernel was used and punishment parameter C and kernel parameter γ were tuned based on a grid-search and 5-fold cross validation methods. After SVM classification, a color filter was used to remove black exocarps of cotton bolls.

5.2.2.3 Point cloud clustering

After obtaining boll points from the point cloud segmentation operation, individual cotton bolls are detected by a clustering-based algorithm relying on point density and boll size features. For two single bolls, usually there was a gap between them if they were not in direct contact with each other, resulting in different point density distributions.

The 3D DBSCAN clustering algorithm was firstly applied to group boll points into clusters. The parameter *Eps* of DBSCAN was set to be 2 cm, considering that most bolls were larger than that; the other parameter *MinPts* could be selected from a wide range from 5 to 15, which did not affect the result much. *MinPts* = 10 was used in this study. The output clusters were divided into three categories according to cluster volume: noisy clusters, single boll clusters and multi-boll clusters. A cluster was considered to be noisy if its volume was less than 1 cm^3, and it was removed by a size filter. For single boll clusters, each cluster was considered as a single boll; while multi-boll clusters included multiple bolls inside, which had larger volume than a single boll. Once boll numbers in a multi-boll cluster were estimated, the whole boll counts could be obtained.

The boll numbers in a multi-boll cluster could be estimated through the quotient between the contact cluster volume and the average single boll volume, v_m (Miller et al., 2017). We assumed that most clusters consisted of single bolls with a typical volume (hereafter, regular bolls) though some were multi-boll clusters with larger volume and some were single bolls with smaller volume.

Let V be a set of volumes for clusters.

$$V = \{v_1, v_2, \cdots, v_n\} \tag{5.6}$$

A square matrix M could be obtained by eq (5.7).

$$M_{ij} = \lfloor v_i / v_j \rceil, \quad i, j = 1, 2, \cdots, n \tag{5.7}$$

where $\lfloor \bullet \rceil$ was a round function; each row of M was the rounded volume ratio between v_i and v_j. The number of unit values (ratio = 1) in each row of M was counted and stored in a vector K.

$$K = \{k_1, k_2, \cdots, k_n\} \tag{5.8}$$

The mode (the value in a set of data appearing most often) of the elements in K was calculated, denoted by e. The index of elements whose value equals e in K was calculated using eq (5.9). If $d_i = 1$, it meant the ith cluster is a regular boll.

$$d_i = \begin{cases} 1 & k_i = e \\ 0 & k_i \neq e \end{cases} \tag{5.9}$$

The average volume v_m of the regular bolls was calculated by eq (5.10).

$$v_m = \frac{\sum_{i=1}^{n} v_i \times d_i}{\sum_{i=1}^{n} d_i} \tag{5.10}$$

Then, the regular boll index and the corresponding average volume v_m were updated using eq (5.11) and (5.10), respectively.

$$d_i = \begin{cases} 1 & \lfloor v_i / v_m \rceil = 1 \\ 0 & \lfloor v_i / v_m \rceil \neq 1 \end{cases} \tag{5.11}$$

The updating steps were repeated until v_m did not change. For a multi-boll cluster, the volume was divided by v_m and the quotient was rounded to produce the boll counts. After that, a 3D *k*-means clustering method was applied to obtain the boundaries of individual bolls.

Algorithm 1: boll counting

```
Input:  $pt$      # boll points
Output: $N$     # the total boll number
    Initialize $N = 0$
    $C = DBSCAN(pt)$
    $C \leftarrow denoise(C)$
    $C = \{c_1, c_2, \cdots, c_n\}$   # $C$: clusters output from DBSCAN with denoise operation
    $V = \{v_1, v_2, \cdots, v_n\}$   # $V$: clusters volume calculated using convex hull
    $v_m = \Omega(V)$     # $\Omega(\bullet)$ is the function to calculate average volume of regular bolls
    for $i = 1$ to $size(V)$ do
        $q = \lfloor \frac{v_i}{v_m} \rceil$
        if $q \leq 1$ then
            $N \leftarrow N + 1$
        else
            $N \leftarrow N + q$
        end
    end
```

In addition to boll numbers, other cotton boll data such as boll volume and boll position could be calculated when the individual bolls were detected. The volume of a cotton boll was estimated using the convex hull method, and the local mean of x, y and z coordinates was used to represent the position of the boll.

5.2.3 Validation and statistical analysis

In order to validate the performance of the proposed boll counting algorithm, the mean absolute percentage error (*MAPE*) was computed between the algorithm measuring boll numbers B_i and the manual measurements m_i by eq (5.12). P was the number of plots.

$$MAPE = \frac{\sum_{i=1}^{P} \frac{|B_i - m_i|}{m_i}}{P} \times 100\% \tag{5.12}$$

In addition, to be able to test the correlation between the algorithm measurements and the ground truth, the coefficient of determination (R^2) and the root mean squared errors (*RMSE*) were calculated.

A linear regression analysis was conducted to explore the relationship between fiber yield and boll number as well as boll volume. In addition, boll position can enable boll spatial density distribution analysis (Figure 5.4). For height (vertical direction) spatial analysis (Figure 5.4a), we divided the space between the ground and the maximum height of the bolls into several slices at consistent intervals. Thereby, the number of bolls in each slice could be calculated, and the distribution histogram could be obtained. For the x-y plane (horizontal direction) analysis (Figure 5.4b), the space was divided into slices along the x axis at consistent intervals, and the bolls located at each slice were calculated.

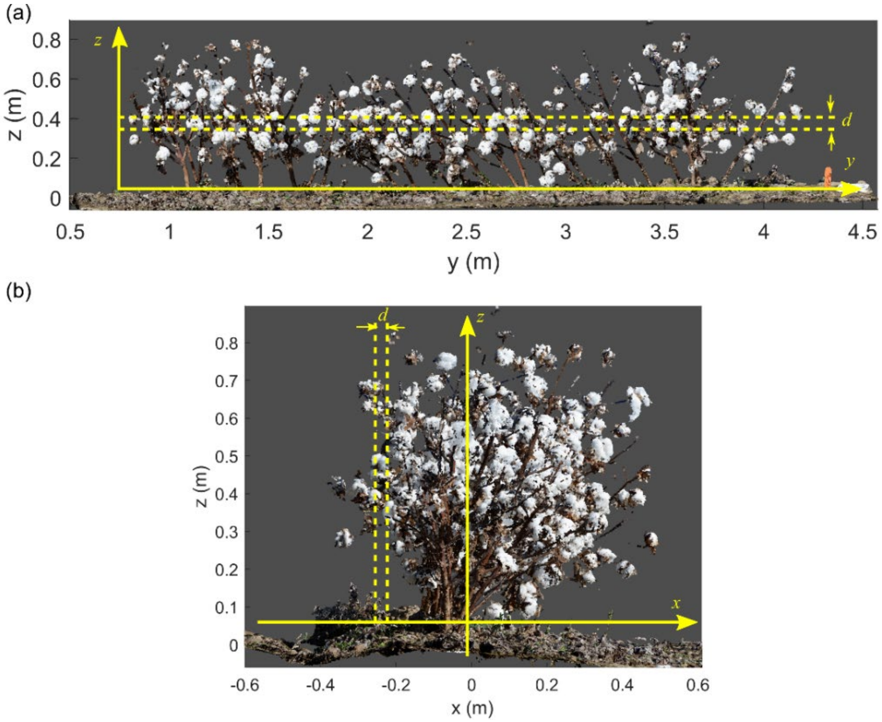

Figure 5.4. Schematic of 3D cotton boll spatial density distribution analysis. (a) z-axis (vertical direction) distribution. (b) x-y plane (horizontal direction) distribution.

5.3 Results

A plot with 312 cotton bolls (Genotype: P011.608.GA2012F2) was selected to demonstrate the 3D boll mapping results (Figure 5.5). This plot was selected because the bolls were dense enough that they had a high possibility of being connected. After pose adjustment, the ground plane was located on the x-y plane with $z = 0$, and the planting line was located at the line $x = 0$. The ground plane was removed for the following processing.

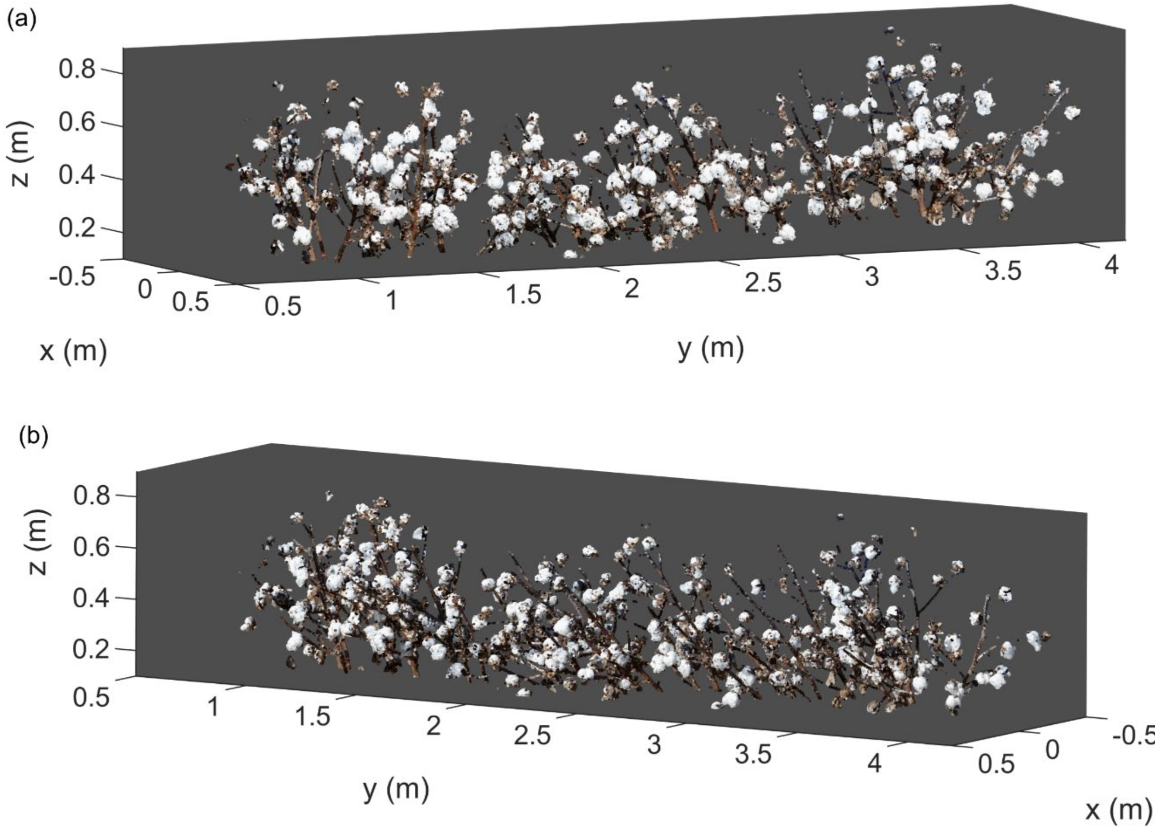

Figure 5.5. Point cloud of a plot after preprocessing (pose adjustment and ground plane removal) from two different perspectives. (a) Point cloud with the viewing angle of azimuth and elevation [120, 10] degree. (b) Point cloud with the viewing angle of azimuth and elevation [60, 10] degree.

5.3.1 Boll point segmentation

Over-segmentations of the point cloud were generated by the VCCS algorithm (Figure 5.6), where each over-segmentation (supervoxel) contained several individual points and was indicated using a color different from surrounding supervoxels. A boll might be divided into several supervoxels, and so were branches. Similar results could be generated using CRGS algorithm.

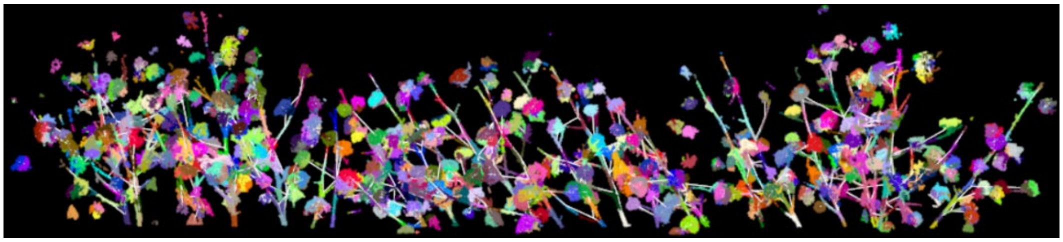

Figure 5.6. Over-segmented regions using VCCS algorithm for a plot.

The optimal parameters C and γ for VCCS-generated region dataset, were 5.28 and 4.60 respectively. The trained SVM classifier achieved classification accuracies of 95.6% and 91.6% in training and validation datasets, respectively. Regarding CRGS-generated region dataset, the optimal parameters C and γ were 1 and 2.30, and the training and validation accuracies were 94.7% and 91.4%, respectively. The results indicated that both classifiers achieved good performance for boll region and branch region classification. Figure 5.7 demonstrated an example of obtained cotton boll points after classification operation using VCCS-generated region dataset. It was observed that almost all the boll points were successfully segmented, and the branches with white color were correctly classified, which was due to the contribution of the region spatial and shape features. While some boll regions were misclassified, it did not cause significant negative effects on boll detection because usually only a small part of a boll was misclassified.

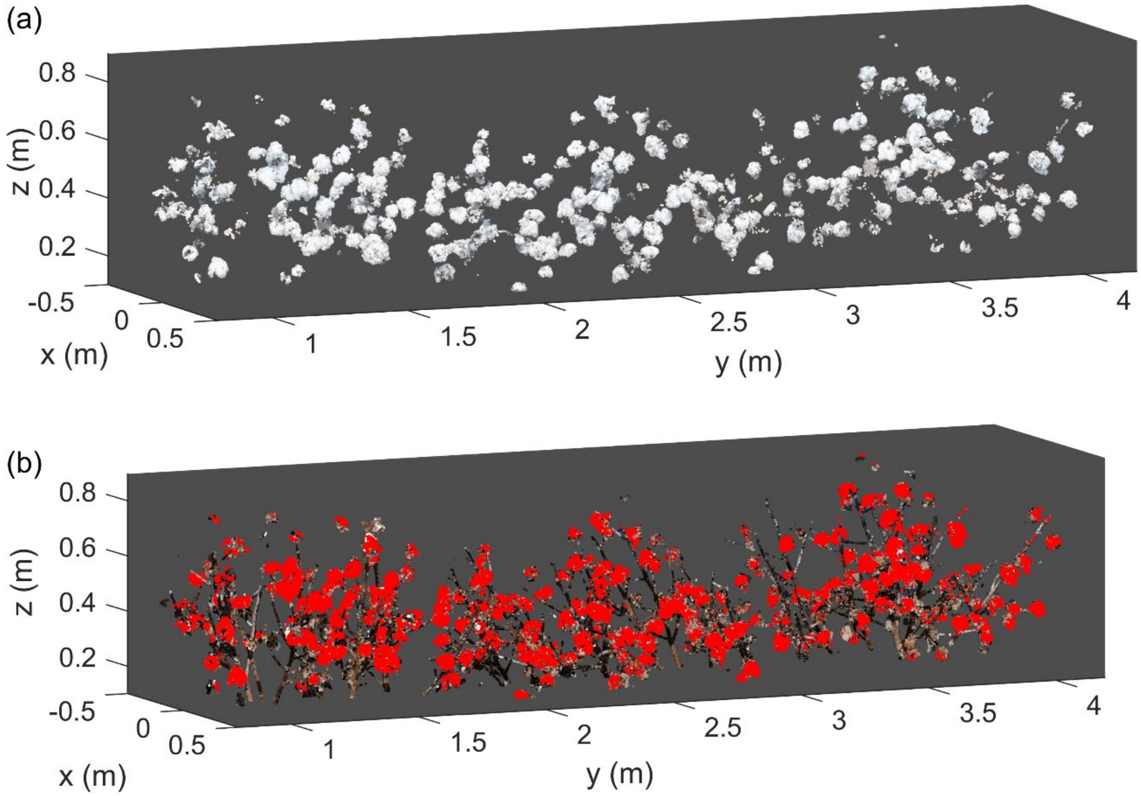

Figure 5.7. A detailed view of boll segmentation for a plot using a classifier trained by a support vector machine. (a) Segmented boll points without branch points. (b) Segmented boll points with branch points. Boll points were indicated using red color and other points using their original color.

5.3.2 3D boll mapping

The boll counting results from the proposed method were precise and highly correlated with manual harvesting results (Figure 5.8). An average accuracy of ~ 90% for boll counts for all 30 plots was achieved, with the best accuracy of ~ 95% (MAPE = 5.08%) and RMSE of 16.87. It was observed that for both boll segmentation methods, the MAPE and RMSE for data collected on November 22, 2017 (Figure 5.8a and b) were better than those for data collected on Dec 14, 2017 (Figure 5.8c and d), suggesting that sampling date affected boll counting performance. The most likely reason was that at the early stage of the harvesting season, cotton bolls retained relatively regular shapes (tight spheres) and have few occlusion issues. However, after prolonged exposure to wind and rain at a later stage of the harvesting season, the cotton fiber would not stay tightly to the burr and became strung out, resulting in cotton bolls that were droopy and have complex shapes and a higher probability to get occluded. However, the R^2 values for the NAM field were better than the ones for the SVT field since the boll number for NAM field was distributed over a large range while it was restricted to a relatively small range for SVT. Each plot in the NAM field was a different genotype with diverse morphology and yield, while the plots in SVT field were commercial cultivars with more homogenous morphology and high yield. For point clouds obtained from each experimental field, similar boll counting performance was obtained using both VCCS- and CRGS-generated region datasets. However, the VCCS algorithm was much faster (~5 times) than the CRGS algorithm. This advantage was mainly attributed to two factors—VCCS applied more efficient data structures such as KD-tree; and an operation merged small regions together for the CRGS method, which was time consuming.

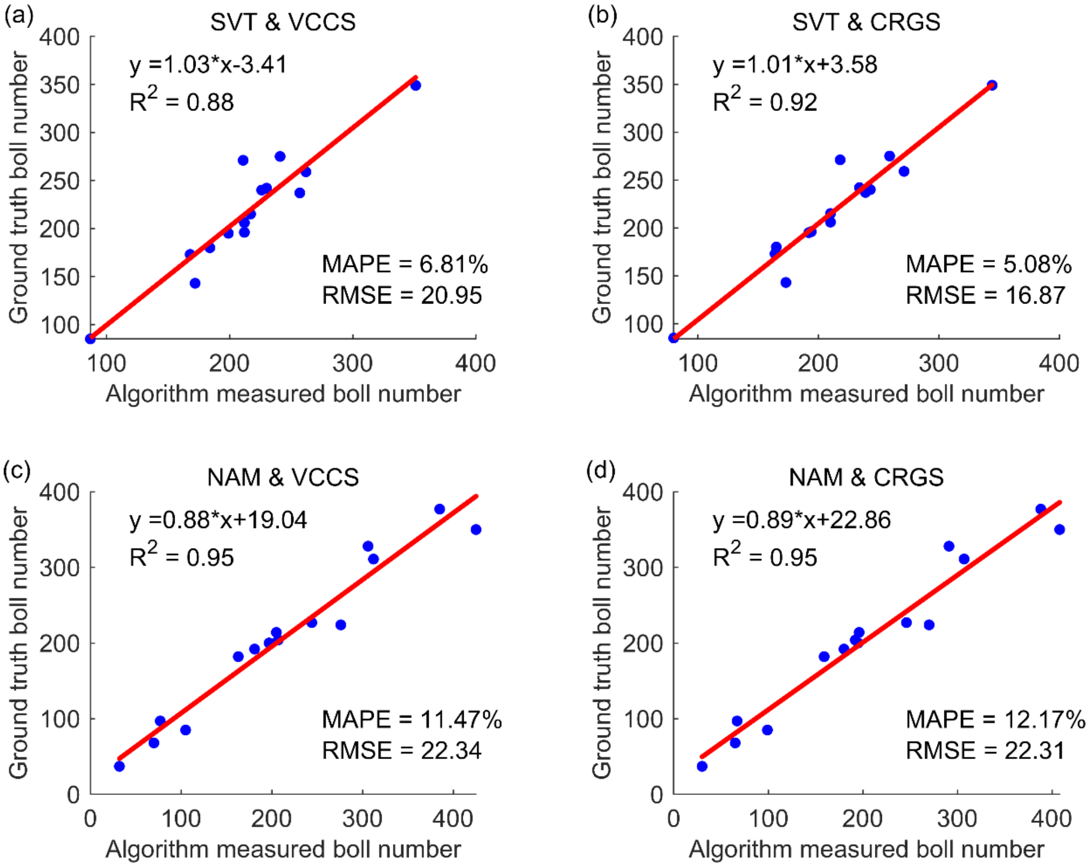

Figure 5.8. Scatter plots of references versus estimated boll numbers. (a) SVT field data with VCCS algorithm. (b) SVT field data with CRGS algorithm. (c) NAM field data with VCCS algorithm. (d) NAM field data with CRGS algorithm.

The error of cotton boll counting (over estimation and under estimation) was mainly attributed to the splitting operation of multi-boll clusters. As the reproductive organ, cotton bolls on a cotton plant reach physiological maturity and open at a wide range of times, since flowering time usually begins about 60 to 70 days after planting and new flowers continue to develop throughout the 4 to 6 weeks of reproductive season, depending on the interaction between cultivar and environmental factors such as temperature and moisture conditions (Sharma et al., 2015). The boll size and shape had a wide variation among plots even grown in the same field. If all bolls were opened while maintaining regular shapes for a plot, the multi-boll cluster splitting method would achieve good counting performance (Figure 5.9a). However, for a plot , if part of bolls, usually located in higher canopy, were not fully opened and had small volumes; while other bolls, usually located at lower canopy, were fully opened and droopy had much larger volume (Figure 5.9b), the calculated average individual boll volume would be similar to these not fully opened bolls. Therefore, the cluster splitting operation would generate a number which is much greater than the ground truth number for a multi-boll cluster. The highest over estimation plot in our dataset was demonstrated in Figure 5.9b and the zoomed-in part showed that a multi-boll cluster was over divided. If all cotton bolls were fully opened, therefore they had large size, resulting in a higher possibility to create multi-boll clusters (Figure 9c). Overall, the calculated average individual boll volume would be large, resulting in that less number (under estimation) would be obtained from the splitting operation. Because some two-boll clusters had similar volume to the calculated average boll volume as demonstrated in the zoomed-in part in Figure 5.9c. Another possible situation was that the identified individual bolls during the cluster splitting operation would be clusters consisting of two or more bolls, therefore, the under estimation would happen. Figure 5.9c demonstrated the plot with the highest under estimation.

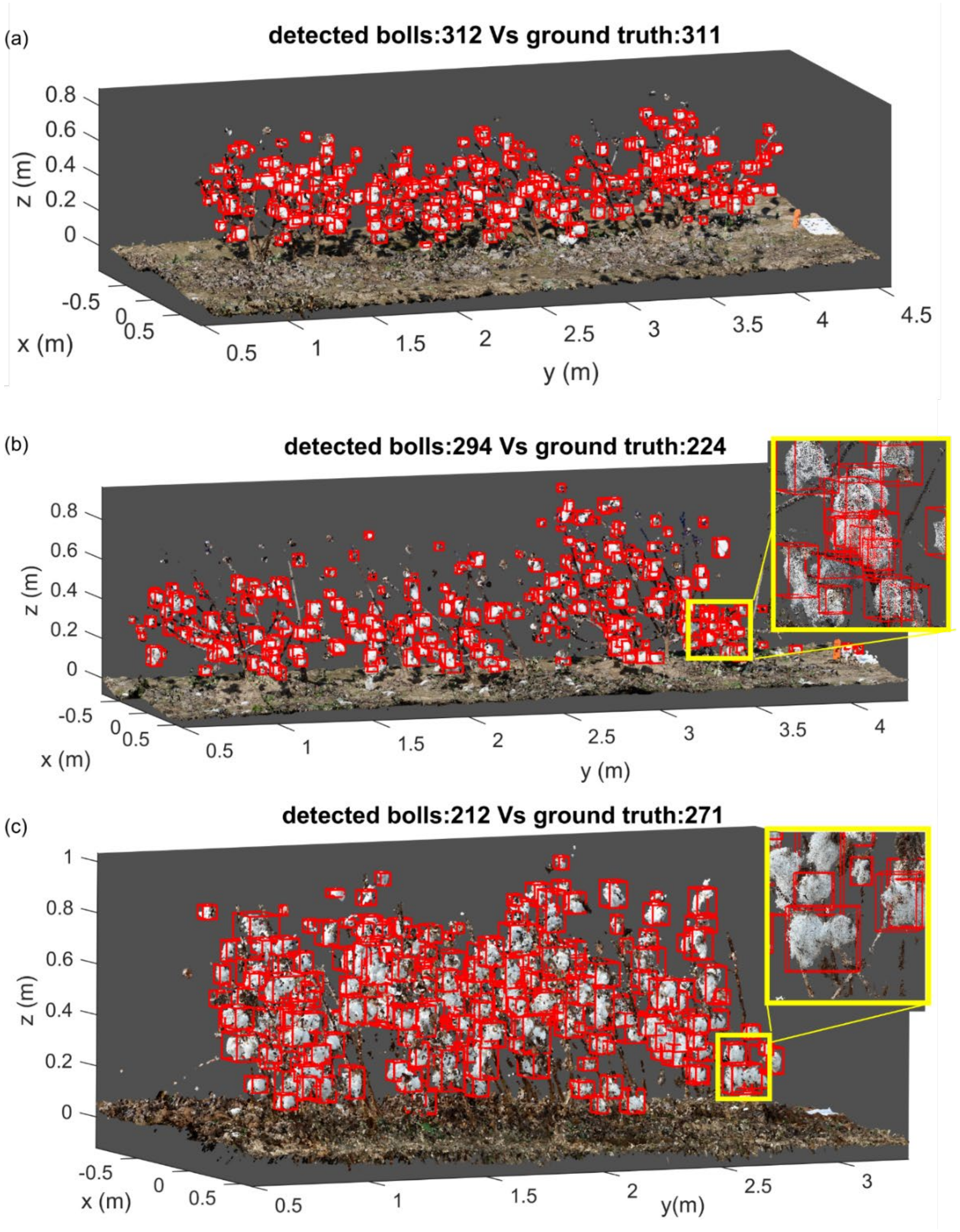

Figure 5.9. Representative results of 3D boll counting, each boll was indicated using a red bounding box. (a) The plot achieved the best boll counting result. Cotton bolls in this plot were fully opened while maintaining regular shapes. (b) The plot had the highest over estimation of boll numbers. Boll size had a wide variation in this plot, bolls at the high plant parts were not fully opened, resulting in small volume, while bolls at the bottom plant parts were fully opened, resulting in much larger volume. (c) The plot had the highest under estimation of boll numbers. In this plot all bolls were fully opened, resulting in a higher possibility to generate more multi-clusters.

5.3.3 Correlation with yield

Overall, boll number and boll volume presented good correlation with fiber yield for the SVT and NAM fields ($R^2 > 0.87$ for boll number, $R^2 > 0.66$ for boll volume) (Table 5.2). Boll number gave better correlation than boll volume with fiber yield for both fields, resulting in better *MAPE* and *RMSE*. This was not surprising since as mentioned above, boll size could vary substantially and were affected by the length of time they were exposed to weather elements. Cotton bolls developed from flowers which opened early in the growing season, often located in the lower canopy, tend to mature and open at an earlier time. These bolls have higher likelihood to become droopy, resulting in more varied sizes at maturity. Similar to the explanation for boll number counting performance analysis, the timing of data collection, which was related to the maturity levels of cotton bolls, was a factor affecting yield correlations. Given that data collection in the SVT field was performed in a more favorable time window (i.e., plants were less weatherized) than in the NAM field, a better performance was obtained in the SVT field than in the NAM field for boll numbers and volume measurements.

Table 5.2. Comparison of fiber yield correlation analysis with boll number and boll volume.

Attributes	**Methods**	**SVT**			**NAM**		
		R^2	**MAPE(%)**	**RMSE (g)**	**R^2**	**MAPE(%)**	**RMSE (g)**
Boll number	VCCS	0.91	7.99	77.09	0.90	19.29	143.84
	CRGS	0.87	8.15	93.57	0.90	17.75	141.01
Boll volume	VCCS	0.66	17.10	152.05	0.84	37.86	179.94
	CRGS	0.66	17.59	151.70	0.85	34.36	173.25

5.3.4 Spatial density distribution analysis

Boll distribution, a phenotypic trait which was highly useful for yield distribution analysis, could also be analyzed using such techniques. For a typical cotton plant, the first position bolls between nodes 7 to 20 generally contributed the majority of fiber yield (Ritchie et al., 2007). As an example, the bolls detected from a plot in Fig 9a, which were represented using local mean coordinates in Figure 5.10a, were distributed within a bounding box with a size of 0.83 m, 3.35 m, 0.78 m along x, y, z direction, respectively. The bolls located at the longest distance from the planting line ($x = 0$) were 0.37 m and 0.48 m for the left and right sides, respectively (Figure 5.10b). The bolls were not evenly distributed on the two sides of the plots: around 70% of the bolls were located to the right side of the plot (Figure 5.10c). This was mainly caused by hurricane Irma, which impacted on September 11th, 2017, resulting in all the plants in the plots becoming tilted. 91.4% of bolls were located within a distance of 0.3 m from the planting line. In the vertical direction, the highest and lowest bolls were located at heights of 0.78 m and 0.11 m, respectively, and the average height of all bolls' location was 0.42 m (Figure 5.10d). Around 85% of the bolls were located within a height range of [0.2, 0.6] m (Figure 5.10e).

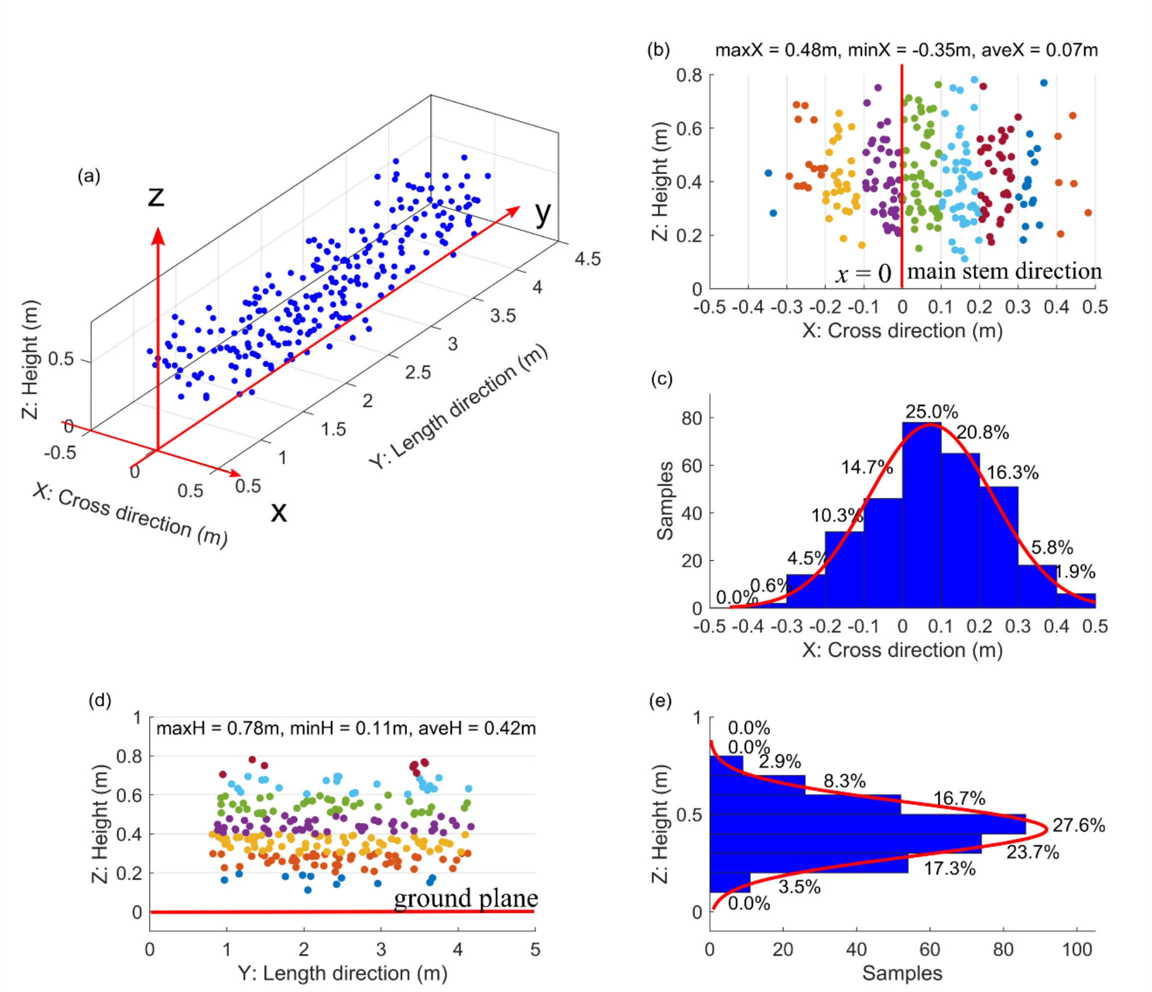

Figure 5.10. Cotton boll 3D spatial density distribution analysis. (a) Localization of all detected bolls, each represented using a blue point. (b) Boll distribution on x-z plane. (c) Histogram of boll localization on x-z plane. (d) Boll distribution on y-z plane. (e) Histogram of boll localization on y-z plane.

5.4 Discussion

We demonstrated that good quality colored 3D point clouds can be reconstructed from multi-view images collected using a ground-based mobile platform under field conditions. This provides the potential to extract plant organ-level phenotypes from the point cloud, which is an advantage compared to UAV-based 3D model platforms (Colomina and Molina, 2014; Pajares, 2015; Sankaran et al., 2015). A multi-view scanning strategy greatly reduces occlusion, which significantly influences plant phenotyping, especially under field conditions (Vazquez-Arellano et al., 2016). The tractor platform could be replaced by a motorized, narrow-wheeled and lightweight robot to further promote easier transportation and operation of the platform, and such a unit would have lower soil disturbance and compaction than the tractor (Thompson et al., 2018).

Illumination conditions play an important role in the quality of raw images. Noon is preferred for field plant scanning with this platform. At midday, there is peak sunlight, which allows configuration of the camera with a high shutter speed that is helpful to reduce blurry images. Another advantage is that the shadow effect can be reduced since the sunlight is almost perpendicular to the ground plane. Wind is another factor influencing image quality and breezy conditions could be detrimental for 3D point cloud reconstruction. One potential solution to resolve these two problems would be to add an enclosure with artificial lights (Andrade-Sanchez et al., 2013; Barker III et al., 2016). The enclosure itself could block winds, and the artificial lights could improve consistency of light condition and reduce shadows.

Current 3D point cloud reconstruction and data analyses were performed off-line. Around three to five hours were needed for a plot, depending on how many images used, based on a desktop equipped with 16GB RAM memory and a 4GB memory GPU card with the computational capability of 5.0. Data acquisition and processing could become online if 3D point clouds were acquired by using high resolution 3D LiDAR, although the cost of instrumentation would increase significantly (Guo et al., 2018b; Kirchgessner et al., 2017).

The boll counting accuracy of the method outperformed the studies of fruit counting using 2D image based methods (Bargoti and Underwood, 2017; Malik et al., 2016; Wang et al., 2016a), because more information such as actual size and depth was included for 3D point clouds, and the occlusion effect was much reduced due to multi-view images. In addition, rich features such as spatial and shape features, which are not affected by varied illumination conditions, can be extracted from over-segmented regions. This greatly improved detection performance (Malambo et al., 2019; Sun et al., 2018b). Although these hand-designed features performed well in this study, performance could be further improved if more advanced or complex features from 3D point clouds can be extracted. In addition, the performance of the classification model could be improved by using more specific machine learning methods for training. For example, the algorithm high-order Markov random fields was reported to achieve better performance than standard SVM for the application of point cloud classification (Munoz, 2013), because it can efficiently model the interaction of a group of points. 3D deep learning is another potential method to be explored in the future, which can automatically extract point cloud features from low-level information such as edges and corners to high-level semantic information by a hierarchical multi-stage structure, enabling end-to-end 'boll mapping' (Qi et al., 2017; Zhou and Tuzel, 2017). Compared to 2D image-based methods, in addition to improving boll counting performance, 3D model-based methods permit more phenotypic traits such as boll volume and boll spatial density distribution to be derived effectively and efficiently. Using such a method, it could be feasible to delineate cotton boll locations on each branch if a cotton plant branch pattern is obtained (Jin et al., 2018). Identification of each individual cotton boll and its location would be highly useful to plant breeding and cotton-picking robot in the future.

This study provides a new method to explore and understand plant growth using 3D mapping *in situ*, which is a grand challenge in plant biology. On one hand, the extracted traits such as the boll distribution on a cotton plant would be helpful for manipulating plant architecture, which are increasingly being emphasized in crop yield improvement (Mathan et al., 2016). If gin turnout data were available, cotton yield could be more accurately estimated by associating with number of bolls and boll size obtained using the proposed method (Sharma et al., 2015). Therefore, it would not be necessary for breeders to harvest cotton in order to determine which genotypes will produce the highest yield. On the other hand, 3D mapping *in situ* provides opportunities to extract more features such as plant nodes and branch architecture from point clouds (Conn et al., 2017).

5.5 Conclusions

A multi-view, camera-based system was developed to acquire high quality colored 3D point clouds of cotton plants *in situ*. High accuracy boll segmentation and counting was achieved based on 3D point cloud segmentation and clustering algorithms. As a result, reliable 3D boll mapping and counting was obtained. Future work will focus on improving the throughput of data acquisition and processing, as well as exploring 3D deep learning for boll detection under field conditions.

CHAPTER 6

HIGH RESOLUTION 3D TERRESTRIAL LIDAR FOR PLANT MAIN STALK AND NODE DETECTION[5]

---

[5] Sun, S., Li, C., Paterson, Chee, P., A., Adhikari, J., Robertson, J., Meng, C., Ma, P., To be submitted to *IEEE Transactions on Geoscience Remote Sensing*

Abstract

Dense three-dimensional point clouds provide opportunities to retrieve detailed characteristics of plant organ-level phenotypic traits, which are helpful to better understand plant function and to contribute to the development of new plant breeding approaches. In this study, a high-resolution LiDAR was used to acquire point clouds of plants under field conditions, and a data processing pipeline was developed to retrieve three plant phenotypic traits including node position, plant height and height-to-node ratio. The proposed method consisted of three main steps: first, extract skeletons from original point clouds using a Laplacian-based contraction algorithm; second, identify plant main stalks by converting the skeleton points to minimum spanning trees; and third, segment individual branches by combining 'pruning' with clustering operations. Then, a node was detected by finding the intersection between the main stalk and a branch; plant height was calculated by accumulating the distance between two adjacent points from the lowest to the highest point of the main stalk, and height-to-node ratio was retrieved by dividing a plant height by the node number. Experimental results based on 26 plants showed that the R^2, mean absolute percentage error, and root mean square error were 0.88, 3.23% and 0.7 for node number counting, 0.93, 3.89%, and 4.7 cm for plant height measurements, and 0.72, 6.24% and 0.4 cm/node for height-to-node ratio, respectively. More traits such as branch angle and canopy size can be extracted from the point clouds. Three-dimensional based high throughput phenotyping may expedite breeding technologies to increase crop production.

6.1. Introduction

Crop improvement needs to increase at a faster pace due to an growing global population, climate change, and the limitations of natural resources such as arable land and water (Gerland et al., 2014; Tilman et al., 2011). To address this tremendous challenge, it is urgent to develop new technologies to accelerate plant breeding (Pieruschka and Schurr, 2019; Tester and Langridge, 2010). Plant phenotyping measures and describes a diversity of phenotypic traits from cell to organ to the canopy and assesses plant development and performance (Dhondt et al., 2013; Goggin et al., 2015; Ninomiya et al., 2019), which plays a vital role in accelerating the selection of the next generation of crops to meet specific breeding and research goals and has become a rapidly-evolving area of focus in agricultural applications (Czedik-Eysenberg et al., 2018; Granier and Vile, 2014). However, high throughput phenotyping (HTP) technologies, especially noninvasive phenotyping in field conditions, remains a major technical bottleneck limiting crop improvement (Campbell et al., 2018; Furbank and Tester, 2011; Großkinsky et al., 2015).

During the past decade, 2D image-based methods are widely used in the application of phenotypic trait measurements, including crop growth monitoring (Li et al., 2014), disease detection (Ghosal et al., 2018), and canopy size (Wang et al., 2018). The emergence of deep learning technology (LeCun et al., 2015) greatly promotes the development of plant phenotyping, which offers the potential to provide generic solutions for plant image analysis (Singh et al., 2018; Tardieu et al., 2017). In order to better understand plant function, efforts have been conducted to explore new imaging technologies to describe the characteristics of phenotypic traits at the organ level, such as leaf and stalk (Yin et al., 2018), flower (Xu et al., 2017) and fruit (Miller et al., 2017), and root analysis (Bao et al., 2018). One major challenge for image-based methods is the inherent occlusion, which is especially difficult to deal with under field conditions (Liu et al., 2019). In addition, image quality, which plays a vital role in trait detection performance, is hard to control under varied illumination conditions, thereby limiting its applications under field conditions (Jin et al., 2018).

Much effort has been made to explore three-dimensional (3D) methods for high throughput plant phenotyping (Vazquez-Arellano et al., 2016), and currently 3D-based methods are receiving increasing attention. Because on one hand, new sensor technologies and more powerful computers make dense point cloud collection and processing easier (Guo et al., 2018b; Paulus et al., 2014b); on the other hand, 3D point cloud data provide depth information, which is highly useful for addressing occlusion, from which a wider variety of phenotypic traits can be retrieved. In addition, such information can improve the chance for deriving new traits from the same models at a later time, which is more difficult in image-based approaches since the required features may be invisible, or the actual size may be unobtainable from unrecorded calibration information (Gibbs et al., 2017). LiDAR is one of the most commonly used sensors for field-based phenotyping, which uses its own light source for distance measurement, greatly reducing the impact on data quality caused by environmental illumination (Lin, 2015). 2D line scan LiDAR combined with GPS were often used to build plant 3D models under field conditions during the past decade; plot/plant level traits such as canopy size and plant volume were derived from the reconstructed point clouds (Auat Cheein et al., 2015; Méndez et al., 2016). However, due to the limited resolution, it is hard to retrieve plant organ level traits such as leaf, bloom, and fruit. The emergence of high-resolution LiDAR provides opportunities to obtain highly dense point clouds. Several studies have been conducted to apply a high-resolution LiDAR to measure plant organ traits, and custom algorithms were designed based on the characterization of specific traits, such as sorghum panicle detection

(Malambo et al., 2019), maize-stem size estimation (Jin et al., 2018), and grape leaf and stem segmentation (Paulus et al., 2013). Stereo vision and structure from motion (SfM) based methods have been used to reconstruct dense point clouds from images (Isokane et al., 2018; McCormick et al., 2016). These methods are able to obtain good quality point clouds under well-controlled environment conditions; however, image limitations with regard to varied illumination conditions still exist.

This study focused on cotton plant architecture phenotypic traits measurement using a high-precision LiDAR under field conditions. Cotton (*Gossypium spp.*) is among the most economically important fiber crops, accounting for almost 80% of the total natural fiber production throughout the world (Fangueiro and Rana, 2016). Phenotypic data on cotton plant nodes are useful to breeders and growers alike. For example, node number and internode distance are closely related to fiber yield and are often used to monitor plant growth (McCarthy et al., 2010). Height-to-node ratio (HNR) is very sensitive to temperature (Oosterhuis and Kerby, 2008) and the traditional manual measurement of nodes can be time consuming and labor intensive. McCarthy et al. (2009) developed a vision system to detect cotton plant nodes from RGB images, in which nodes were identified by extracting line features of main stems and branches from acquired images. Although the absolute error of internode distance measurement for 95 detected nodes were small (6.1 mm), only around 11% (95 out of 840) nodes were detected. Visual occlusion was the main reason for nodes going undetected. 3D-based cotton plant node detection remains unexplored in the phenotyping literature.

The overall goal of this study was to demonstrate the feasibility of applying LiDAR and the proposed 3D data processing pipeline for field-based cotton plant organ trait detection. The objectives were to: (1) collect dense point clouds for individual cotton plants under field conditions; (2) derive plant skeletons from original point clouds using a Laplacian-based algorithm; (3) develop a graph-based algorithm to detect plant main stalks and a method for individual branch segmentation by combing a 'pruning' operation and a density-based clustering method; (4) extract plant phenotypic traits including nodes, height and HNR and validate the performance based on ground truth data.

6.2. Material and Methods

6.2.1. Plant scanning with LiDAR

The experimental field was located at Iron Horse Farm in Greene County, GA, USA. There was a total of 132 single cotton plants, 12 rows by 11 columns, with the plant inter-distance of approximate 152.4 cm (Figure 6.1a). A 3D terrestrial LiDAR sensor (FARO laser scanner focus S70, FARO Technologies, USA) (Figure 6.1b) was used to scan plants for point cloud data acquisition. The sensor can conduct a 360° scan on the horizontal plane, so each plant could be scanned from four perspectives, while each scan could cover four plants (Figure 6.1a). The scans were registered as point cloud datasets by the software FARO SCENE, which was included with the sensor (Figure 6.1c). Data collection was conducted on Dec 11 and 18, 2018, respectively. Fifteen plants were scanned on each day, resulting in a total of 30 point cloud datasets.

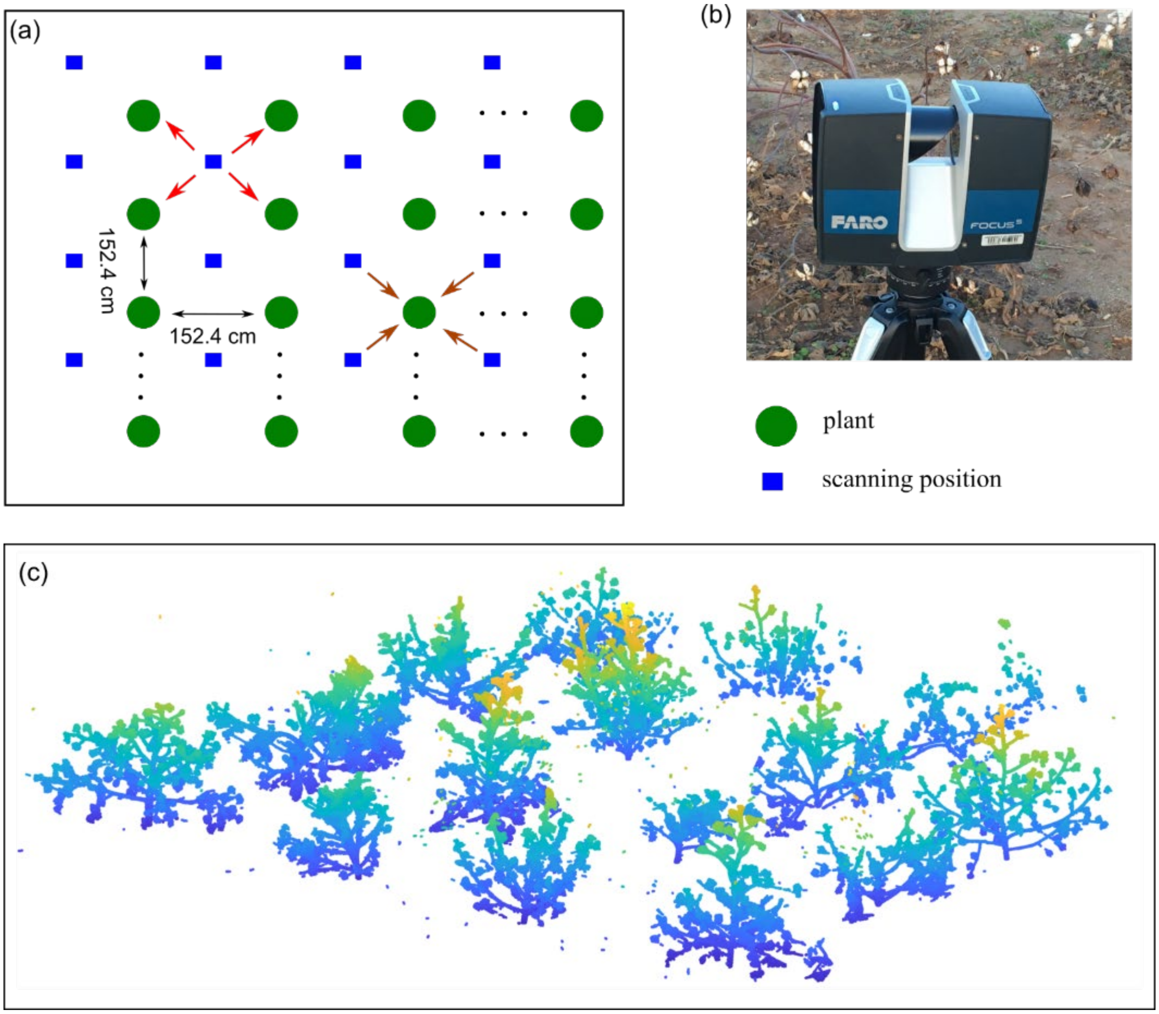

Figure 6.1. Experimental field and scanned point cloud data using a terrestrial LiDAR. (a) Schematic of plant layout and scanning positions. (b) The LiDAR sensor used in this study. (c) Partial point clouds acquired in the experimental field.

Highly accurate point clouds were obtained with the LiDAR using the proposed scanning strategy under field conditions (Figure 6.2), from which plant organs such as branches and cotton bolls could be observed. The plants had wide variation in appearance due to the influence of environmental and genotypic factors. According to the shape of the plant architecture, the plants were divided into three categories in this study. Representative plant shapes for each category are demonstrated in Figure 6.2. Eighteen of them had canopy shapes with upright main stalks (Figure 6.2a); the main stalks of eight plants were moderately tilted (Figure 6.2b), while the main stalks of the last four plants were bent in several places such that some branches touched the ground (Figure 6.2c). The highest point of a plant was located at the main stalk in the first two categories, while it was located at one of the branches instead of at the main stalk for plants in third category. In this study, we processed data only from plants in the first two categories (Figure 6.2a and b).

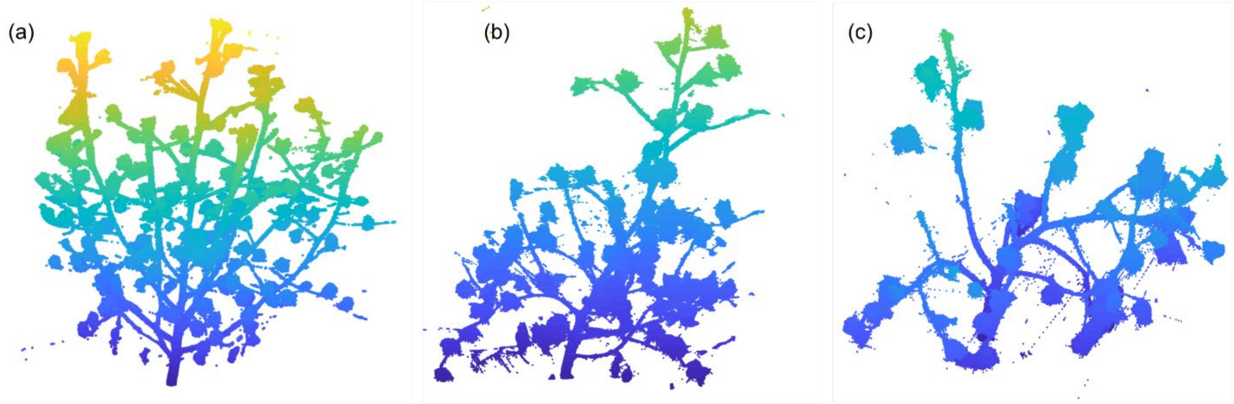

Figure 6.2. Three categories of representative plants with different architecture patterns. (a) plant with an upright main stalk. (b) and (c) plants with tilted main stalks. The highest point of (b) is located in the main stalk while the highest point of (c) is located at a branch instead of at the main stalk.

6.2.2. Identification of the main stalk and individual branches

Identification of the main stalk and individual branches is a prerequisite for many plant organ level phenotypic trait measurements. For example, a plant node is the part of the main stalk where branches start to grow, which can be detected by identifying the intersection between the main stalk and a branch. The method developed in this study consisted of three steps: 3D skeleton extraction, main stalk detection, and identification of individual branches. Point cloud skeletonization is a thinning operation in which point cloud regions are reduced to lines that approximate their center lines. The purpose of skeletonization operation is to generate a thin centered structure which maintains the topological and geometrical characterizations of the original point cloud data while greatly reducing data volume so that further analysis is performed.

6.2.2.1. 3D skeleton extraction

A Laplacian-based contraction method was used to extract the plant curve skeleton from the point clouds because it is resistant to noise and can handle a moderate amount of missing data (Cao et al., 2010). Only point location information was used for the skeletonization operation. Two steps are involved in this method, including geometric contraction and topological thinning. A point cloud could be contracted by iteratively solving the linear system (eq (6.1)).

$$\begin{bmatrix} W_L^t L^t \\ W_H^t \end{bmatrix} P^{t+1} = \begin{bmatrix} 0 \\ W_H^t P^t \end{bmatrix} \tag{6.1}$$

where P^t was the point cloud for the t^{th} contraction operation, P^{t+1} was the corresponding point cloud after the contraction operation, and P^0 was the original point cloud with dimension of $n \times 3$, n was the number of points; L^t was a $n \times n$ Laplacian matrix which was constructed via 1-ring of a Delaunary triangulation; W_L^t and W_H^t were the $n \times n$ diagonal weight matrices balancing the contraction and attraction constraints; **0** was a $n \times n$ zero matrix. $W_{L,i}^{t+1}$ and $W_{H,i}^{t+1}$ are updated using $W_{L,i}^{t+1} = S_L W_{L,i}^t$ and $W_{H,i}^{t+1} = W_{H,i}^0 \sqrt{S_i^0 / S_i^t}$, respectively, where S_L was a constant coefficient, $S_L = 3$ following the suggestion in (Cao et al., 2010). $W_{L,i}^0 = 1 / S_i^0$, $W_{H,i}^0 = 1$, and S_i^0 is the mean neighbor extent of point i in the point cloud. The iteration of the contraction operation stopped when convergence achieved a steady state. The final contracted point cloud was denoted by C.

Regarding topological thinning operation, firstly, the contracted point cloud C was sampled using farthest-point sampling with a resolution of ε. After that, we obtained the skeleton by imposing an initial connectivity and then by collapsing unnecessary edges. The parameter ε was selected according to the size of interested traits. $\varepsilon = 5$ mm was used in this study since this value was so small that the extracted skeleton could distinguish nodes based on the observation of cotton plant internode distance. A down-sampling operation was conducted in order to improve computational efficiency before skeleton extraction operation.

It should be noted on the difference between contraction and down-stamping. Contraction is an operation to shrink the shape of point cloud data. It does not reduce the point numbers, while maintaining the key topological and geometrical features. Down-sampling is an operation to select part of the points from the original point clouds based on predefined rules. It reduces the point numbers but maintain the original shape. Point cloud skeletonization is a thinning operation in which point cloud regions are reduced to lines that approximate their center lines, which greatly reduces point numbers. In this study, down-sampling is firstly applied to reduce point numbers in order to improve computation efficiency and then skeletons were extracted from the point clouds.

6.2.2.2. Main stalk detection

A graph-based method was developed for main stalk detection, which involved two steps: (1) initial main stalk points detection and (2) main stalk points refinement. The skeleton point set, denoted by $Pt = \{p_1, p_2, \cdots, p_k\}$, was divided into two sub-point sets: S and B. S was the main stalk point set, and B was a point set including all other points, $Pt = S \cup \mathrm{B}, \mathrm{S} \cap \mathrm{B} = \emptyset$.

The initial main stalk points were detected by converting the skeleton points (Figure 6.3a) to a graph (Figure 6.3b) based on the 3D Euclidean distance between two points p_i and p_j (eq (6.2)). If the distance was less than a threshold λ which could be selected based on the skeleton resolution, the two points were connected, such as point 1 and 2 in Figure 6.3a; otherwise, they were disconnected, such as point 3 and 11. Each point in the generated graph was taken as a vertex and connected to its neighboring points with edges (Figure 6.3b). The neighboring points are all those points whose 3D Euclidean distance to the given point is less than the predefined threshold λ. Three sub-graphs were included in Figure 6.3b: sub-graph 1(sub-graph 1 = {1, 2, 3, 4, 5, 6, 7, 8, 9, 10}) contained most parts of the plant, resulting in the most number of points; sub-graph 2 (sub-graph 2 = {11, 12}) was created by part of a branch which did not connect to the main stalk because the minimum distance between point 11 and the main stalk points was greater than λ; sub-graph 3 (sub-graph 3 = {13, 14}) was created by materials laying on the ground, such as weeds or parts of the plant branches that were touching the ground. The main stalk points should be included in the sub-graph containing the most points (sub-graph 1 in Figure 6.3b), which was selected for further processing. Then the selected sub-graph was converted to a minimum spanning tree (MST) in order to cut circles in the graph (Figure 6.3c), in which the lowest point (point 1) was selected, and starting from which, the standard shortest path search method was used to derive all paths in the MST. The path with the highest terminal point (point 6) was selected as the main stalk.

$$d(i,j)=\sqrt{\left(x_i-x_j\right)^2+\left(y_i-y_j\right)^2+\left(z_i-z_j\right)^2} \tag{6.2}$$

For the ideal situation in which there are no gaps (the distance between two adjacent points is equal to the predefined skeleton resolution ε) in the skeleton, the parameter λ could be selected from the range (ε, 2ε) such that all main stalk points could be detected. However, gaps may exist in the skeleton because of incomplete point clouds although multi-view scanning was used for data collection in this study. Therefore, λ should be greater than 2ε in order to cover gaps in the initial main stalk detection step. However, the problem was that only some of the main stalk points were detected.

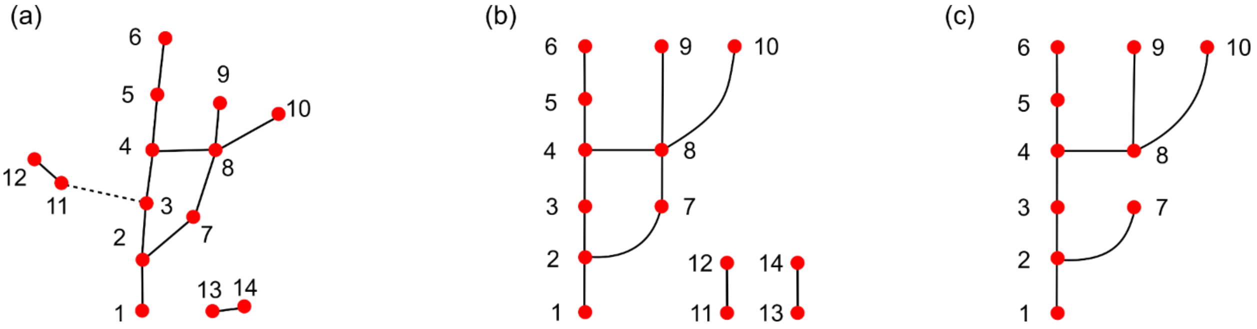

Figure 6.3. Schematic of the algorithm for main stalk detection. (a) Example of the extracted skeleton points of a plant. The solid line means the two points are connected since the distance between them is so small (less a predefined threshold); the dashed line means the two points are not connected due to the large distance. (b) Graph converted from (a), in which three sub-graphs are included. Sub-graph 1 = {1, 2, 3, 4, 5, 6, 7, 8, 9, 10}, sub-graph 2 = {11, 12}, and sub-graph 3 = {13, 14}. (c) Minimum spanning tree converted from sub-graph 1 in (b), the lowest point (point 1) is selected, and starting from which, four paths are detected, they are path 1 = {1, 2, 3, 4, 5, 6}, path 2 = {1, 2, 7}, path 3 = {1, 2, 3, 4, 8, 9}, and path 4 = {1, 2, 3, 4, 8, 10}. path 1 is selected as the main stalk because it contains the highest terminal point (point 6).

The aim of the refinement operation was to detect these missed main stalk points according to the trajectory of pre-detected main stalk points. The method relied on the assumption that the main stalk within a short distance scale (λ) was a straight line. First, a line was formed between two adjacent pre-detected main stalk points, and the missed points located between the two pre-detected points should be very close to the line. Then, the distance between a point and the line was calculated. In this study, a value of 3 mm was used as a threshold. If the distance between a point and the line was less than 3mm, the point was considered to be a main stalk point and added to the main stalk point set S.

6.2.2.3. Identification of individual branches

A ‘pruning’ operation was conducted before identifying each branch because cotton plant branches have complex structures that are long and dense, making it very likely that a branch crosses or is physically connected to other branches. The ‘pruning’ operation was designed to cut parts of branches which were far away from the main stalk. First, circles were set with the same radius *r* along the main stalk starting from the lowest point in the crown to the highest point (Figure 6.4a); second, points outside of the circles were removed. Thus, a short part of each branch close to the main stalk was kept, resulting in a simpler branch structure (Figure 6.4b). After that, 3D density-based spatial clustering of applications with noise (DBSCAN) was applied on the remaining branch points, from which the output clusters were assumed to be individual branches.

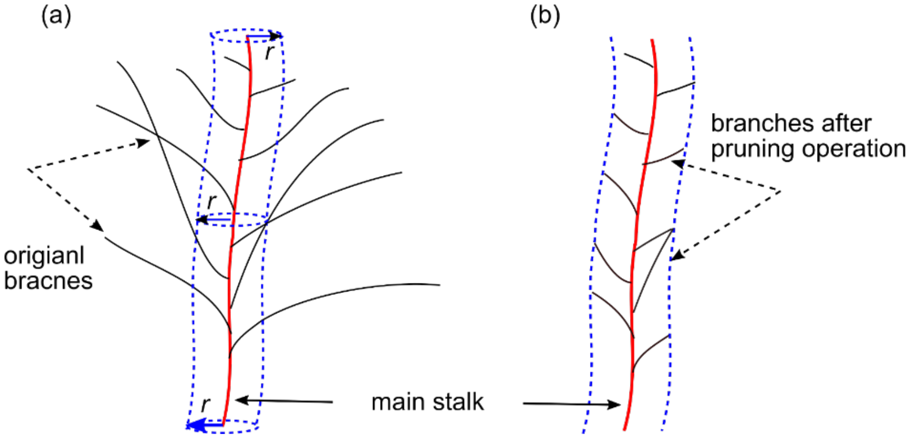

Figure 6.4. Schematic of branch pruning operation. (a) circles were set with the same radius *r* along the main stalk starting from the lowest point in the crown to the highest point. (b) Branches after pruning operation.

6.2.3. Plant architecture traits measurements and accuracy validation

The identified main stalk and branches were used to extract three plant architecture traits including plant nodes, plant height, and HNR.

A node can be detected by identifying the intersection between the main stalk and a branch as described in section 6.2.1. For a branch cluster, denoted by $b = \{b_1, b_2, \cdots, b_n\}$, the highest and lowest points were selected, generating a distance range [*lo*, *hi*]; *lo* and *hi* were the values on the z axis for the lowest and highest points, respectively. The points in the main stalk point set *S*, which were located in the range [lo-δ, hi+δ], were selected and denoted by s (Figure 6.5a), $s = \{s_1, s_2, \cdots, s_m\}$. Then, 3D Euclidean distances between points in b and s were calculated, generating a distance matrix table (Table 6.1). s_{iz} was the value on the z axis for stalk point s_i; $d(s_i, b_j)$ denoted the distance between point s_i and b_j; d_{si} was the minimum distance between point s_i and points in the branch cluster b. An example of visualization for Table 6.1 was shown in Figure 6.5b, in which black dots were the distance point pairs (s_{iz}, $d(s_i, b_j)$) and the blue line consisted of point pairs (s_{iz}, d_{si}) where d_{si} is the minimum distance between s_i *and* b_j. Local minimum peak points of the blue line were then detected, denoted by $N_i = (s_{Ni}, d_{Ni})$. If the vertical axis value d_{Ni} was small enough ($d_{Ni} < \tau_1$) (Figure 6.5b), it indicated that there was a node in s, and the value of the node on z-axis was s_{Ni}. Accordingly, the corresponding node could be identified in s.

The parameter δ was a small positive value, such that, on one hand, only part of the main stalk points were selected for each branch cluster, which was helpful to reduce computation time; on the other hand, it provided room to adjust the position of detected nodes. Detailed description about it would be presented in the example demonstrated in Figure 6.5c and d. The value of the parameter δ was flexible: a value greater than 1 cm could be selected, and $\delta = 2$ cm was used in this study. The parameter τ_1 was used to check whether there was a gap between the main stalk and a branch. Since skeleton resolution was 5 mm, $\tau_1 = 1$ cm was used in this study.

For the situation demonstrated in Figure 6.5c, a gap existed between the main stalk and a branch, i.e., the vertical axis value of the peak point was greater than τ_1 (Figure 6.5d). A pseudo node could be found in the corresponding point set s using the method described for the situation shown in Figure 6.5a and b, However, the actual node should be located below the pseudo node. As shown in Figure 6.5c, the actual node location was estimated by selecting a point located two points below the pseudo node in s.

For the situation two or more peak points were detected (Figure 6.5e and f), a *k*-means clustering method with $k = 2$ was applied to reduce the number of peak points to two. $k = 2$ was used because based on observation, misclustering of 3D DBSCAN happened mostly with two close branches. Then, for each peak point, the method described for the situations in Figure 6.5a and c was used to identify the node position in *s*. If the vertical axis value of a peak point was greater than $\tau_2 = 3$ cm, the point would not be further analyzed because it was very likely caused by the noise.

Table 6.1. Distance matrix between the main stalk and a branch cluster

	b_1	b_2	$\cdots$	b_n	$min(d(s_i, b_j))$
s_{1z}	$d(s_1, b_1)$	$d(s_1, b_2)$	$\cdots$	$d(s_1, bn)$	d_{s1}
s_{2z}	$d(s_2, b_1)$	$d(s_2, b_2)$	$\cdots$	$d(s_2, b_n)$	d_{s2}
$\vdots$	$\vdots$	$\vdots$	$\cdots$	$\vdots$	$\vdots$
s_{mz}	$d(s_m, b_1)$	$d(s_m, b_2)$	$\cdots$	$d(\mathrm{s}_m, b_n)$	d_{sm}

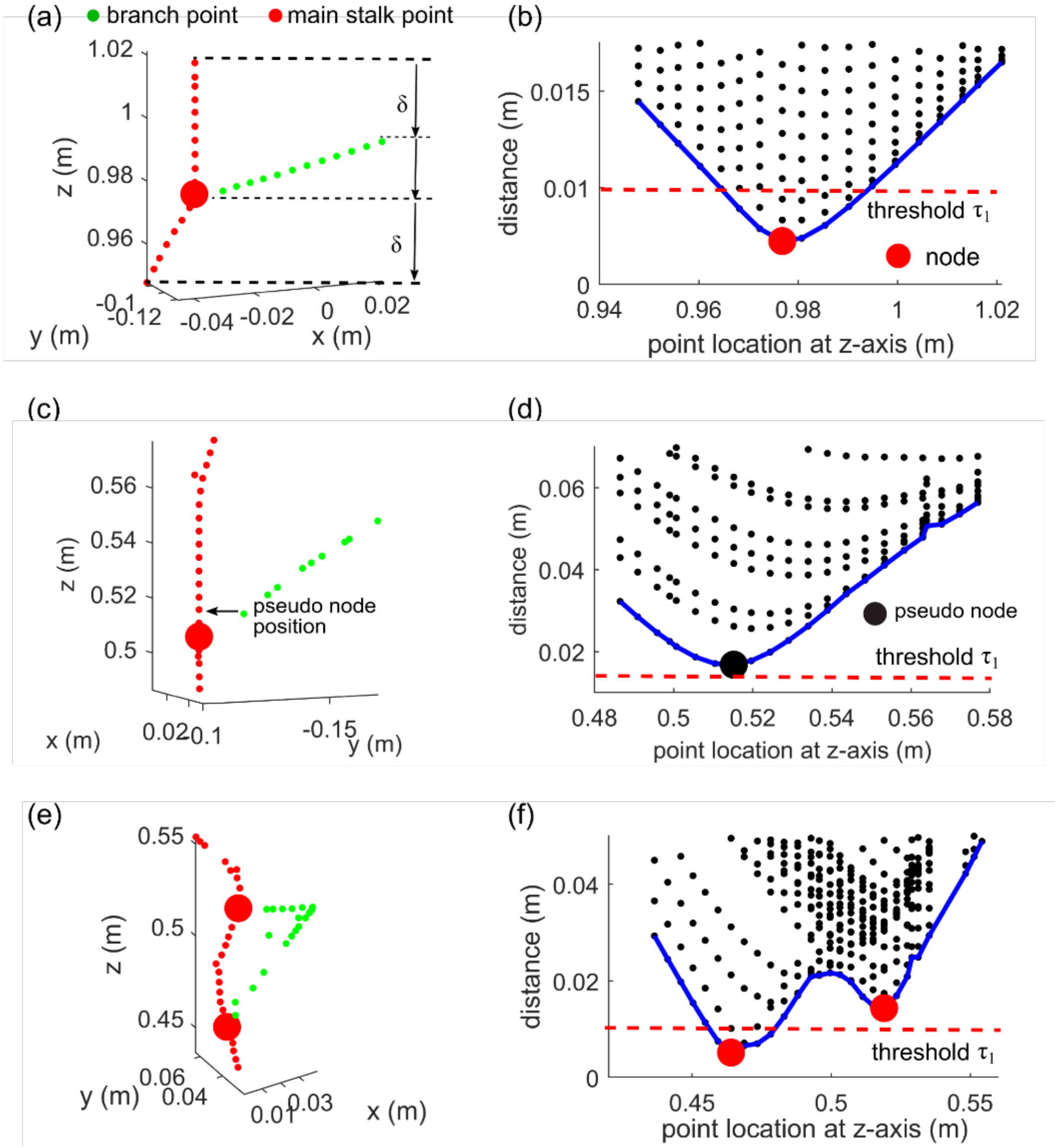

Figure 6.5. Schematic for the node localization algorithm. For situation (a), the branch was connected to the main stalk, the point (b) in the main stalk with minimum distance was considered to be the node; For situation (c), there was a gap between the main stalk and a branch, and the real node (d) was below the point with minimum distance. For situation (e), two local low peaks were detected, and the corresponding distance was less than the distance threshold, so the two nodes could be detected.

In addition, two more traits – plant height and HNR – could be measured. Plant height was calculated by accumulating the distance between two adjacent points of the whole main stalk points starting from the lowest point of the crown (eq (6.3)).

$$H = \sum_{i=1}^{M-1} d(i, i+1) \qquad (6.3)$$

where H was the plant height, M was the point number of the main stalk and $d(i, i+1)$ was the Euclidean distance between point i and $i+1$.

HNR was calculated using eq (6.4), and N was the detected node number.

$$HNR = {}^{H}\!/\!_{N} \qquad (6.4)$$

For plant node number counting, the mean absolute percentage error (*MAPE*) was computed between the algorithm measuring node numbers N_i and the manual measurements m_i by eq (6.5). P was the number of plants.

$$MAPE = \frac{\sum_{i=1}^{P} \frac{|N_i - m_i|}{m_i}}{P} \times 100\% \qquad (6.5)$$

In addition, the coefficient of determination (R^2) and the root-mean-squared error (RMSE) were calculated to assess the performance. These three metrics were also used to assess the other two phenotypic traits.

6.3. Results

6.3.1. Skeleton-based main stalk and individual branch identification

Overall, the extracted skeletons matched well with the original point clouds (Figure 6.6), maintaining plants topological and geometrical features while greatly reducing point numbers. In this study, a single plant had around 3~6 million points, while the skeleton had around 2~5 thousand points depending on the plant size. As demonstrated in Figure 6.6a, b and c, a branch was represented by a line of points in the extracted skeleton dataset. Although, for the plant in Figure 6.6a and b, the crown could be simply detected by selecting the lowest point of the skeleton, this would not work for the situation as shown in Figure 6.6c. Some skeleton points inside the red ellipse in Figure. 6.6c, which were generated by any branch touching the ground, might have the same height as the crown. In the proposed graph-based method, the points in the red ellipse could easily be removed based on the number of points for each sub-graph.

The main stalk could be reached by laser beams from all scanning perspectives; therefore, the occluded areas were small, resulting in small gaps in the main stalk skeleton (Figure 6.6b). Based on this observation, the parameter λ was set to be 2 cm for the step of initial main stalk point detection, and results showed that this setting was large enough to cover all gaps. For the well-extracted main stalk skeleton (no gaps existed), there were three skeleton points between two adjacent pre-detected main stalk points, as demonstrated in the zoomed-in figures in Figure 6.6a and c. Results of the main stalk points refinement operation showed that main stalk points were successfully detected for all plants. However, some branch points might be assigned to the main stalk point sets (Figure 6.6f). This would not affect the presence of node detection, but would cause the detected node location shift. More discussion was presented below.

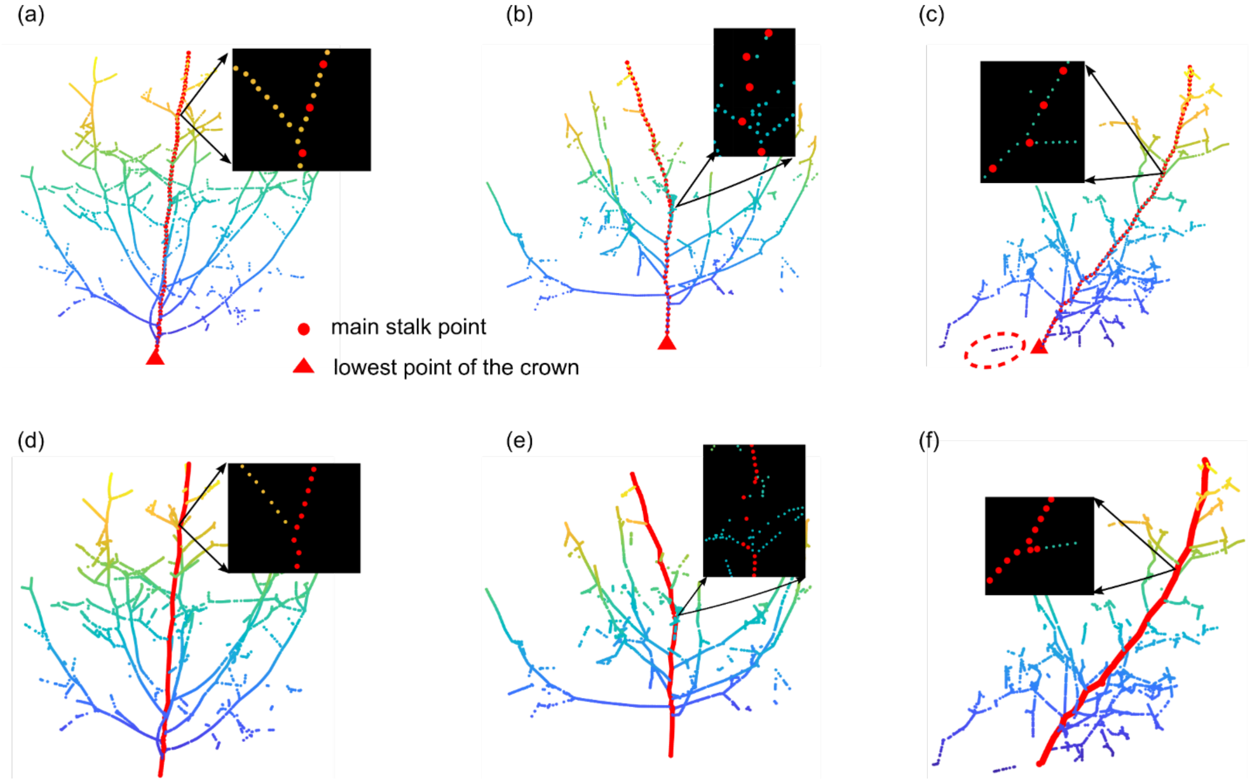

Figure 6.6. Extracted skeletons and main stalk detection results. The first row demonstrated the extracted skeletons, the lowest points of crowns (indicated by red triangles) and initial main stalk points (indicated by red dots) detection results. (a) Skeleton of a plant with a straight upward main stalk. (b) Skeleton of a plant with a tilted main stalk; gaps existed in the main stalk skeleton points. (c) Skeleton of a plant with a tilted main stalk, part of the branch skeleton points was at the same height as the root point. The second row ((d), (e) and (f)) demonstrated the main stalk detection results after refinement operation.

Branch structure became much simpler compared to the original situation after the pruning operation (Figure 6.7). We found that the circle radius *r* was flexible; experimental results showed the value did not affect the results when it was selected in a range of 10 to 20 cm. In this study, the circle radius *r* was set to be 15 cm. The parameters *Eps* and *MinPts* of DBSCAN clustering algorithm were selected as 2 cm 3, respectively, for the individual branch identification, considering the skeleton resolution configuration and potential skeleton gap size. Results showed that most of the ‘pruned’ branches were successfully grouped into different clusters. However, it was observed that a branch might be divided into different clusters due to the gaps (Figure 6.7a), and branches which were too close to each other would be grouped in the same cluster (Figure 6.7c). These misclustering results would be addressed by the node detection method described in Figure 6.5.

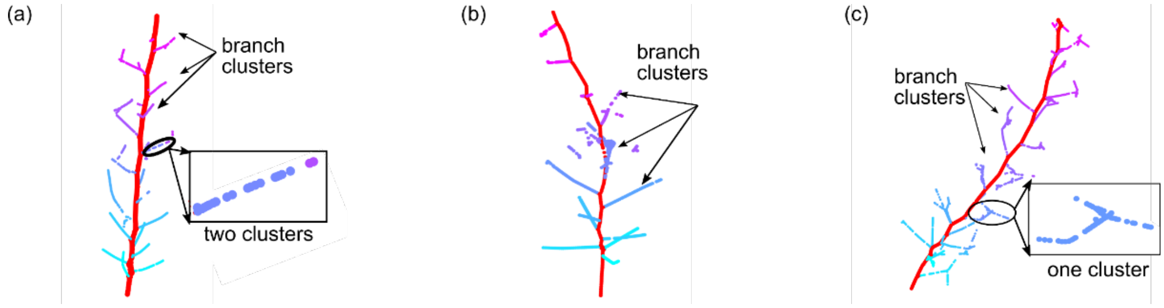

Figure 6.7. Individual branch identification results for the two kinds of representative plant architectures. (a) A plant with a straight upward main stalk; (b) and (c) Plants with tilted main stalks. The main stalk points were indicated in red. For branches, each color represented a detected branch cluster.

6.3.2. Results of plant architecture trait measurements

Overall, the proposed node detection method performed well to identify cotton plant nodes (Figure. 6.8 and 6.9). Usually, nodes at the lower part of a plant were denser than those located at a higher level, and the proposed method was able to distinguish them due to the skeleton resolution configuration. In the case that a branch was divided into two or more clusters (Figure 6.7a), the cluster which was far away from the main stalk could be removed using the distance filter (τ_1 = 3 cm); the parameter τ_2 was set to be 1cm, if the gap between the branch cluster and the main stalk was in the range (τ_1, τ_2); the node position was estimated by finding the point which was two points below the pseudo node. For the situation demonstrated in Figure 6.6f, a node was detected, but the location was shifted a few points (Figure 6.8c). This was one of the limitations for the main stalk points detection. The total ground truth of the nodes was 475 for 26 plants, and the algorithm detected nodes was 458, including 9 false positive (FP) detections and 26 false negative (FN) detections, resulting in an R^2 of 0.88, and MAPE, and RMSE of 3.23%, and 0.7, respectively (Figure 6.9).

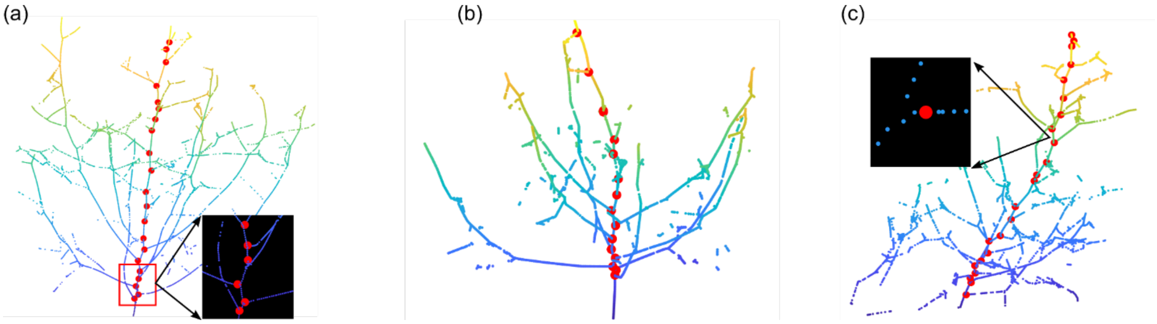

Figure 6.8. Representative results of node detection. (a) A plant with normal architecture; (b) and (c) Plants with tilted main stalks. Detected nodes are indicated in red.

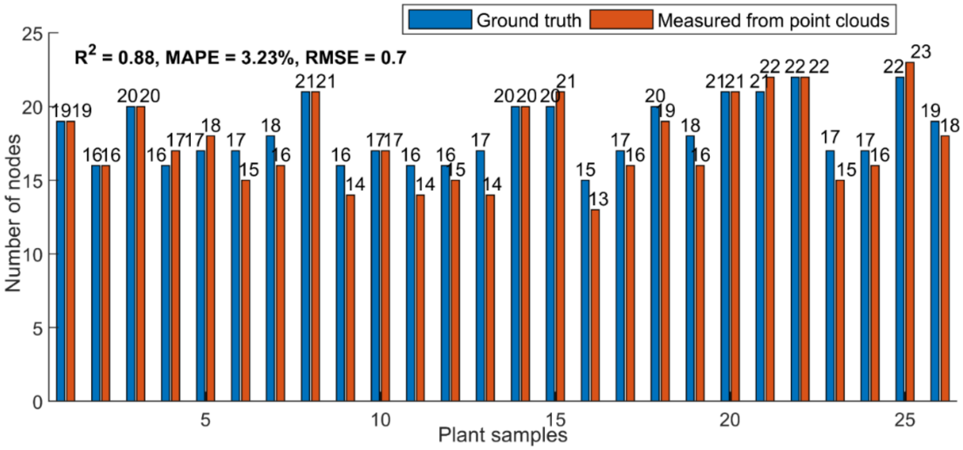

Figure 6.9. Performance of node detection results.

Plant heights were well derived from the main stalk skeleton points, with the R^2, MAPE, and RMSE of 0.93, 3.89%, and 4.7 cm, respectively (Figure 6.10a). The R^2, MAPE, and RMSE of HNR were 0.72, 6.24% and 0.4 cm/node, respectively (Figure 6.10b).

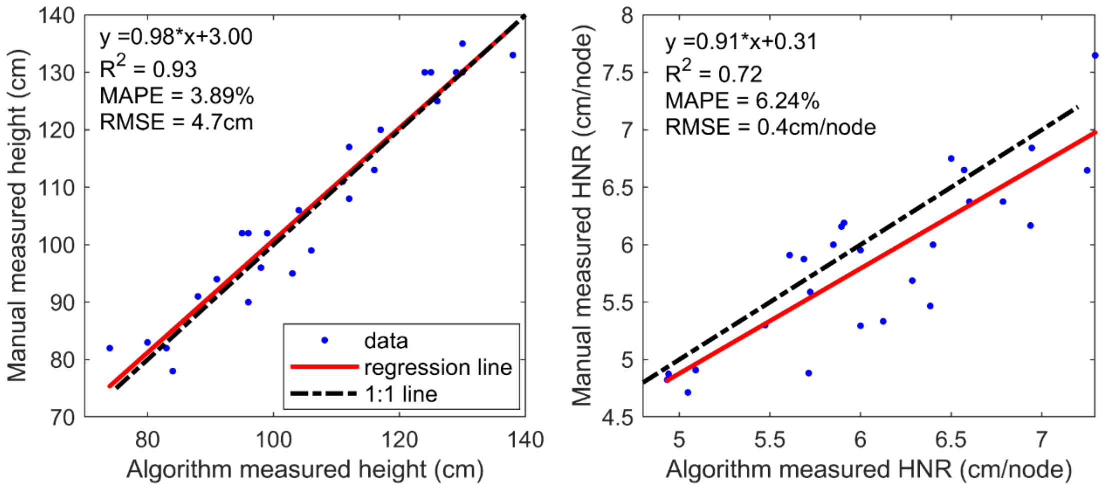

Figure 6.10. Performance of plant height and Height-to-Node ratio measurement. (a) Correlation analysis of plant height; (b) Correlation analysis of Height-to-Node ratio.

6.4. Discussion

Highly accurate point clouds of plants can be obtained using the 3D LiDAR with multi-view scanning strategy under field conditions, which provide a detailed and precise representation of plants, enabling retrieving plant phenotypic traits at both the canopy level and organ level (Dhondt et al., 2013). The multi-view scanning strategy greatly reduces the possibility of occlusion, which is one of the biggest challenges for phenotypic trait extraction form 2D images. However, one limitation is that it takes a relatively long time for data collection. Therefore, scanning positions will be optimized in the future, keeping the quality and density of point cloud data while reducing the number of scanning positions. For example, a plant can be scanned from fewer perspectives, such as three (each scan covering 120°) or even two (each scan covering 180°); another potential solution would be to mount the LiDAR at a higher position so that it can cover a larger field area (more plants) (Malambo et al., 2019; Wu et al., 2019), while configuring the sensor at a higher scanning resolution to achieve the same level of accuracy. Furthermore, the sensor can be mounted on a GPS-navigated robot platform, and point cloud registration operation can be conducted while collecting data. An efficient data collection method would be extremely useful for large field applications.

Overall, the skeleton extraction method performed well for cotton plants which had wide variation in appearance of the architecture, although there existed small occluded areas. In order to address the issue of 'gaps' existing in the skeletons, a parameter λ, which was four times larger than the skeleton resolution, was used for the main stalk detection to ensure that two coarse adjacent connected points in the graph can cover the gaps. 'Gaps' also exist between a branch and the main stalk as shown in Figure 6.5c, resulting in the detected node location is not accurate.

It was observed that the method produced a higher FN rate than FP rate for node detection, which was attributed to the situation that there was a big gap between a branch and the main stalk skeleton points (Figure 6.11a, b and c). Some branches, especially those located at the top of a plant, were of a small stem diameter, resulting in less points in the original point cloud compared to those with a larger stem diameter. After down-sampling, the full skeleton of the branches with a small stem diameter might not be retrieved if they generate a very limited number of points. Figure 6.11d demonstrates a representative situation for FP node detection. There is a sub-branch, which is close to the main stalk, and ghost points appear due to the point cloud registration operation and environmental factors such as wind, resulting in the corresponding branch skeleton points being very close to the main stalk (Figure 6.11e). The node detection method would detect this as a node (Figure 6.11f).

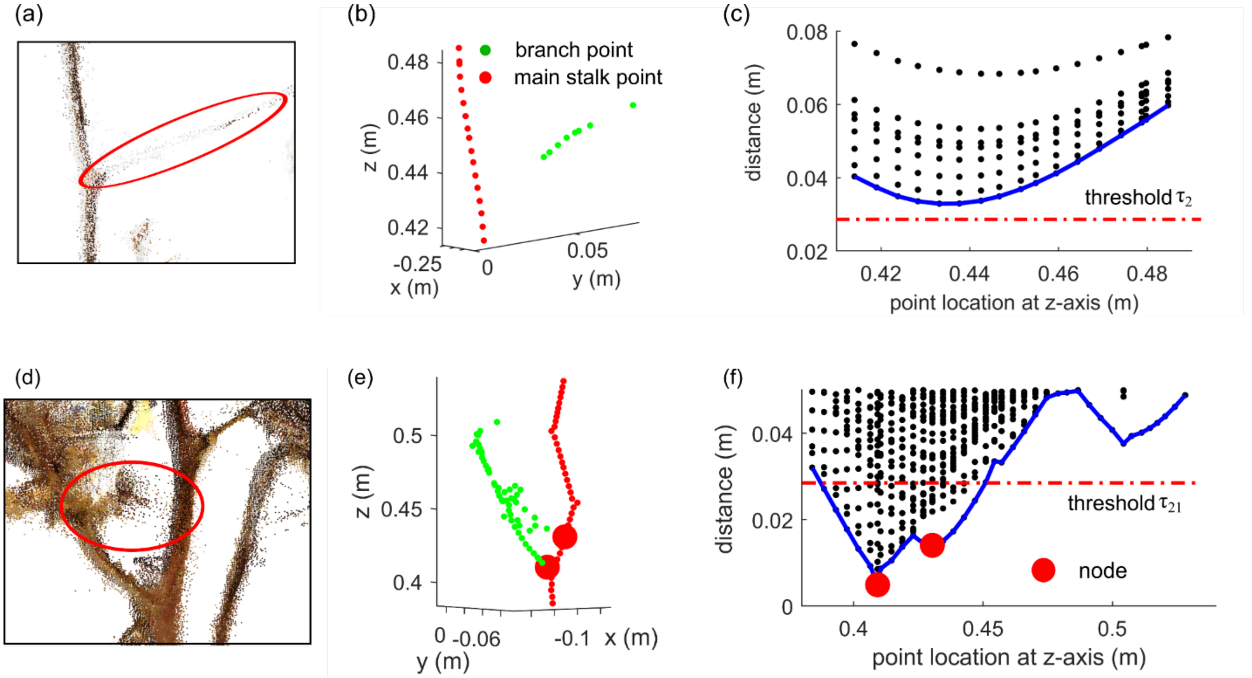

Figure 6.11. Error analysis for false negative and false positive node detection. The first row is to demonstrate FN. Incomplete point cloud for a branch in (a). For the skeleton, there is a gap between the branch and the main stalk (b). The smallest distance is greater than the outliner threshold (c), resulting in a missing node. The second row is to demonstrate FP. The sub-branch is almost connected to the main stalk due to noisy points in (d). For the skeleton (e), although there is a small gap, it is less than the distance threshold, so two nodes are detected (f).

Skeleton quality plays a vital role in node detection; therefore, future work will focus on optimization of the skeleton extraction algorithm. New algorithms will be developed to retrieve skeletons from incomplete point clouds. For example, the structure pattern of the visible branches can be used to predict branch growth direction (Li and Wang, 2018; Mei et al., 2016). A point cloud down-sampling method can also contribute to improve skeleton quality. In this study, the original point clouds were down-sampled using an evenly voxel-based method. For small stem branches, which generate fewer points than big ones, the point number may be too small to extract a fine skeleton after the down-sampling operation. If the down-sampling operation was conducted based on point density information, i.e., a branch which has a low density of points, fewer points would be removed during the down-sampling operation; otherwise, more points are removed. This down-sampling method could result in a more evenly distributed point cloud, which is good for skeleton extraction. If the skeleton could be well-extracted, no gaps would exist, and the proposed method could become simpler. For example, the main stalk detection could be implemented just by the first step via setting the parameter λ as a value in the range of (ε, 2ε). The node position would not be affected by the gaps between a branch and the main stalk described in Figure 6.5c and Figure 6.6f.

Overall the measured plant height was underestimated, which is also related to the skeleton quality. Similar to branches, main stalks at the top of plants are thinner, resulting in more limited points. Therefore, skeletons may not be generated completely for that part. The reasons for errors of node detection and plant height measurement jointly contribute to the measurement error of HNR.

In addition to the traits extracted in this study, more traits can be extracted from the point cloud data. For example, if whole branches, not just part of them as in this study, could be identified, combined with cotton boll detection technology (Sun et al., 2018a), information as to where each cotton boll is located on each branch could be obtained. Branch angle (the angle between a branch and the main stalk) also could be estimated from the skeleton. A plant with average, small branch angles indicates that the plant architecture exhibits more upright branches, producing a more compact shape. This is helpful to increase plant density and improve final yield (Tian et al., 2019). Other traits such as canopy size and plant volume could also be detected. New algorithms will be developed for these traits.

Another limitation of the proposed method is that the main stalk detection method is designed only for the situation in which the highest point of the plant is at the main stalk. However, some plants may not satisfy this requirement. For example, a plant may fall down due to wind or other environmental factors, resulting in one of the branches being the highest point as demonstrated in Figure 6.2c. Some plant species may also exhibit an abnormal pattern, such as “Pima” cotton (Jiang et al., 2018). The main stalk detection method will be optimized in the future.

6.5. Conclusions

Highly accurate point cloud data was obtained using a high-resolution terrestrial 3D LiDAR sensor, providing opportunities to retrieve plant organ level phenotypic traits with a high accuracy. The proposed methods for node, plant height and HNR were robust, although the plants had complex topological and geometrical patterns. In the future, new scanning strategies requiring fewer scans while maintaining the same accuracy will be explored to save field data collection time, and new algorithms will be developed to retrieve more traits from point clouds.

CHAPTER 7

CONCLUSIONS AND FUTURE WORK

7.1 Conclusions

Overall, the developed 3D imaging system and methodologies can accurately measure phenotypic traits, not only automating phenotypes that are traditionally measured manually such as plant canopy height, cotton boll number and plant node number and internode distance, but also extracting new traits such canopy projected area, plant volume, cotton boll size and position. The systems and methodologies can be used as tools for plant researchers and growers alike. In addition, they can be used for other crops such as wheat and maize after minor modifications.

However, there are a few limitations for the systems and methodologies as follows:

1. The ground vehicle-based platforms for data acquisition is inefficient because a driver is needed for the current platforms and the ground vehicle consumes more energy compared to robot-based platforms. In addition, the ground vehicle is very heavy, causing soil compaction when conducting periodic data collection for the whole crop growing season.
2. Although good performance was achieved for the 3D cotton boll voxel segmentation based on the handcrafted features, new feature extraction methods such as deep learning and more features are needed in order to improve the resistance of segmentation to varied environmental conditions.

3. The current scanning strategy of the 3D terrestrial LiDAR are inefficient, limiting large field applications. New scanning strategies, which can balance data quality and scanning efficiency, need to be designed.
4. The skeleton extraction method needs to be optimized in order to improve the capability of handling point clouds with different local point densities.

7.2 Future Work

Experimental results in this dissertation demonstrated that the 3D imaging technologies have great potential and advantages for the applications of field-based plant high throughput phenotyping. The developed sensing systems and data processing algorithms can be improved by applying new technologies such as robotics and artificial intelligence, through which more traits can be extracted more efficiently in the future. Detailed information about the future work is listed as follows:

1. Developing robotic infield phenotyping platforms. Robots can work with less human involvement and both at day and night to further improve the efficiency of infield data collection. In addition, multiple robots can be designed to work coordinately, further improving the efficiency of data collection, which is particularly useful for large field applications.
2. It is worthwhile to explore 3D deep learning technologies for point cloud data processing, implementing end-to-end plant phenotypic trait detection. Deep learning network is capable of learning features automatically from training datasets, which is helpful to improve the object detection performance when applying in varied environmental conditions.

3. Developing methodologies to compensate for missing points for acquired incomplete point clouds. Occlusion problem is hard to be fully avoided although a multi-view scanning strategy is used for data collection, which is one of major challenges for further phenotypic traits extraction, especially for organ level traits. Combining point compensation algorithms and multi-view scanning methods is a good way to obtain full point cloud data.
4. Building mathematic models to simulate crop growth in computers by incorporating high resolution 3D imaging data of plants throughout the life cycle. The models can be used to study spatial-temporal dynamics of crop growth, improving the understanding of biology and accelerating the process of new cultivar selection.
5. Building crop yield prediction models. Accurate yield prediction is very important for crop production. For example, growers rely on the information to arrange logistics in advance; policy makers need it to make decisions about food import and export plans, ensuring national food security. As demonstrated in this dissertation, the developed systems and methodologies could help find yield components. In the future, when more yield related traits are identified, crop yield could be predicted by fusing phenotype, genotype, and environmental data.
6. Collecting more data in different years and locations with more cultivars to further validate and improve the developed systems and methodologies in the future.
7. Performing quantitative trait locus or genome-wide association study analysis using the novel extracted phenotypic traits by collaborating with plant scientists.

REFERENCES

Andrade-Sanchez, P., Gore, M.A., Heun, J.T., Thorp, K.R., Carmo-Silva, A.E., French, A.N., Salvucci, M.E., White, J.W., 2013. Development and evaluation of a field-based high-throughput phenotyping platform. Functional Plant Biology 41, 68-79.

Andújar, D., Rosell-Polo, J., Sanz, R., Rueda-Ayala, V., Fernández-Quintanilla, C., Ribeiro, A., Dorado, J., 2016. A LiDAR-based system to assess poplar biomass. Gesunde Pflanzen 68, 155-162.

Auat Cheein, F.A., Guivant, J., Sanz, R., Escolà, A., Yandún, F., Torres-Torriti, M., Rosell-Polo, J.R., 2015. Real-time approaches for characterization of fully and partially scanned canopies in groves. Computers and Electronics in Agriculture 118, 361-371.

Awlia, M., Nigro, A., Faikus, J., Schmoeckel, S.M., Negrao, S., Santelia, D., Trtilek, M., Tester, M., Julkowska, M.M., Panzarova, K., 2016. High-throughput non-destructive phenotyping of traits that vontribute to salinity tolerance in arabidopsis thaliana. Frontiers in Plant Science 7, 1-15.

Bac-Molenaar, J.A., Vreugdenhil, D., Granier, C., Keurentjes, J.J., 2015. Genome-wide association mapping of growth dynamics detects time-specific and general quantitative trait loci. Journal of Experimental Botany, 5567-5580.

Baloch, M., Khan, N., Rajput, M., Jatoi, W., Gul, S., Rind, I., Veesar, N., 2014. Yield related morphological measures of short duration cotton genotypes. J. Anim. Plant Sci 24, 1198-1211.

Bao, T., Melenka, G.W., Ljubotina, M.K., Carey, J.P., Cahill, J.F., 2018. A new method for the rapid characterization of root growth and distribution using digital image correlation. New Phytologist 218, 835-846.

Bao, Y., Tang, L., Srinivasan, S., Schnable, P.S.J.B.E., 2019. Field-based architectural traits characterisation of maize plant using time-of-flight 3D imaging. Biosystems Engineering 178, 86-101.

Bargoti, S., Underwood, J.P., 2017. Image segmentation for fruit detection and yield estimation in apple orchards. Journal of Field Robotics 34, 1039-1060.

Barker III, J., Zhang, N., Sharon, J., Steeves, R., Wang, X., Wei, Y., Poland, J., 2016. Development of a field-based high-throughput mobile phenotyping platform. Computers and Electronics in Agriculture 122, 74-85.

Bhardwaj, A., Sam, L., Bhardwaj, A., Martín-Torres, F.J., 2016. LiDAR remote sensing of the cryosphere: Present applications and future prospects. Remote Sensing of Environment 177, 125-143.

Bietresato, M., Carabin, G., Vidoni, R., Gasparetto, A., Mazzetto, F., 2016. Evaluation of a LiDAR-based 3D-stereoscopic vision system for crop-monitoring applications. Computers and Electronics in Agriculture 124, 1-13.

Brown, T., Zimmermann, C., Panneton, W., Noah, N., Borevitz, J., 2012. High-resolution, time-lapse imaging for ecosystem-scale phenotyping in the field. High-Throughput Phenotyping in Plants: Methods and Protocols, 71-96.

Busemeyer, L., Mentrup, D., Möller, K., Wunder, E., Alheit, K., Hahn, V., Maurer, H., Reif, J., Würschum, T., Müller, J., Rahe, F., Ruckelshausen, A., 2013a. BreedVision — A Multi-Sensor Platform for Non-Destructive Field-Based Phenotyping in Plant Breeding. Sensors 13, 2830.

Busemeyer, L., Ruckelshausen, A., Muller, K., Melchinger, A.E., Alheit, K.V., Maurer, H.P., Hahn, V., Weissmann, E.A., Reif, J.C., Wurschum, T., 2013b. Precision phenotyping of biomass accumulation in triticale reveals temporal genetic patterns of regulation. Scientific reports 3, 1-6.

Butler, E.E., Datta, A., Flores-Moreno, H., Chen, M., Wythers, K.R., Fazayeli, F., Banerjee, A., Atkin, O.K., Kattge, J., Amiaud, B., 2017. Mapping local and global variability in plant trait distributions. Proceedings of the National Academy of Sciences 114, E10937-E10946.

Campbell, Z.C., Acosta-Gamboa, L.M., Nepal, N., Lorence, A., 2018. Engineering plants for tomorrow: how high-throughput phenotyping is contributing to the development of better crops. Phytochemistry Reviews 17, 1329-1343.

Cao, J., Tagliasacchi, A., Olson, M., Zhang, H., Su, Z., 2010. Point cloud skeletons via laplacian based contraction, IEEE Shape Modeling International (SMI 2010), pp. 187-197.

Carlone, L., Dong, J., Fenu, S., Rains, G., Dellaert, F., 2015. Towards 4d crop analysis in precision agriculture: Estimating plant height and crown radius over time via expectation-maximization, ICRA Workshop on Robotics in Agriculture, pp. 1-8.

Chen, Q., Lai, H., Wang, X., Ren, L., Liu, J., 2013. An cotton image segmentation algorithm based on support vector machine. Computer Engineering 39, 266-269.

Chu, T., Starek, M.J., Brewer, M.J., Murray, S.C., Pruter, L.S., 2018. Characterizing canopy height with UAS structure-from-motion photogrammetry—results analysis of a maize field trial with respect to multiple factors. Remote Sensing Letters 9, 753-762.

Cobb, J.N., DeClerck, G., Greenberg, A., Clark, R., McCouch, S., 2013. Next-generation phenotyping: requirements and strategies for enhancing our understanding of genotype–phenotype relationships and its relevance to crop improvement. Theoretical and Applied Genetics 126, 867-887.

Collins, G., 2013. Plant Growth Regulator (PGR) Management Considerations for the 2013 Crop. http://www.ugacotton.com/2013/07/plant-growth-regulator-pgr-management-considerations-for-the-2013-crop-collins-and-whitaker/.

Colomina, I., Molina, P., 2014. Unmanned aerial systems for photogrammetry and remote sensing: A review. ISPRS Journal of Photogrammetry & Remote Sensing 92, 79-97.

Conn, A., Pedmale, U.V., Chory, J., Stevens, C.F., Navlakha, S., 2017. A Statistical Description of Plant Shoot Architecture. Current Biology 27, 2078-2088.

Constable, G.A., Bange, M.P., 2015. The yield potential of cotton (Gossypium hirsutum L.). Field Crops Research 182, 98-106.

Cordell, D., Drangert, J.-O., White, S., 2009. The story of phosphorus: Global food security and food for thought. Global Environmental Change 19, 292-305.

Crist, E., Mora, C., Engelman, R., 2017. The interaction of human population, food production, and biodiversity protection. Science 356, 260-264.

Crommelinck, S., Höfle, B., 2016. Simulating an Autonomously Operating Low-Cost Static Terrestrial LiDAR for Multitemporal Maize Crop Height Measurements. Remote Sensing 8, 1-17.

Cui, T.-t., He, K.-h., Chang, L.-g., Zhang, X.-h., Xue, J.-q., Liu, J.-c., 2017. QTL mapping for leaf area in maize (Zea mays L.) under multi-environments. Journal of Integrative Agriculture 16, 800-808.

Czedik-Eysenberg, A., Seitner, S., Guldener, U., Koemeda, S., Jez, J., Colombini, M., Djamei, A., 2018. The 'PhenoBox', a flexible, automated, open-source plant phenotyping solution. New Phytologist 219, 808-823.

Deery, D., Jimenez-Berni, J., Jones, H., Sirault, X., Furbank, R., 2014. Proximal remote sensing buggies and potential applications for field-based phenotyping. Agronomy 4, 349-379.

Dhondt, S., Wuyts, N., Inze, D., 2013. Cell to whole-plant phenotyping: the best is yet to come. Trends in Plant Science 18, 433-444.

Dodds, D.M., Banks, J., Barber, L.T., Boman, R.K., Brown, S.M., Edmisten, K.L., Faircloth, J.C., Jones, M.A., Lemon, R.G., Main, C.L., 2010. Beltwide evaluation of commercially available plant growth regulators. Journal of Cotton Science 14, 119-130.

Dong, J., Burnham, J.G., Boots, B., Rains, G.C., Dellaert, F., 2016. 4D Crop Monitoring: Spatio-Temporal Reconstruction for Agriculture. arXiv preprint arXiv:1610.02482.

Duan, T., Chapman, S.C., Holland, E., Rebetzke, G.J., Guo, Y., Zheng, B., 2016. Dynamic quantification of canopy structure to characterize early plant vigour in wheat genotypes. Journal of Experimental Botany 67, 4523-4534.

Earl, H.J., Davis, R.F., 2003. Effect of drought stress on leaf and whole canopy radiation use efficiency and yield of maize. Agronomy journal 95, 688-696.

Egal, F., 2019. Review of The State of Food Security and Nutrition in the World, 2019. World Nutrition 10, 95-97.

Fangueiro, R., Rana, S., 2016. Natural fibres: advances in science and technology towards industrial applications. Springer, Netherlands, Dordrecht.

Feng, A., Sudduth, K., Vories, E., Zhang, M., Zhou, J., 2018. Cotton Yield Estimation based on Plant Height From UAV-based Imagery Data, 2018 ASABE Annual International Meeting. ASABE, St. Joseph, MI, pp. 1-10.

Fernandez, M.G.S., Bao, Y., Tang, L., Schnable, P.S., 2017. A High-Throughput, Field-Based Phenotyping Technology for Tall Biomass Crops. Plant Physiology 174, 2008-2022.

Friedli, M., Kirchgessner, N., Grieder, C., Liebisch, F., Mannale, M., Walter, A., 2016. Terrestrial 3D laser scanning to track the increase in canopy height of both monocot and dicot crop species under field conditions. Plant Methods 12, 1-15.

Fu, L., Tola, E., Al-Mallahi, A., Li, R., Cui, Y., 2019. A novel image processing algorithm to separate linearly clustered kiwifruits. Biosystems Engineering 183, 184-195.

Furbank, R.T., Tester, M., 2011. Phenomics – technologies to relieve the phenotyping bottleneck. Trends in Plant Science 16, 635-644.

Furukawa, Y., Ponce, J., 2010. Accurate, dense, and robust multiview stereopsis. IEEE transactions on pattern analysis and machine intelligence 32, 1362-1376.

Gardner, M.P., 1985. Mood states and consumer behavior: A critical review. Journal of Consumer research 12, 281-300.

Garrido, M., Paraforos, D.S., Reiser, D., Vázquez Arellano, M., Griepentrog, H.W., Valero, C., 2015. 3D Maize Plant Reconstruction Based on Georeferenced Overlapping LiDAR Point Clouds. Remote Sensing 7, 17077-17096.

Gebbers, R., Ehlert, D., Adamek, R., 2011. Rapid Mapping of the Leaf Area Index in Agricultural Crops. Agronomy Journal 103, 1532-1541.

Gerland, P., Raftery, A.E., Ševčíková, H., Li, N., Gu, D., Spoorenberg, T., Alkema, L., Fosdick, B.K., Chunn, J., Lalic, N., 2014. World population stabilization unlikely this century. Science 346, 234-237.

Ghanem, M.E., Marrou, H., Sinclair, T.R., 2015. Physiological phenotyping of plants for crop improvement. Trends in Plant Science 20, 139-144.

Ghosal, S., Blystone, D., Singh, A.K., Ganapathysubramanian, B., Singh, A., Sarkar, S., 2018. An explainable deep machine vision framework for plant stress phenotyping. Proc. Natl. Acad. Sci. U. S. A. 115, 4613-4618.

Gibbs, J.A., Pound, M., French, A.P., Wells, D.M., Murchie, E., Pridmore, T., 2017. Approaches to three-dimensional reconstruction of plant shoot topology and geometry. Functional Plant Biology 44, 62-75.

Goggin, F.L., Lorence, A., Topp, C.N., 2015. Applying high-throughput phenotyping to plant–insect interactions: picturing more resistant crops. Current Opinion in Insect Science 9, 69-76.

Gongal, A., Amatya, S., Karkee, M., Zhang, Q., Lewis, K., 2015. Sensors and systems for fruit detection and localization: A review. Computers and Electronics in Agriculture 116, 8-19.

Granier, C., Vile, D., 2014. Phenotyping and beyond: modelling the relationships between traits. Current Opinion in Plant Biology 18, 96-102.

Großkinsky, D.K., Pieruschka, R., Svensgaard, J., Rascher, U., Christensen, S., Schurr, U., Roitsch, T., 2015. Phenotyping in the fields: dissecting the genetics of quantitative traits and digital farming. New Phytologist 207, 950-952.

Günaydin, G.K., Avinc, O., Palamutcu, S., Yavas, A., Soydan, A.S., 2019. Naturally Colored Organic Cotton and Naturally Colored Cotton Fiber Production, Organic Cotton. Springer, pp. 81-99.

Guo, J., Xu, S., Yan, D., Cheng, Z., Jaeger, M., Zhang, X., 2018a. Realistic Procedural Plant Modeling from Multiple View Images. IEEE Transactions on Visualization and Computer Graphics, 1-14.

Guo, Q.H., Wu, F.F., Pang, S.X., Zhao, X.Q., Chen, L.H., Liu, J., Xue, B.L., Xu, G.C., Li, L., Jing, H.C., Chu, C.C., 2018b. Crop 3D-a LiDAR based platform for 3D high-throughput crop phenotyping. Science China-Life Sciences 61, 328-339.

Herrero-Huerta, M., González-Aguilera, D., Rodriguez-Gonzalvez, P., Hernández-López, D., 2015. Vineyard yield estimation by automatic 3D bunch modelling in field conditions. Computers and Electronics in Agriculture 110, 17-26.

Hofle, B., 2014. Radiometric correction of terrestrial LiDAR point cloud data for individual maize plant detection. Geoscience and Remote Sensing Letters, IEEE 11, 94-98.

Hosoi, F., Omasa, K., 2012. Estimation of vertical plant area density profiles in a rice canopy at different growth stages by high-resolution portable scanning lidar with a lightweight mirror. Isprs Journal of Photogrammetry and Remote Sensing 74, 11-19.

Hosseini, M., McNairn, H., Merzouki, A., Pacheco, A., 2015. Estimation of Leaf Area Index (LAI) in corn and soybeans using multi-polarization C- and L-band radar data. Remote Sensing of Environment 170, 77-89.

Huang, Y., J. Brand, H., Sui, R., J. Thomson, S., Furukawa, T., Wayne Ebelhar, M., 2016. Cotton Yield Estimation Using Very High-Resolution Digital Images Acquired with a Low-Cost Small Unmanned Aerial Vehicle. Transactions of the ASABE 59, 1563-1574.

Isokane, T., Okura, F., Ide, A., Matsushita, Y., Yagi, Y., 2018. Probabilistic Plant Modeling via Multi-View Image-to-Image Translation. arXiv preprint arXiv:1804.09404.

Jiang, Y., Li, C., Paterson, A., Sun, S., Xu, R., Robertson, J., 2017. Quantitative analysis of cotton canopy size in field conditions using a consumer-grade RGB-D camera. Frontiers in plant science 8, 1-20.

Jiang, Y., Li, C., Paterson, A.H., 2016. High throughput phenotyping of cotton plant height using depth images under field conditions. Computers and Electronics in Agriculture 130, 57-68.

Jiang, Y., Li, C., Robertson, J.S., Sun, S., Xu, R., Paterson, A.H., 2018. GPhenoVision: A Ground Mobile System with Multi-modal Imaging for Field-based High Throughput Phenotyping of Cotton. Scientific reports 8, 1-15.

Jin, S., Su, Y., Wu, F., Pang, S., Gao, S., Hu, T., Liu, J., Guo, Q., 2018. Stem-leaf segmentation and phenotypic trait extraction of individual maize using terrestrial LiDAR data. IEEE Transactions on Geoscience Remote Sensing 57, 1336-1346.

Kaess, M., Johannsson, H., Roberts, R., Ila, V., Leonard, J.J., Dellaert, F., 2011. iSAM2: Incremental smoothing and mapping using the Bayes tree. The International Journal of Robotics Research, 216-236.

Kirchgessner, N., Liebisch, F., Yu, K., Pfeifer, J., Friedli, M., Hund, A., Walter, A., 2017. The ETH field phenotyping platform FIP: a cable-suspended multi-sensor system. Functional Plant Biology 44, 154-168.

Kjaer, K.H., Ottosen, C.-O., 2015. 3D laser triangulation for plant phenotyping in challenging environments. Sensors 15, 13533-13547.

Krieg, D.R., Sung, J., 1986. Source-sink relations as affected by water stress during boll development. Cotton physiology 7377, 73-81.

Kurtulmus, F., Lee, W.S., Vardar, A., 2013. Immature peach detection in colour images acquired in natural illumination conditions using statistical classifiers and neural network. Precision Agriculture 15, 57-79.

Kutulakos, K.N., Seitz, S.M., 1999. A theory of shape by space carving, Proceedings of the Seventh IEEE International Conference on Computer Vision, pp. 307-314.

LeCun, Y., Bengio, Y., Hinton, G., 2015. Deep learning. Nature 521, 436-444.

Leeuwen, M.v., Nieuwenhuis, M., 2010. Retrieval of forest structural parameters using LiDAR remote sensing. European Journal of Forest Research 129, 749-770.

Li, L., Wang, W., 2018. Improved Use of LOP for Curve Skeleton Extraction. Computer Graphics Forum 37, 313-323.

Li, L., Zhang, Q., Huang, D.F., 2014. A Review of Imaging Techniques for Plant Phenotyping. Sensors 14, 20078-20111.

Li, Y., Cao, Z., Lu, H., Xiao, Y., Zhu, Y., Cremers, A.B., 2016. In-field cotton detection via region-based semantic image segmentation. Computers and Electronics in Agriculture 127, 475-486.

Li, Y., Cao, Z., Xiao, Y., Cremers, A.B., 2017. DeepCotton: in-field cotton segmentation using deep fully convolutional network. Journal of Electronic Imaging 26, 1-15.

Lin, Y., 2015. LiDAR: An important tool for next-generation phenotyping technology of high potential for plant phenomics? Computers and Electronics in Agriculture 119, 61-73.

Lipka, A.E., Kandianis, C.B., Hudson, M.E., Yu, J., Drnevich, J., Bradbury, P.J., Gore, M.A., 2015. From association to prediction: statistical methods for the dissection and selection of complex traits in plants. Current Opinion in Plant Biology 24, 110-118.

Liu, J.-S., Lai, H.-C., Jia, Z.-H., 2011. Image segmentation of cotton based on YCbCcr color space and fisher discrimination analysis. Acta Agronomica Sinica 33, 1274-1279.

Liu, S., Martre, P., Buis, S., Abichou, M., Andrieu, B., baret, F., 2019. Estimation of plant and canopy architectural traits using the D3P Digital Plant Phenotyping Platform. Plant Physiology 181, 881-890.

Llorens, J., Gil, E., Llop, J., 2011. Ultrasonic and LIDAR sensors for electronic canopy characterization in vineyards: Advances to improve pesticide application methods. Sensors 11, 2177-2194.

Lobell, D.B., Schlenker, W., Costa-Roberts, J., 2011. Climate trends and global crop production since 1980. Science 333, 616-620.

Luo, L.F., Tang, Y.C., Zou, X.J., Ye, M., Feng, W.X., Li, G.Q., 2016. Vision-based extraction of spatial information in grape clusters for harvesting robots. Biosystems Engineering 151, 90-104.

Luo, S., Wang, C., Pan, F., Xi, X., Li, G., Nie, S., Xia, S., 2015. Estimation of wetland vegetation height and leaf area index using airborne laser scanning data. Ecological Indicators 48, 550-559.

Malambo, L., Popescu, S., Horne, D., Pugh, N., Rooney, W., 2019. Automated detection and measurement of individual sorghum panicles using density-based clustering of terrestrial lidar data. ISPRS Journal of Photogrammetry and Remote Sensing 149, 1-13.

Malik, Z., Ziauddin, S., Shahid, A.R., Safi, A., 2016. Detection and Counting of On-Tree Citrus Fruit for Crop Yield Estimation. International Journal of Advanced Computer Science and Applications 7, 519-523.

Masuda, T., 2019. 3D Shape Reconstruction of Plant Roots in a Cylindrical Tank From Multiview Images, Proceedings of the IEEE International Conference on Computer Vision Workshops, pp. 1-10.

Mathan, J., Bhattacharya, J., Ranjan, A., 2016. Enhancing crop yield by optimizing plant developmental features. Development 143, 3283-3294.

Mauney, J.R., 1986. Vegetative growth and development of fruiting sites.

McCarthy, C., Hancock, N., Raine, S., 2009. Automated internode length measurement of cotton plants under field conditions. Transactions of the ASABE 52, 2093-2103.

McCarthy, C., Hancock, N., Raine, S., 2010. Apparatus and Infield Evaluations of a Prototype Machine Vision System for Cotton Plant Internode Length Measurement. Journal of Cotton Science 14, 221-232.

McCormick, R.F., Truong, S.K., Mullet, J.E., 2016. 3D Sorghum Reconstructions from Depth Images Identify QTL Regulating Shoot Architecture. Plant Physiology 172, 823-834.

Mei, J., Zhang, L., Wu, S., Wang, Z., Zhang, L., 2016. 3D tree modeling from incomplete point clouds via optimization and L1-MST. International Journal of Geographical Information Science 31, 999-1021.

Méndez, V., Rosell-Polo, J.R., Pascual, M., Escolà, A., 2016. Multi-tree woody structure reconstruction from mobile terrestrial laser scanner point clouds based on a dual neighbourhood connectivity graph algorithm. Biosystems Engineering 148, 34-47.

Miller, N.D., Haase, N.J., Lee, J., Kaeppler, S.M., de Leon, N., Spalding, E.P.J.T.P.J., 2017. A robust, high-throughput method for computing maize ear, cob, and kernel attributes automatically from images. The Plant Journal 89, 169-178.

Monteith, J.L., 1994. Validity of the correlation between intercepted radiation and biomass. Agricultural and Forest Meteorology 68, 213-220.

Monteith, J.L., Moss, C., 1977. Climate and the efficiency of crop production in Britain. Philosophical Transactions of the Royal Society of London. Series B, Biological Sciences, 277-294.

Munoz, D., 2013. Inference Machines Parsing Scenes via Iterated Predictions. Carnegie Mellon University, Pittsburgh, Pennsylvania, USA.

Murgoitio, J., Shrestha, R., Glenn, N., Spaete, L., 2014. Airborne LiDAR and terrestrial laser scanning derived vegetation obstruction factors for visibility models. Transactions in GIS 18, 147-160.

Nguyen, T.T., Slaughter, D.C., Townsley, B., Carriedo, L., Julin, N., Sinha, N., 2016. Comparison of structure-from-motion and stereo vision techniques for full in-field 3d reconstruction and phenotyping of plants: An investigation in sunflower, 2016 ASABE Annual International Meeting. American Society of Agricultural and Biological Engineers, Orlando, FL, USA, pp. 17-20.

Ninomiya, S., Baret, F., Cheng, Z.-M.M., 2019. Plant phenomics: emerging transdisciplinary science. Plant phenomics 2019, 1-3.

Nuske, S., Wilshusen, K., Achar, S., Yoder, L., Singh, S., 2014. Automated Visual Yield Estimation in Vineyards. Journal of Field Robotics 31, 837-860.

Oberti, R., Shapiro, A., 2016. Advances in robotic agriculture for crops. Biosystems Engineering 146, 1-2.

Ollivier, Q.R., Maher, D.T., Pitfield, C., Macreadie, P.I., 2019. Punching above their weight: Large release of greenhouse gases from small agricultural dams. Global change biology 25, 721-732.

Oosterhuis, D.M., Kerby, T.A., 2008. Measures of Cotton Growth and Development. Crop Management System 21, 21-25.

Ortiz-Reyes, E., Anex, R.P., 2018. A life cycle impact assessment method for freshwater eutrophication due to the transport of phosphorus from agricultural production. Journal of cleaner production 177, 474-482.

Pajares, G., 2015. Overview and Current Status of Remote Sensing Applications Based on Unmanned Aerial Vehicles (UAVs). Photogrammetric Engineering and Remote Sensing 81, 281-329.

Palanichamy, D., Cobb, J.N., 2015. Agronomic Field Trait Phenomics, Phenomics. Springer, pp. 83-99.

Papon, J., Abramov, A., Schoeler, M., Wörgötter, F., 2013. Voxel cloud connectivity segmentation-supervoxels for point clouds, 2013 IEEE Conference on Computer Vision and Pattern Recognition (CVPR). IEEE, Portland, Oregon, USA, pp. 2027-2034.

Paproki, A., Sirault, X., Berry, S., Furbank, R., Fripp, J., 2012. A novel mesh processing based technique for 3D plant analysis. BMC Plant Biology 12, 1-13.

Pastrana, J.C., Rath, T., 2013. Novel image processing approach for solving the overlapping problem in agriculture. Biosystems Engineering 115, 106-115.

Paulus, S., 2019. Measuring crops in 3D: using geometry for plant phenotyping. Plant Methods 15, 1-13.

Paulus, S., Dupuis, J., Mahlein, A.-K., Kuhlmann, H., 2013. Surface feature based classification of plant organs from 3D laserscanned point clouds for plant phenotyping. BMC bioinformatics 14, 1-12.

Paulus, S., Dupuis, J., Riedel, S., Kuhlmann, H., 2014a. Automated Analysis of Barley Organs Using 3D Laser Scanning: An Approach for High Throughput Phenotyping. Sensors 14, 12670-12686.

Paulus, S., Schumann, H., Kuhlmann, H., Léon, J., 2014b. High-precision laser scanning system for capturing 3D plant architecture and analysing growth of cereal plants. Biosystems Engineering 121, 1-11.

Pearse, G.D., Watt, M.S., Morgenroth, J., 2016. Comparison of optical LAI measurements under diffuse and clear skies after correcting for scattered radiation. Agricultural and Forest Meteorology 221, 61-70.

Pforte, F., Selbeck, J., Hensel, O., 2012. Comparison of two different measurement techniques for automated determination of plum tree canopy cover. Biosystems Engineering 113, 325-333.

Pieruschka, R., Schurr, U., 2019. Plant Phenotyping: Past, Present, and Future. Plant Phenomics 2019, 1-6.

Pratap, A., Tomar, R., Kumar, J., Pandey, V.R., Mehandi, S., Katiyar, P.K., 2015. High-Throughput Plant Phenotyping Platforms, Phenomics in Crop Plants: Trends, Options and Limitations. Springer, pp. 285-296.

Qi, C.R., Yi, L., Su, H., Guibas, L.J., 2017. Pointnet++: Deep hierarchical feature learning on point sets in a metric space, Advances in Neural Information Processing Systems, Long Beach, California, USA, pp. 5105-5114.

Qureshi, W.S., Payne, A., Walsh, K.B., Linker, R., Cohen, O., Dailey, M.N., 2017. Machine vision for counting fruit on mango tree canopies. Precision Agriculture 18, 224-244.

Rahaman, M.M., Chen, D.J., Gillani, Z., Klukas, C., Chen, M., 2015. Advanced phenotyping and phenotype data analysis for the study of plant growth and development. Frontiers in Plant Science 6, 1-15.

Rahnemoonfar, M., Sheppard, C., 2017. Deep Count: Fruit Counting Based on Deep Simulated Learning. Sensors (Basel) 17, 1-17.

Rebetzke, G.J., Jimenez-Berni, J.A., Bovill, W.D., Deery, D.M., James, R.A., 2016. High-throughput phenotyping technologies allow accurate selection of stay-green. Journal of Experimental Botany 67, 4919-4924.

Remagnino, P., Mayo, S., Wilkin, P., Cope, J., Kirkup, D., 2016. Computational Botany: Methods for Automated Species Identification. Springer.

Richardson, J.J., Moskal, L.M., Kim, S.-H., 2009. Modeling approaches to estimate effective leaf area index from aerial discrete-return LIDAR. Agricultural and Forest Meteorology 149, 1152-1160.

Ritchie, G.L., Bednarz, C.W., Jost, P.H., Brown, S.M., 2007. Cotton growth and development. Bulletin 1252. Athens, GA: Cooperative Extension Service and the University of Georgia College of Agricultural and Environmental Sciences.

Rosell-Polo, J.R., Llorens, J., Sanz, R., Arnó, J., Ribes-Dasi, M., Masip, J., Escolà, A., Camp, F., Solanelles, F., Gràcia, F., Gil, E., Val, L., Planas, S., Palacín, J., 2009. Obtaining the three-dimensional structure of tree orchards from remote 2D terrestrial LIDAR scanning. Agricultural and Forest Meteorology 149, 1505-1515.

Rosell Polo, J.R., Sanz, R., Llorens, J., Arnó, J., Escolà, A., Ribes-Dasi, M., Masip, J., Camp, F., Gràcia, F., Solanelles, F., Pallejà, T., Val, L., Planas, S., Gil, E., Palacín, J., 2009. A tractor-mounted scanning LIDAR for the non-destructive measurement of vegetative volume and surface area of tree-row plantations: A comparison with conventional destructive measurements. Biosystems Engineering 102, 128-134.

Rusu, R.B., 2010. Semantic 3D object maps for everyday manipulation in human living environments. KI-Künstliche Intelligenz 24, 345-348.

Rusu, R.B., Blodow, N., Beetz, M., 2009. Fast point feature histograms (FPFH) for 3D registration, IEEE International Conference on Robotics and Automation. IEEE, Kobe, Japan, pp. 3212-3217.

Rusu, R.B., Marton, Z.C., Blodow, N., Dolha, M., Beetz, M., 2008. Towards 3D point cloud based object maps for household environments. Robotics and Autonomous Systems 56, 927-941.

Sankaran, S., Khot, L.R., Espinoza, C.Z., Jarolmasjed, S., Sathuvalli, V.R., Vandemark, G.J., Miklas, P.N., Carter, A.H., Pumphrey, M.O., Knowles, N.R., Pavek, M.J., 2015. Low-altitude, high-resolution aerial imaging systems for row and field crop phenotyping: A review. European Journal of Agronomy 70, 112-123.

Sanz-Cortiella, R., Llorens-Calveras, J., Escolà, A., Arnó-Satorra, J., Ribes-Dasi, M., Masip-Vilalta, J., Camp, F., Gràcia-Aguilá, F., Solanelles-Batlle, F., Planas-DeMartí, S., Pallejà-Cabré, T., Palacin-Roca, J., Gregorio-Lopez, E., Del-Moral-Martínez, I., Rosell-Polo, J.R., 2011. Innovative LIDAR 3D Dynamic Measurement System to Estimate Fruit-Tree Leaf Area. Sensors 11, 57-69.

Sharma, B., Mills, C.I., Snowden, C., Ritchie, G.L., 2015. Contribution of Boll Mass and Boll Number to Irrigated Cotton Yield. Agronomy Journal 107, 1845-1853.

Sharma, B., Ritchie, G.L., 2015. High-Throughput Phenotyping of Cotton in Multiple Irrigation Environments. Crop Science 55, 958-969.

Shi, Y., Wang, N., Taylor, R.K., Raun, W.R., 2015. Improvement of a ground-LiDAR-based corn plant population and spacing measurement system. Computers and Electronics in Agriculture 112, 92-101.

Si, Y., Liu, G., Feng, J., 2015. Location of apples in trees using stereoscopic vision. Computers and Electronics in Agriculture 112, 68-74.

SICK, A., 2015. Operation Instructions LMS5xx Laser Measurement Sensors. <https://www.sick.com/media/dox/4/14/514/Operating_instructions_Laser_Measurement_Sensors_of_the_LMS5xx_Product_Family_en_IM0037514.PDF>.

Siebert, J.D., Stewart, A.M., 2006. Influence of plant density on cotton response to mepiquat chloride application. Agronomy Journal 98, 1634-1639.

Simko, I., Jimenez-Berni, J.A., Sirault, X.R.R., 2016. Phenomic Approaches and Tools for Phytopathologists. Phytopathology 107, 6-17.

Singh, A.K., Ganapathysubramanian, B., Sarkar, S., Singh, A., 2018. Deep Learning for Plant Stress Phenotyping: Trends and Future Perspectives. Trends in Plant Science 23, 883-898.

Snavely, N., Seitz, S.M., Szeliski, R., 2008. Modeling the world from internet photo collections. International journal of computer vision 80, 189-210.

Sritarapipat, T., Rakwatin, P., Kasetkasem, T., 2014. Automatic Rice Crop Height Measurement Using a Field Server and Digital Image Processing. Sensors 14, 900-926.

Stamatiadis, S., Tsadilas, C., Schepers, J.S., 2010. Ground-based canopy sensing for detecting effects of water stress in cotton. Plant and soil 331, 277-287.

Steder, B., Rusu, R.B., Konolige, K., Burgard, W., 2011. Point feature extraction on 3D range scans taking into account object boundaries, Robotics and automation (icra), 2011 ieee international conference on. IEEE, pp. 2601-2608.

Stöckle, C., Kemanian, A., 2009. Crop radiation capture and use efficiency: a framework for crop growth analysis. Crop Physiology: Applications for Genetic Improvement and Agronomy. Academic Press, San Diego, CA, USA, 145-170.

Sui, R., Fisher, D.K., Reddy, K.N., 2012. Cotton yield assessment using plant height mapping system. Journal of Agricultural Science 5, 23-31.

Sun, S., Li, C., Paterson, A., Jiang, Y., Robertson, J., 2018a. 3D computer vision and machine learning based technique for high throughput cotton boll mapping under field conditions, 2018 ASABE Annual International Meeting. American Society of Agricultural and Biological Engineers, pp. 1-10.

Sun, S., Li, C., Paterson, A., Jiang, Y., Xu, R., Robertson, J., Snider, J., 2018b. In-field high throughput phenotyping and cotton plant growth analysis using LiDAR. Frontiers in Plant Science 9, 1-17.

Sun, S., Li, C., Paterson, A.H., 2017. In-Field High-Throughput Phenotyping of Cotton Plant Height Using LiDAR. Remote Sensing 9, 1-17.

Szeliski, R., 2010. Computer Vision: Algorithms and Applications.

Taheriazad, L., Moghadas, H., Sanchez-Azofeifa, A., 2016. A new approach to calculate Plant Area Density (PAD) using 3D ground-based LiDAR, in: Michel, U., Schulz, K., Ehlers, M., Nikolakopoulos, K.G., Civco, D. (Eds.), Earth Resources and Environmental Remote Sensing/Gis Applications Vii. Spie-Int Soc Optical Engineering, Bellingham.

Tao, Y., Zhou, J., 2017. Automatic apple recognition based on the fusion of color and 3D feature for robotic fruit picking. Computers and Electronics in Agriculture 142, 388-396.

Tardieu, F., Cabrera-Bosquet, L., Pridmore, T., Bennett, M., 2017. Plant Phenomics, From Sensors to Knowledge. Current Biology 27, 770-783.

Tessmer, O.L., Jiao, Y., Cruz, J.A., Kramer, D.M., Chen, J., 2013. Functional approach to high-throughput plant growth analysis. BMC systems biology 7, 1-17.

Tester, M., Langridge, P., 2010. Breeding Technologies to Increase Crop Production in a Changing World. Science 327, 818-822.

Thompson, A., Conrad, A., Conley, M., Shrock, H., Taft, B., Miksch, C., Mills, T., Dyer, J., 2018. Professor: A motorized field-based phenotyping cart. HardwareX 4, 1-10.

Thuy Tuong, N., Slaughter, D.C., Max, N., Maloof, J.N., Sinha, N., 2015. Structured Light-Based 3D Reconstruction System for Plants. Sensors 15, 18587-18612.

Tian, J., Wang, C., Xia, J., Wu, L., Xu, G., Wu, W., Li, D., Qin, W., Han, X., Chen, Q., Jin, W., Tian, F., 2019. Teosinte ligule allele narrows plant architecture and enhances high-density maize yields. Science 365, 658-664.

Tilly, N., Hoffmeister, D., Cao, Q., Huang, S., Lenz-Wiedemann, V., Miao, Y., Bareth, G., 2014. Multitemporal crop surface models: Accurate plant height measurement and biomass estimation with terrestrial laser scanning in paddy rice. Journal of Applied Remote Sensing 8, 083671-083671.

Tilly, N., Hoffmeister, D., Cao, Q., Lenz-Wiedemann, V., Miao, Y., Bareth, G., 2015. Transferability of models for estimating paddy rice biomass from spatial plant height data. Agriculture 5, 538-560.

Tilman, D., Balzer, C., Hill, J., Befort, B.L., 2011. Global food demand and the sustainable intensification of agriculture. Proceedings of the National Academy of Sciences 108, 20260-20264.

Toda, L.L., Yokingco, J.C.E., Paringit, E.C., Lasco, R.D.J.A.g., 2017. A LiDAR-based flood modelling approach for mapping rice cultivation areas in Apalit, Pampanga. 80, 34-47.

Townsend, T., Sette, J., 2016. Natural fibres and the world economy, Natural fibres: advances in science and technology towards industrial applications. Springer Dordrecht, pp. 381-390.

Underwood, J., Wendel, A., Schofield, B., McMurray, L., Kimber, R., 2017. Efficient in-field plant phenomics for row-crops with an autonomous ground vehicle. Journal of Field Robotics 34, 1061-1083.

Underwood, J.P., Hung, C., Whelan, B., Sukkarieh, S., 2016. Mapping almond orchard canopy volume, flowers, fruit and yield using lidar and vision sensors. Computers and Electronics in Agriculture 130, 83-96.

USDA, 2018a. Crop Production Historical Track Records (https://www.nass.usda.gov/Publications/Todays_Reports/reports/croptr18.pdf). National Agricultural Statistics Service.

USDA, 2018b. Georgia Agricultural Statistics Service (https://www.nass.usda.gov/Quick_Stats/Ag_Overview/stateOverview.php?state=GEORGIA).

Vapnik, V., 2013. The nature of statistical learning theory. Springer science & business media, New York, USA.

Vazquez-Arellano, M., Griepentrog, H.W., Reiser, D., Paraforos, D.S., 2016. 3-D Imaging Systems for Agricultural Applications-A Review. Sensors 16, 1-24.

Vázquez-Arellano, M., Reiser, D., Paraforos, D.S., Garrido-Izard, M., Burce, M.E.C., Griepentrog, H.W., 2018. 3-D reconstruction of maize plants using a time-of-flight camera. Computers and Electronics in Agriculture 145, 235-247.

Velumani, K., Elberink, S.O., Yang, M.Y., Baret, F., 2017. Wheat ear detection in plots by segmenting mobile laser scanner data. ISPRS Annals of Photogrammetry, Remote Sensing & Spatial Information Sciences IV-2/W4, 149-156.

Verdoja, F., Thomas, D., Sugimoto, A., 2017. Fast 3D point cloud segmentation using supervoxels with geometry and color for 3D scene understanding, IEEE International Conference on Multimedia and Expo (ICME). IEEE, Hong Kong, pp. 1285-1290.

Wallace, L., Hillman, S., Reinke, K., Hally, B., 2017. Non-destructive estimation of above-ground surface and near-surface biomass using 3D terrestrial remote sensing techniques. Methods in Ecology and Evolution 8, 1607-1616.

Wang, C.L., Zou, X.J., Tang, Y.C., Luo, L.F., Feng, W.X., 2016a. Localisation of litchi in an unstructured environment using binocular stereo vision. Biosystems Engineering 145, 39-51.

Wang, G., Laga, H., Xie, N., Jia, J.Y., Tabia, H., 2018. The Shape Space of 3D Botanical Tree Models. Acm Transactions on Graphics 37, 1-17.

Wang, L.A., Zhou, X.D., Zhu, X.K., Dong, Z.D., Guo, W.S., 2016b. Estimation of biomass in wheat using random forest regression algorithm and remote sensing data. Crop Journal 4, 212-219.

Watanabe, K., Guo, W., Arai, K., Takanashi, H., Kajiya-Kanegae, H., Kobayashi, M., Yano, K., Tokunaga, T., Fujiwara, T., Tsutsumi, N., Iwata, H., 2017. High-Throughput Phenotyping of Sorghum Plant Height Using an Unmanned Aerial Vehicle and Its Application to Genomic Prediction Modeling. Frontiers in Plant Science 8, 1-11.

Wei, J.-d., Fei, S.-m., Wang, M.-l., Yuan, J.-n., 2008. Research on the Segmentation Strategy of the Cotton Images on the Natural Condition Based upon the HSV Color-Space Model. Cotton Science 1, 1-10.

Weiss, U., Biber, P., 2011. Plant detection and mapping for agricultural robots using a 3D LIDAR sensor. Robotics and autonomous systems 59, 265-273.

Weraduwagel, S.M., Chen, J., Anozie, F.C., Morales, A., Weise, S.E., Sharkey, T.D., 2015. The relationship between leaf area growth and biomass accumulation in Arabidopsis thaliana. Frontiers in Plant Science 6, 1-21.

White, J.W., Andrade-Sanchez, P., Gore, M.A., Bronson, K.F., Coffelt, T.A., Conley, M.M., Feldmann, K.A., French, A.N., Heun, J.T., Hunsaker, D.J., Jenks, M.A., Kimball, B.A., Roth, R.L., Strand, R.J., Thorp, K.R., Wall, G.W., Wang, G., 2012. Field-based phenomics for plant genetics research. Field Crops Research 133, 101-112.

Wierzchoń, S.T., Kłopotek, M., 2018. Modern algorithms of cluster analysis. Springer, Switzerland.

Wu, S., Wen, W., Xiao, B., Guo, X., Du, J., Wang, C., Wang, Y.J.F.i.P.S., 2019. An Accurate Skeleton Extraction Approach from 3D Point Clouds of Maize Plants. Frontiers in Plant Science 10, 1-14.

Xiong, X., Yu, L.J., Yang, W.N., Liu, M., Jiang, N., Wu, D., Chen, G.X., Xiong, L.Z., Liu, K.D., Liu, Q., 2017. A high-throughput stereo-imaging system for quantifying rape leaf traits during the seedling stage. Plant Methods 13, 1-17.

Xu, R., Li, C., Paterson, A., Jiang, Y., Sun, S., Robertson, J., 2017. Cotton bloom detection using aerial images and convolutional neural network. Frontiers in Plant Science 8, 1-17.

Xu, R., Li, C., Paterson, A.H.J.P.o., 2019. Multispectral imaging and unmanned aerial systems for cotton plant phenotyping. Plos One 14, 1-20.

Yamamoto, K., Guo, W., Yoshioka, Y., Ninomiya, S., 2014. On Plant Detection of Intact Tomato Fruits Using Image Analysis and Machine Learning Methods. Sensors 14, 12191-12206.

Yin, X., Liu, X., Chen, J., Kramer, D.M., 2018. Joint Multi-Leaf Segmentation, Alignment, and Tracking for Fluorescence Plant Videos. IEEE Trans Pattern Anal Mach Intell 40, 1411-1423.

Yuan, W., Howard, R.E., Dana, K.J., Raskar, R., Ashok, A., Gruteser, M., Mandayam, N., 2014. Phase messaging method for time-of-flight cameras, 2014 IEEE International Conference on Computational Photography (ICCP). IEEE, pp. 1-8.

Zaidi, S.S.-e.-A., Vanderschuren, H., Qaim, M., Mahfouz, M.M., Kohli, A., Mansoor, S., Tester, M., 2019. New plant breeding technologies for food security. Science 363, 1390-1391.

Zaman-Allah, M., Vergara, O., Araus, J.L., Tarekegne, A., Magorokosho, C., Zarco-Tejada, P.J., Hornero, A., Alba, A.H., Das, B., Craufurd, P., Olsen, M., Prasanna, B.M., Cairns, J., 2015. Unmanned aerial platform-based multi-spectral imaging for field phenotyping of maize. Plant Methods 11, 1-10.

Zhang, L., Grift, T.E., 2012. A LIDAR-based crop height measurement system for Miscanthus giganteus. Computers and Electronics in Agriculture 85, 70-76.

Zhao, K., Popescu, S., 2009. Lidar-based mapping of leaf area index and its use for validating GLOBCARBON satellite LAI product in a temperate forest of the southern USA. Remote Sensing of Environment 113, 1628-1645.

Zhou, Y., Tuzel, O., 2017. VoxelNet: End-to-End Learning for Point Cloud Based 3D Object Detection, IEEE/CVF Conference on Computer Vision and Pattern Recognition. IEEE, Salt Lake City, UT, USA pp. 1-10.

Zhu, Z.H., Fu, J.Y., Yang, J.S., Zhang, X.M., 2016. Panoramic Image Stitching for Arbitrarily Shaped Tunnel Lining Inspection. Computer-Aided Civil and Infrastructure Engineering 31, 936-953.